NASA CONTRACTOR REPORT

NASA CR-1196

NASA CR-11

THEORETICAL PREDICTION OF CRATER SIZE FOR HYPERVELOCITY IMPACT BY REDUCED-DENSITY PARTICLES

by T. D. Riney and J. F. Heyda

NATIONAL AERONAUTICS AND SPACE ADMINISTRATION • WASHINGTON, D. C. • NOVEMBER 1968

THEORETICAL PREDICTION OF CRATER SIZE FOR HYPERVELOCITY

IMPACT BY REDUCED-DENSITY PARTICLES

By T. D. Riney and J. F. Heyda

FOREWORD

The work described herein was conducted by members of the Mechanics Section of the Space Sciences Laboratory, General Electric Company, King of Prussia, Pa., under NASA Contract NAS 3-8512. Technical direction for the Lewis Research Center was provided by S. Lieblein and I. J. Loeffler of the Airbreathing Engines Division, NASA-Lewis Research Center. This report is based upon research performed between May 18, 1966, and August 17, 1967.

ABSTRACT

A theoretical study is presented which predicts the depth of craters produced in a thick aluminum alloy target, AL-2024 T6, when impacted by low-density heterogeneous and homogeneous projectiles at velocities of 7.35, 20, and 50 km/sec. The prediction is based on a hydrodynamic model for computing the flow field and a comparison of the computed dynamic pressure with the yield stress of the target for terminating the crater. This indirect method for including the strength effect is first shown to give an accurate prediction of the final crater produced by a normal density aluminum projectile at an impact velocity for which experimental data are available. The criterion is then applied for heterogeneous porous projectiles and homogeneous projectiles of reduced density for velocities in the meteoroid range. Also included is the development of an improved equation of state for homogeneous reduced density projectiles and the numerical technique, involving linked particle-in-cell and Eulerian finite difference schemes, that was employed for the calculations.

TABLE OF CONTENTS

THEORETICAL PREDICTION OF CRATER SIZE FOR HYPERVELOCITY IMPACT BY REDUCED-DENSITY PARTICLES

by

T. D. Riney* and J. F. Heyda**

SUMMARY

In order to study the effect that the reduced bulk density and structure of meteoroids may have on their penetrating ability, numerical techniques have been used to solve the compressible flow equations for a thick 2024 T6 aluminum alloy target impacted by several low-bulk-density projectiles over a range of velocities characteristic of meteoroids. The projectiles were chosen to correspond in mass and shape to a solid one of normal density (2.7 gm/cc), two heterogeneous configurations with distributed mass kernals of normal density and average bulk density of 0.5 gm/cc, and a homogeneous projectile of reduced density equal to 0.5 gm/cc. Aluminum, which has Hugoniot characteristics similar to stone (for stony meteoroids), was selected as the basic material of the projectiles.

The numerical treatment selected for solving the axisymmetric compressible fluid equations employed a particle-in-cell computer code, VISTA, for the early stages of the process in which it is desired to follow the distortion of the various projectile configurations in detail. Once the projectile has delivered momentum and energy to the target a LINK program was used to smooth the flow field in a critical region near the axis of symmetry and to rewrite the computational data in a form suitable for continuing the calculations with an Eulerian computer code, PICWICK III.

An adequate equation of state for normal density aluminum representing the targets, solid projectiles, and distributed mass kernels in the heterogeneous projectiles is available in the literature. Since it does not describe the response of homogeneous reduced-density aluminum, an improved equation of state was developed for this material based on a modified Plate-Gap Model of a porous solid.

Two methods have been employed for allowing for strength effects in interpreting the hydrodynamic calculations: an indirect method based on late-stage equivalence which was found to be inapplicable for predicting craters for the heterogeneous projectiles; and a more direct applicable

---

* Group Leader, Theoretical and Experimental Mechanics Operation
** Consulting Mathematician, Mechanics Section

1

method in which the dynamic pressure in the region surrounding the forming crater is compared with the residual yield strength of the target material in the wake of the shock. The two criteria were shown to give compatible results when applied to the calculations corresponding to impact by a normal-density projectile at 7.35 and 20 km/sec. The explicit prediction based on the dynamic pressure criterion is also found to be in excellent agreement with existing experimental data for the lower velocity.

The verified prediction method was then applied to the prescribed low-density heterogeneous and homogeneous projectiles for impact velocities of 7.35, 20, and 50 km/sec. In all cases the predicted crater depths were less than was predicted for normal density projectiles of the same mass and impact velocity. The craters of the reduced-density projectiles were shallower and wider. The difference was found to decrease as the velocity was increased but persisted throughout the velocity range covered.

I. INTRODUCTION

The existence of a hazard to the operation of a space waste-heat radiator of space power systems or other spacecraft components due to meteoroid impact has been recognized as an important factor in the design of such components (ref. 1). The possible severe weight penalty associated with providing armor or other protective material for such components involving lengthy exposure of large vulnerable areas requires that a realistic evaluation of the hazard be made in order to develop efficient, lightweight meteoroid protection.

Many variables may affect the phenomenon of hypervelocity impact into fluid-carrying space radiators, such as the specific geometry, the materials used for the radiators and armor protection, the operating temperature, and the presence of a liquid or gas in the tube. The NASA Lewis Research Center has employed laboratory tests to study these effects experimentally (refs. 2 and 3). In particular it has been shown that the inner surface of a fluid-carrying tube could be made to dimple and spall with armor thicknesses significantly greater than the crater depth. Hence, simple cratering is not the only critical design condition.

Although these laboratory tests give a better qualitative and quantitative understanding of the damage modes resulting from impact on specific armor and radiator configurations, they are restricted to velocities less than 10 km/sec by the limited capability of available acceleration devices. The actual velocity range of meteoroids extends to 72 km/sec with typical values of 20 to 30 km/sec. Moreover, the majority of the meteoroids important to large components such as space radiators are believed to be of heterogeneous, porous structure of average bulk density as low as 0.2 gm/cc (ref. 4). Tests with heterogeneous low-density fluffy projectiles have not been possible even for laboratory velocities since the simulated meteoroids cannot withstand the acceleration required by the experimental techniques. It has been suggested, however, that impact damage resulting from such particles might not be the same as from solid particles of the same mass (ref. 2).

In view of the limited capability of experimental techniques, the NASA Lewis Research Center considered it desirable to employ theoretical techniques to simulate hypervelocity impact by heterogeneous low-density meteoroids. The normal impact of equi-mass projectiles of various mass distributions onto a thick 2024-T6 aluminum target was selected for the theoretical studies. The projectiles were chosen to simulate stony meteoroids corresponding in mass and shape to a solid one of normal density, 2.7 gm/cc, two heteogeneous configurations with distributed mass kernels of normal density and average bulk density of 0.5 gm/cc, and a homogeneous projectile

of reduced density equal to 0.5 gm/cc. These four configurations, designated respectively as α-, β-, γ-.and δ-projectiles, are depicted in Fig. 1. The objective of the study was to compare the theoretical crater depths of these reduced-density projectiles with that of the corresponding normal-density particle for velocities of 7.35, 20 and 50 km/sec.

To solve the system of equations governing the axisymmetric impact problems of interest requires the use of numerical techniques programmed for modern digital computers. In the next section of this report the adaptations required for the present study are described. Also presented is the criterion incorporated into the calculations in order to predict the final crater dimensions.

A necessary input for the numerical calculations is a hydrodynamic equation of state for the projectile and target materials. Since only limited shock Hugoniot data were available for stony materials, an aluminum equation of state was used for the projectiles as well as the targets. This approximation is consistent with their nearly equal normal densities. Even for aluminum, however, no satisfactory equation of state was available for the treatment of the reduced density δ - projectile. An earlier study (ref. 5) has shown that the pressures produced in the target along the axis of symmetry are sensitive to a change in the equation of state assumed for a reduced density projectile. It may be that the cratering flow is similarly sensitive. Consequently, an improved equation of state for porous aluminum, as well as other materials, is developed in the third section of the report. The subsequent sections contain the details of the calculations and the predictions of the final crater dimensions for the seven problems treated.

II. NUMERICAL TREATMENT

The response of the target material to the loading induced by meteoroid impact ranges from hydrodynamic behavior with negligible shear stresses for early time close to the point of impact, to purely elastic behavior at a later time after the cratering or penetration process is complete. The problem treated in its most general aspects requires a detailed investigation of the behavior of different material models under rapid loading: a hydrodynamic model in the impact zone; a visco-plastic model in a transition area; an elastic-plastic model in a plasticized region; and an elastic model in an elastic precursor region. Some compromise must be made between the complexity of the physical problem and the practical difficulties involved in solving the equations governing the model selected.

2.1   Choice of Computational Method

For a given one of these models the conservation relations for mass, momentum, and energy, into which appropriate constitutive relations describing material response to intense impulsive loading have been inserted, yield a system of partial differential equations. A solution to these equations for realistic geometries and boundary conditions cannot be obtained without resorting to large-scale computer codes. Of many possible choices of numerical schemes, three basic procedures have been applied to problems of this nature. In schemes based on a Lagrangian description, a coordinate system or grid is embedded into the configuration to be studied. The deformation and flow of the projectile-target configuration is then monitored with reference to this deformed grid-work. In Eulerian numerical schemes, the coordinate system is not embedded into the configuration, but is rather fixed in space and the calculations follow the material that happens to be in a given computational cell at that particular time. A third type of numerical method is the particle-in-cell scheme which is a combination approach insofar as both the Eulerian and Lagrangian coordinate systems are utilized in each cycle of the calculation. The Lagrangian representation, however, is approximate in the particle-in-cell scheme since it consists of discrete mass particles whose positions are monitored with respect to a grid that is fixed in space.

Each of these numerical schemes has advantages and disadvantages. The Lagrangian scheme treats material interfaces and free surfaces in a straight forward fashion and also permits the use of constitutive relations for the materials in which the stress history of each piece of material is taken into account. Such a capability is required to treat an elastic-plastic model. The Lagrangian description, however, is sensitive to the distortions in the flow field being studied, and instabilities are introduced if the embedded cells are deformed too severely. During hypervelocity impact both

projectile and target are subjected to severe distortions, and the embedded cells would need to be repeatedly rezoned if the calculations were to be continued. A further complication in problems involving the heterogeneous β and γ projectiles (Fig. 1) would be the necessity of allowing for the closing of the voids as the projectiles are distorted.

In the case of Eulerian schemes, large distortions cause no problem. However, the stress history that a given segment of material has been subjected to cannot be obtained. Consequently, an elastic-plastic model is difficult to treat. Of more importance in the present application is the fact that it is extremely difficult to treat more than a single material, and free surfaces cannot be treated without resorting to artificial constraints on the flow. This is a consequence of the fact that material entering a cell of the fixed Eulerian mesh is considered to be immediately diffused uniformly throughout the cell volume. The capability of distinguishing between projectile and target materials is required in treating δ -projectiles, and the capability of treating special projectile geometries with internal free surfaces at the voids is required for the problems involving β and γ -projectiles.

The combined Eulerian and Lagrangian coordinate systems used in the particle-in-cell scheme readily permits the treatment of the large distortions, free surfaces, and multiple materials. The representation of the materials by the mass particles, whose positions are monitored at each stage of the calculation, allows free surfaces to be located and avoids the false diffusion problem. The particle-in-cell scheme cannot treat an elastic-plastic model. It has been found that the method fails prior to the onset of strength effects because of yet another reason: the resolution provided by the discrete mass representation employed does not permit the flow process to be followed at pressures low enough for the anisotropic components of the stress tensor to play a significant role.

Since none of the individual numerical schemes is capable of treating the full cratering process it was decided to use the particle-in-cell scheme in the early stages when it is desirable to follow the interaction of the complex projectile configuration with the target. Once the projectile has delivered its energy and buried itself in the target the computations will be continued from that point using an Eulerian numerical scheme.

Neither the Eulerian nor the particle-in-cell schemes used treat the elastic-plastic regime of the cratering process. The visco-plastic model with realistic choices for the viscosity parameters has led to numerical results using the Eulerian scheme that are essentially the same as obtained using a compressible fluid model (ref. 6). A compressible fluid model was therefore chosen for the calculations, and an indirect criterion for inclusion of the strength of the target was employed for the prediction of the final crater dimensions.

2.2   Finite Difference Approximations

The simplifying assumption that the impacted materials behave like a compressible fluid, valid during the early stages of the process, leads to the following system of equations for the axisymmetric case (all symbols are defined in the Appendix):

$$p = f(\rho, I) \tag{2.1}$$

$$\frac{\partial \rho}{\partial t} + u \frac{\partial \rho}{\partial r} + v \frac{\partial \rho}{\partial z} + \rho \, \mathrm{div} \, \overline{u} = 0 \tag{2.2}$$

$$\rho \left(\frac{\partial u}{\partial t} + u \frac{\partial u}{\partial r} + v \frac{\partial u}{\partial z} \right) = - \frac{\partial p}{\partial r} \tag{2.3}$$

$$\rho \left(\frac{\partial v}{\partial t} + u \frac{\partial v}{\partial r} + v \frac{\partial v}{\partial z} \right) = - \frac{\partial p}{\partial z} \tag{2.4}$$

$$\rho \left(\frac{\partial I}{\partial t} + u \frac{\partial I}{\partial r} + v \frac{\partial I}{\partial z} \right) = - p \, \mathrm{div} \, \overline{u} \tag{2.5}$$

Here ρ, p, $\overline{u} = (u, 0, v)$, and I denote the density, pressure, velocity, and specific internal energy, respectively.

In both the particle-in-cell and Eulerian numerical schemes, the area occupied by an axial section of the projectile-target configuration is divided into a mesh of rectangular cells, fixed in space, through which the material moves. The sequence of numerical calculations for the two schemes is the same. At the end of the n-th time cycle, the density, velocity components, internal energy, and pressure are associated with each cell (i, j):

$$(\rho^n, u^n, v^n, I^n, p^n)_{i,j} \tag{2.6}$$

To obtain the corresponding data at the end of the (n + 1)-th time cycle, one makes a three-phase calculation. In phase 1, the pressure is updated and the cellwise field functions are changed neglecting the motion of the medium. Thus, the transport terms are dropped from the momentum and energy equations, and (2.3), (2.4) and (2.5) are replaced by difference formulas for computing tentative new cellwise velocity components and internal energy:

$$(\rho^n, \tilde{u}^{n+1}, \tilde{v}^{n+1}, \tilde{I}^{n+1}, p^n)_{i,j} \tag{2.7}$$

In phase 2, the material contained in each cell is moved according to the velocity of the cell in which it is located and the velocities of the neighboring cells. The material moved carries its share of the cellwise energy and

7

momentum with it; the field functions are then recalculated to account for the motion:

$$(\rho^{n+1}, u^{n+1}, v^{n+1}, I^{n+1}, p^{n})_{i,j} \tag{2.8}$$

The pressure is now updated by substituting the cellwise values of ρ^{n+1} and I^{n+1} into the specified equation of state (2.1)':

$$(\rho^{n+1}, u^{n+1}, v^{n+1}, I^{n+1}, p^{n+1})_{i,j} \tag{2.9}$$

In phase 3, various functionals are computed which furnish checks on the accuracy of the calculations. The computations are then repeated for n+2, etc.

The only essential difference between the Eulerian and particle-in-cell numerical schemes used is in the treatment of the mass flow in phase 2 of each time cycle. The former employs an approximation of the continuity equation (2.2) to determine the diffusion of mass, momentum and energy across each cell boundary. The latter employs marker particles to represent centers of mass of discrete material elements whose positions are monitored as they move through the mesh of fixed cells, each mass particle carrying its share of cellwise energy and momentum for that time cycle. It is this Lagrangian treatment in phase 2 that enables the particle-in-cell scheme to readily treat free surfaces and multi-materials.

The detailed logic of the particle-in-cell computer program (VISTA), developed in a related study and used in carrying out the initial stages of the impact calculations during the present study, has been described in detail elsewhere (ref. 7). The logic of the Eulerian code PICWICK III, developed earlier and used for the later stages of each of the impact problems treated in this study, is very similar to that employed in the independently developed OIL code (ref. 8).

2.3   Singularity at Axis of Symmetry

In cylindrical coordinates

$$\text{div } \overline{u} = \frac{1}{r} \frac{\partial (ur)}{\partial r} + \frac{\partial v}{\partial z} \tag{2.10}$$

The singularity at the axis of symmetry, r = 0, leads to inaccuracies in the finite difference approximation for div $\overline{u}$ in the vicinity of the axis and, as a consequence of (2.5), corresponding inaccuracies in the finite difference

approximation for $\tilde{I}$. The usual central difference approximation (refs. 7 and 8) relates the cell center value of div $\bar{u}$ to values of the radial velocity at the right (R) and left (L) cell boundaries and the axial velocity at the front (F) and back (B) cell boundaries. These boundary values are taken to be the average of the cell center values of the two adjacent cells:

$$(\text{div } \bar{u})_{i,j} = \frac{1}{(i-1/2)h} \frac{(ur)_{R,j} - (ur)_{L,j}}{h} + \frac{v_{i,F} - v_{i,B}}{k}$$

At a cell adjacent to the axis, $i = 1$, the reflective condition $(ur)_{L,j} = 0$ is imposed and the above expression reduces to

$$(\text{div } \bar{u})_{1,j} = \frac{u_{1,j} + 3u_{2,j}}{2h} + \frac{v_{1,F} - v_{1,B}}{k} \qquad (2.11)$$

With this treatment it can be shown that there is no loss of total energy or axial momentum at the axis of symmetry.

Since $u = 0$ at $r = 0$, it is clear from application of L'Hospital's Rule to (2.10) that

$$\lim_{r \to 0} \text{div } \bar{u} = \left[\frac{\partial v}{\partial z} \right]_{r=0} \qquad (2.12)$$

Comparison with (2.11) indicates that the first term in the approximation for div $\bar{u}$ leads to too large an estimate when $u_1 + 3u_2 > 0$. This is always true during the early stages of the calculations after the rarefaction wave from the periphery of the impact area arrives at the axis of symmetry approximately one radius below the center of impact. Consequently, from (2.5), the internal energy is decreased at too great a rate during that period. Conversely, the kinetic energy is increased at a rate greater than it should be and, since this is reflected primarily in increased radial velocity, the effect is cumulative. This treatment, (2.11), however, has apparently been used by all published descriptions of computer codes which have utilized the basic particle-in-cell and Eulerian schemes developed at the Los Alamos Scientific Laboratory (eg. refs. 7 through 13).

During the course of this contract, a detailed analysis of the difference equations was made. A new formulation was developed which not only conserved total energy at the axis of symmetry, but also conserved kinetic energy and internal energy individually. Moreover, a forward difference scheme was used in the cells adjacent to the axis of symmetry in order to provide a better approximation to (2.12) than that obtained with (2.11). When the lengthy alterations were incorporated into the PICWICK III code, however, the presence of round-off errors under radical signs, required in the formulation to conserve the energy components, led to the failure of the new scheme in actual application.

9

The details of this analysis as well as several less ambitious attempts to improve the accuracy of the finite difference scheme in the vicinity of the axis have been documented (ref. 14). Although these studies provided great insight into the numerical method, they were not utilized in the computations reported in the sequel and will not be detailed here.

In the present calculations the VISTA code is used for the initial stages of the impact process. This includes that period of time during which the edge rarefactions arrive at the axis of symmetry and the radial flow near the axis is greatest. It therefore includes that portion of the process when the inaccuracies arising from the approximation (2.11) are greatest. The over estimate of the radial flow near the axis causes an excess of mass particles to move from the critical area near the axis. This effect is reflected by the sparsity of mass particles in the critical area that may be observed in plots of flow fields computed using particle-in-cell schemes (see for example Fig. 5b of ref. 15, Fig. 8 of ref. 16, and Fig. C-4 of ref. 17). The same effect is observed in the VISTA calculations in this report.

By the time the projectile has buried itself into the target and the cavitation flow takes over, the radial flow should be very small in the vicinity of the axis between the forming crater and shock in the target. The calculations associated with these later stages of the flow process should therefore be less sensitive to the singularity at the axis of symmetry provided the VISTA data, read off the magnetic tape as input data for these later stage PICWICK III calculations, is smoothed in the critical region.

2.4   VISTA to PICKWICK III Link

In making the link between the early stage VISTA calculations and the later stage PICWICK III calculations there are two principal steps. The VISTA data saved on magnetic tapes at the end of n-cycles is rewritten in the form appropriate for a restart using the PICWICK III program. Before the calculations are actually resumed, however, the data are smoothed in the vicinity of the axis of symmetry to reduce the inaccuracies resulting from the singularity there.

The LINK program to carry out these two steps is more involved than may be expected. This is a consequence of the complex storage sharing in the VISTA code which alternatively employs internal core storage and external storage, on magnetic tape or disk, for the mass particle information and the cell-wise information. LINK must necessarily process the VISTA mass particle information in order to accumulate the contributions to the mass, M, radial momentum, R, axial momentum, Z, and total energy, E, that each particle makes to the cell in which it is located. At this intermediate stage of the LINK computations, after all the particles have been

10

processed, the cellwise quantities in storage are the corresponding cumulative values:

$$(M^n, \ R^n, \ Z^n, \ E^n, \text{———})_{i,j} \ .$$

The dash represents the fact that the pressure in cell (i,j) is not yet computed and the associated storage is kept available. The associated field variables, corresponding to equation number (2.6), are then computed according to the following:

$$\left(\rho^n = \frac{M^n}{\tau} \ , \ u^n = \frac{R^n}{M^n} \ , \ v^n = \frac{Z^n}{M^n} \ , \ I^n = -\frac{1}{2}(u^2 + v^2) + \frac{E^n}{M^n} \ , \ \text{—} \right)_{i,j}$$

Here, $\tau_i = \tau_{i,j}$ is the volume of a cell in the i-th column of the mesh.

Having rewritten the data in a form suitable for PICWICK III, the LINK program next recomputes the density, radial velocity, and internal energy in the critical region near the axis of symmetry. In this region, consisting of the first N_1 columns and rows J_1 through J_2, the radial velocity is equated to zero and the axial velocity left unchanged, thus conserving axial momentum, while the density and internal energy are set equal to a common value within the N cells of each row. These common values are determined by requiring conservation of mass and total energy within each row.

The smoothing process decreases the kinetic energy in the affected region and increases the internal energy by a corresponding amount. It also increases the density adjacent to the axis. Its effect therefore is opposite to that due to the inaccuracy of the finite difference approximation to div $\overline{u}$ and attempts to compensate for the latter cumulative error prior to continuing the calculations with PICWICK III. In the problems treated here in this study the VISTA distribution was normally smoothed over the first three columns for about ten rows between the projectile-target interface and the shock wave in the target.

The VISTA data, smoothed near the axis of symmetry through processing by the LINK program, is read into the PICWICK III code as initial data. The projectile and target materials are no longer distinguished. The equation of state for the target material is used to compute the cellwise pressure $p^n = f(\rho^n, \ I^n)$ in the subsequent PICWICK III calculations.

III. EQUATIONS OF STATE

3.1   Normal Density Materials

Empirical equations of state of the form (2.1) have been constructed that fit the existing Hugoniot data for normal density aluminum, and approximate states off the Hugoniot curve, by simplified solid state physics and thermodynamic considerations. The most widely used of these forms is that due to R.K. Osborne of the Los Alamos Scientific Laboratory,

$$p = \frac{1}{e + \varphi_o} \left\{ \zeta(a_1 + a_2 |\zeta|) + e [b_o + \zeta(b_1 + b_2 \zeta) + I (c_o + c_1 \zeta)] \right\} \qquad (3.1)$$

Here $e = \rho_o I$, $\zeta = (\rho / \rho_o) - 1$ and the coefficients ρ_o, a_1, a_2, b_o, b_1, b_2, c_o, c_1, and φ_o are material constants. Table I gives the values of the constants for aluminum.

Equation (3.1) provides an adequate description of the response of normal density aluminum to intense compression. It was used to represent the target for all the calculations in this study. Equation (3.1) was also used to describe the response of the normal density aluminum α-projectile and the response of the distributed mass kernals of normal density aluminum occurring in the β- and γ-projectiles, Fig. 1.

The empirical equation (3.1) has been found, however, to be quite unreliable for predicting states far off the Hugoniot of normal density aluminum as is evidenced by its failure to check experimental data obtained by impacting porous solids (see ref. 17). Equation (3.1) cannot therefore satisfactorily describe the response of the δ-projectile in the VISTA impact calculations.

A "theoretically correct" equation of state for aluminum, based on more complete considerations from solid state physics, thermodynamics and some quantum mechanical calculations, has been developed (refs. 17, 18, 19). The equation is correct in the sense that it is the best that can be written based on current physical theory and has been formulated to fit the available Hugoniot data generated from both normal density and porous aluminum. The formulation, however, is presented in tabular form generated from complex computer computations and is most unsuitable for use in the VISTA calculations.

It was therefore necessary to develop an empirical equation of state of the form (2.1) that would adequately treat the porous aluminum δ-projectile.

3.2   Porous Materials

The empirical equation of state presented here is based on the observation that an arbitrary p, ρ, I state of a solid can be regarded as the Hugoniot state of a solid with a specified initial off-normal density (porous or augmented density) and that if a description of such Hugoniot states as a function of a "porosity parameter" is available, then the full equation of state of form (2.1) can be written as the locus of such Hugoniot curves. Fortunately, a relatively accurate model, the so-called Plate-Gap Model, is available for predicting Hugoniot states of an initially porous solid, and this will serve as the basis for developing the empirical equation of state.

1.   Consider the equation of state written in the form, equivalent to (2.1),

$$p = p(\eta, I) \quad , \quad \eta = \rho / \rho_o \quad , \tag{3.2}$$

where ρ_o is the normal (crystal) density of the solid and I is the specific internal energy. Geometrically, one may regard (3.2) as the equation of a surface.

If we take the initial state of the solid to be

$$p = 0, \quad I = 0, \quad \eta = 1, \tag{3.3}$$

then states achievable through shocking the material constitute its Hugoniot. Such states satisfy (3.2) and also the equation

$$I = \frac{p}{2\rho_o} \left(1 - \frac{1}{\eta}\right). \tag{3.4}$$

Equation (3.2), (3.4) jointly define the Hugoniot curve for the normal density solid, a curve which lies on the surface (3.2). This curve can also be written in the form

$$p = p(\eta); \quad I = I(\eta) \quad . \tag{3.5}$$

To obtain states off the curve (3.5), one can shock the solid from a porous initial state

$$p = 0, \quad I = 0, \quad \eta = \frac{1}{m} \quad , \quad m = \rho_o / \overline{\rho}_o, \tag{3.6}$$

where $\overline{\rho}_o$ is the initial density of the porous solid.   Equation (3.4) is then replaced by

$$I = \frac{p}{2\rho_o} \left(m - \frac{1}{\eta}\right) \tag{3.7}$$

13

and the displaced Hugoniot curve associated with this porosity by

$$p = p'(\eta, m), \quad I = I(\eta, m) \tag{3.8}$$

For a porous solid, $m > 1$; for one of augmented initial density, $m < 1$. Since from (3.7),

$$m = \frac{1}{\eta p} [p + 2\rho_o \eta I] , \tag{3.9}$$

we see that an arbitrary p, η, I state will correspond to a Hugoniot state for porosity m defined by (3.9). The equation of state surface (3.2) can then be generated as the locus of curves (3.8) as m varies from 0^+ to ∞. To proceed further one requires an independent formulation for the Hugoniot of a porous solid. This is supplied by the Plate-Gap Model which is discussed next.

2. Thouvenin (ref. 20) has described a model for the behavior of a porous solid under shock loading which is both simple and remarkably accurate. He replaces the solid by an array of parallel plates, each of normal density ρ_o and of thickness $\lambda = \overline{\rho}_o / \rho_o$, where $\overline{\rho}_o$ is the initial density of the porous material; the air gap between any two neighboring plates is taken to be $1-\lambda$, Fig. 2. The porous material is thus taken to be periodic in structure, the width of each period being unity and of density $\rho_o \lambda = \overline{\rho}_o$, thereby agreeing with the required initial density.

Consider now a plate impacting the first plate at speed $2u$. A shock is driven into it at speed $D(u)$ with corresponding particle velocity u, where $D = D(u)$ is the wave speed in the non-porous material. When the wave reaches the rear free surface of the first plate, the pressurized material of the plate begins to be unloaded by a rarefaction wave moving back toward the front of the plate. The unloaded material then fills in the gap $1-\lambda$ at the free surface velocity $u_{fs} = 2u$. The total time for all this to happen is then

$$\frac{\lambda}{D} + \frac{1-\lambda}{u_{fs}} ,$$

and this is taken to be the time for the crush-up wave velocity D^* in the porous material to cover unit thickness. Hence, we have the first of Thouvenin's relations

$$\frac{1}{D^*} = \frac{\lambda}{D(u)} + \frac{1-\lambda}{2u} . \tag{3.10}$$

Thouvenin derived a second relation relating u and the crush-up particle velocity u^* based on an assumed equilibrium crush-up state.

This state is assumed to occur when the shock driven into the unloaded material after its impact with the second plate reaches an asymptotic limiting strength after being attenuated by the unloading waves moving to the left in both first and second plates. Unfortunately, this second relation is based on an approximate analysis and is nowhere nearly as accurate as relation (3.10). However, as pointed out in an earlier report (ref. 5), this second relation may be replaced by

$$F(2u - u^*) = \bar{\rho}_o D^* u^* \quad , \tag{3.11}$$

where $p = F(u)$ is the shock polar for the non-porous solid. Equation (3.11) expresses the fact that u^* quite obviously must lie between u and 2u, (Fig. 3), and hence may be determined by conservation of momentum across the crush-up front. In Fig. 3, the arc $p = F(u)$ represents the loading path for a plate while arc PAB is the unloading isentrope, approximated here by the mirror image of the Hugoniot $p = F(u)$ about the vertical drawn at u.

Relations (3.10), (3.11) give a surprisingly accurate description of the Hugoniot states p^*, D^*, u^* for a porous material. This has been shown by comparing the predictions of the model with available experimental data for metals (see ref. 5). For aluminum, comparison is also made with predictions given by the "theoretically correct" equation of state due to Wagner and Bjork, (ref. 17).

3. To proceed further with the derivation of the empirical equation of state $p = p(\eta, I)$, it is observed that if p, η, I is an arbitrary state of the solid with initial state $p = 0$, $I = 0$, $\eta = 1$, then this state can be regarded as a Hugoniot state of the porous solid of porosity m given by (3.9) and having u^* and D^* determined from

$$u^* = \sqrt{2I} \quad , \quad D^* = \frac{m}{\rho_o} \frac{p}{\sqrt{2I}} = \frac{p + 2\rho_o \eta I}{\rho_o \eta \sqrt{2I}} \quad , \tag{3.12}$$

which follow directly from the conservation relations.

Next the basic plate-gap relations (3.10), (3.11) are rewritten in the form

$$\frac{1}{D^*} = \frac{1}{2u} - \frac{1}{m} \left[\frac{1}{2u} - \frac{1}{D(u)} \right] \quad , \tag{3.13}$$

$$\rho_o (2u - u^*) D(2u - u^*) = \frac{\rho_o}{m} D^* u^* \quad . \tag{3.14}$$

Substitution for m, u*, D* from (3.9) and (3.12) produces equation of state in parametric form where u is the parameter.

$$\frac{\rho_o \eta \sqrt{2I}}{p + 2\rho_o \eta I} = \frac{1}{2u} - \frac{\eta p}{p + 2\rho_o \eta I} \left[\frac{1}{2u} - \frac{1}{D(u)} \right],$$
(3.15)

$$(2u - \sqrt{2I}) \ D(2u - \sqrt{2I}) = \frac{p}{\rho_o} .$$
(3.16)

In these equations D is a known function of u. Thus, the only requirement for writing an equation of state for a given solid of known normal density ρ_o is knowledge of its shock velocity-particle velocity relation, D = D(u).

For most materials, and for many liquids also, the function D(u) is a linear function of u over a wide range of pressure within a given phase,

$$D(u) = A + Bu$$
(3.17)

where A and B are known empirical constants. Hence, based on this relation , a specific non-parametric form of (3.15, 3.16) may be derived. To do so, p is eliminated between (3.15) and (3.16) to obtain

$$\frac{2u}{D(u)} - \frac{\sqrt{2I}}{D(2u - \sqrt{2I})} = \frac{\eta - 1}{\eta} .$$
(3.18)

Using (3.17) in (3.18) u can then be determined in terms of η, I by solving a quadratic equation. The result turns out to be

$$u = \frac{\sqrt{\Delta} - A + \frac{B}{2} \left[3\sqrt{2I} + (3A - B\sqrt{2I}) \ (\frac{\eta - 1}{\eta}) \right]}{2B \left[2 - B(\frac{\eta - 1}{\eta}) \right]}$$
(3.19)

where the discriminant $\Delta \geq 0$ is given by

$$\Delta = \left[A + \frac{B}{2} \left\{ (A + B\sqrt{2I}) \ (\frac{\eta - 1}{\eta}) - 3\sqrt{2I} \right\} \right]^2 + 4AB \sqrt{2I} .$$
(3.20)

Knowing u, the full equation of state is then found in the form

$$p = \rho_o (2u - \sqrt{2I}) \ [A + B (2u - \sqrt{2I})]$$
(3.21)

Thus, from the manner in which it was derived assurance is provided that equation (3.21) will agree with experimental porous Hugoniot data.

4. In the derivation of (3.21), A and B were assumed constant. A more precise description for D(u) can be obtained by taking A, B, to be functions of η. For aluminum, these functions are

$$A(\eta) = .3452 + .1276\eta \ (cm/\mu sec)$$

$$B(\eta) = 1.8237 - .2933\eta \ .$$

(3.22)

The values (3.22) were used in the VISTA calculations to describe the response of the δ - projectile.

IV. CALCULATIONS

The four equal-mass projectile configurations of Fig. 1 were employed for a total of seven VISTA-PICWICK III computer runs as listed in Table II. In each case a thick 2024 T6 aluminum alloy target was impacted. The α-projectile, normal density aluminum, $\rho_o = 2.7$ gm/cc, was treated for impact velocities of $v_o = 0.735$ cm/μsec (problem N1), and $v_o = 2.0$ cm/μsec (problem N2). Three additional computer runs were made at $v_o = 2.0$ cm/μsec for reduced-density projectile configurations of average bulk density $\overline{\rho}_o = 0.5$ gm/cc. The first of these, the heterogeneous β-projectile, contains normal density aluminum kernals distributed throughout the volume of the projectile (problem N3). The second of these, the heterogeneous γ-projectile, contains normal density aluminum kernals that are concentrated along the central region and the periphery of the axisymmetric projectile configuration (problem N4). The third of these, the homogeneous δ-projectiles, is composed of uniformly reduced-density aluminum throughout (problem N5). The heterogeneous β-projectile was also treated for impact velocities of $v_o = 0.735$ cm/μsec (problem N6), and $v_o = 5.0$ cm/μsec (problem N7).

In the calculations, the equation of state form (3.1) was employed throughout except for the VISTA calculations in problem N5 wherein form (3.22) was used to determine the response of the porous δ-projectile. For the homogeneous material composing the α- and δ-projectiles, it is possible to combine the equations of state for the projectile and the target with the Rankine-Hugoniot relations (see ref. 21, pp. 13-16) to obtain the initial response of the impacted materials. This was done for impact velocities of $v_o = 0.735$, 2.0 and 5.0 cm/μsec and the corresponding Hugoniot values of the pressure, p_H, shock velocity, R_H, and compression, ρ_H/ρ_o, in the projectile and target are listed in Table III. For $v_o = 0.735$, and 2.0 cm/μsec the values listed for projectile and target of normal density aluminum correspond to the impact conditions in problems N1 and N2 respectively. For $v_o = 2.0$ cm/μsec, the values listed for normal density target and projectile of reduced density, $\overline{\rho}_o = 0.5$ gm/cc, correspond to the impact conditions in problem N5. From Table III is clear that at a given impact velocity the pressure that would be generated by a δ-projectile is approximately one-third that which would be generated by an α-projectile.

The axisymmetric numerical calculations were performed on the direct coupled IBM 7094/7044 computer system at the NASA Lewis Research Center. By careful treatment of the computing sequence and appropriate manipulation of internal and external memory with this system it was possible to provide a finite difference computational mesh in excess of 2000 cells in both the VISTA and PICWICK III codes. The choice of the computational mesh within this constraint and the number and distribution of the mass marker particles in the VISTA calculations depends on the resolution desired and the computing cost that appears reasonable.

In this study, a finite difference mesh of 36 columns and 52 rows (1872 cells) to represent an axial section of the projectile-target configuration seemed optimum. The initial configuration (Fig. 4), utilized VISTA's capability of representing the incoming projectile as partially outside the mesh, thereby leaving a greater number of rows available to represent the target. This choice also allows the finite difference mesh to be rezoned three times if desired. In each rezoning, possible in either the VISTA or PICWICK III phase of the calculations, four of the existing cells are combined into a single enlarged cell thus doubling the linear dimensions of the axial section of the configuration encompassed by the mesh (Fig. 5). In the VISTA calculations, the undisturbed target material was represented by nine mass markers per cell as were the homogeneous α- and δ-projectiles. Twenty-five mass markers were employed to represent each of the undisturbed mass kernals in the heterogeneous β- and γ-projectiles.

Typically, the VISTA calculations were continued for about three-hundred time cycles and required three hours IBM 7094 computer time. The subsequent PICWICK III calculations continued, on the average, for an additional two-hundred cycles and required approximately one hour of IBM 7094 computer time.

With each of the seven problems there was generated reams of numerical data describing the flow field at various stages of the impact process. The sheer volume limits the analysis and presentation of the results. Detailed examination of the data, hand plots, and even mechanical plotters were entirely too slow to be satisfactory. For these reasons ancillary computer programs were devised for facilitating the analysis of the calculations by use of the electronic Stromberg-Carlson 4020 computer recorder. Graphical displays giving the current projectile-target configuration, velocity field, $(u, v)_{i,j}$, and the mass flux field, $(\rho u, \rho v)_{i,j}$, were obtained at various stages of the cratering process.

19

V. RESULTS FOR NORMAL DENSITY PROJECTILES

5.1 Flow Field Description

The early stage deformation mechanisms computed with the VISTA code for an α-projectile impacting at $v_o = 0.735$ cm/μsec (problem N1) are shown in Figs. 6(a) through 6(f).* Shock fronts are smeared over two to three cell widths in finite difference calculations. Nevertheless, the approximate positions of the shock moving up into the projectile and the shock propagating down into the target from the contact area are apparent especially in the mass particle plots. Although the VISTA calculations were actually continued to almost 0.7μsec, the results beyond 0.5μ sec were increasingly inaccurate because of the discrete nature of the particle-in-cell mass representation. The LINK program was therefore employed at t = 0.434 μ sec and the calculations resumed with PICWICK III. The mass particle plot at t = 0.452, Fig. 6(e), displays the low density region at the axis of symmetry which results from the singularity in div $\bar{u}$ at the axis. This region was smoothed during the LINK processing of the data.

In Figs. 6(g) through 6(j), the mass flux field for problem N1 is depicted for the later stages computed using the PICWICK III code. These plots demonstrate the separation of the flow field in the target into two principal regions in which the mass flux, and hence the dynamic pressure, has peak values. One region is associated with the receding shock front and the other with the material surrounding the forming crater. It was necessary to rezone the finite difference mesh, four cells being combined into a single cell, between times depicted in Figs. 6(g) and 6(h) in order for the mesh to encompass the entire flow field.

When the impact velocity of the α-projectile was raised to $v_o = 2.0$ cm/μsec, (problem N2), the resulting higher compaction is more accurately treated by the discrete mass representation since more marker projectiles are compressed into a cell in the impacted region. Consequently, the VISTA calculations remained accurate for a longer time as indicated in Figs. 7(a) through 7(h). It became necessary to rezone the mesh during the course of the VISTA calculations, and the rectangular irregularity of the mass particles in Fig. 7 (g) is a consequence of the associated repositioning of the mass particles in the region originally covered by the finite difference mesh. The

---

*The dark annular regions appearing at the top of the mesh in the velocity field plots result from an error in the associated Stromberg-Carlson 4020 ancillary program. They should be ignored.

low density region at the axis of symmetry resulting from the singularity is again apparent in Figs. 7(e) and 7(g).

The LINK program was employed at t = 0.717 μsec in order to smooth the VISTA data in the critical region and to continue the calculations. Representative mass flux plots obtained in the subsequent PICWICK III calculations for problem N2 are shown in Figs. 7(i) and 7(j). A second rezoning of the finite difference mesh was required to follow the flow process to the stage at which the shock wave disengages itself from the forming crater.

The time variation of the partition of the total axial momentum, scalar radial momentum, and total energy between projectile and target materials is also monitored at each cycle of the VISTA calculations. These gross characteristics of the flow field are displayed in Figs. 8 and 9 for problems N1 and N2 respectively. The time after impact at which the LINK process was carried out is shown in each of the plots; the dashed curves beyond that time represents VISTA calculations that overlap the PICWICK III calculations made subsequent to the linking of the codes.

At the time of the LINK only 15% of the radial momentum in problem N1 is contained in the projectile materials, (Fig. 8(a)), but approximately 40% of the axial momentum and energy still resides in the projectile, (Figs. 8(b) and 8(c)). On the other hand, the projectile content of all three quantities is less than 5% at the time of the LINK in the case of problem N2, in Figs. 9(a) through 9(c).

The plots in Fig. 10 illustrate the continuity of the gross characteristics of the flow field calculated with VISTA and PICWICK III notwithstanding the local smoothing of the data during the LINK processing. The total forward axial momentum, Z_+, and the total outward radial momentum, R_+, are observed to be undisturbed by the linking process (Fig. 10(a)). Here

$$Z_+ = \sum_{i,j} M_{i,j} (v_+)_{i,j} \quad , \quad R_+ = \sum_{i,j} M_{i,j} (u_+)_{i,j} \qquad (5.1)$$

where the plus indicates that the sums are extended over those cells in the mesh for which the indicated velocity components are positive. The division of the total energy between kinetic and internal energy should be especially sensitive to the LINK processing since these quantities were adjusted in the vicinity of the axis. As illustrated in Fig. 10(b), there is indeed a cusp at that stage of the calculations, but the general trend of the time variation is

preserved in the subsequent PICWICK III calculations. These plots are for problem N1, but similar results were obtained for each problem treated.

5.2 Selection of Crater Termination Criterion

Since the VISTA - PICWICK III calculations employ a compressible fluid model, there is no direct method of determining the final crater surface from the calculations. Two criteria have been considered in predicting final crater depth in thick targets subjected to hypervelocity impact. One is based on the concept of late-stage equivalence of two flow-fields, and the other is based on a comparison of the dynamic pressure in the flow field with the yield stress of the target.

The principle of late-stage equivalence does not predict the final crater dimension directly, but rather it provides a basis for comparing flow fields (refs. 15 and 16). Since the pressure pulse in the target is the basic element in the cratering mechanism, the flow fields produced by two projectiles in a specified target material are compared at times when the locations of the shock wave in the target are an equal distance below the target surface. For equivalence it is required that at these corresponding times the total forward axial momentum Z_+, the total outward radial momentum, R_+, and the amplitude of the pressure pulse become equal prior to the onset of strength and strain-rate effects.

If two impact conditions produce equivalent flow-fields in a target, then the final craters are assumed identical. If late-stage equivalence is not realized between the impact condition of interest and one for which the final crater is known, however, the criteria cannot serve as a basis for crater predictions. It cannot therefore be applied for the cases of heterogeneous projectiles which are of primary interest in this study.

The dynamic pressure for predicting the final crater dimensions is based on the detailed nature of the flow field established in the impacted target (ref. 17). By the time the projectile has expended itself and the cratering process in the target is in progress, the flow field is separated into two principal regions since the shock wave in the target propagates at a higher velocity than the rate of crater growth. This disengagement of the two regions means that after a certain point in time the shock wave has no further direct effect on the cratering process. The final crater depends on the momentum content of the target material in the neighborhood of the forming crater and its interaction with the residual strength of that material

which has been processed by the earlier passage of the shock wave.

At the given location in the flow field surrounding the forming crater, the velocity vector has the magnitude and direction defined by

$$v_n = \sqrt{u^2 + v^2} \qquad \tan \varphi = u/v$$

The local mass flux is given by

$$M_f = \rho v_n = \rho \sqrt{u^2 + v^2}$$

The assumption that the momentum contained in this flux is perfectly absorbed by a surface normal to the velocity vector leads to the following expression for the dynamic pressure exerted on the surface at that location:

$$P_{dyn} = \frac{1}{2} \rho v_n^2 = \frac{1}{2} \rho (u^2 + v^2).$$

In predicting the location of the final crater surface it is assumed that the dynamic pressure exerted there must equal the yield stress of the target material:

$$P_{dyn} = \sigma_y(T) \qquad\qquad (5.2)$$

The target material will be left with a residual temperature T in the wake of the shock processing and, consequently, its yield strength will be decreased.

Criterion (5.2) represents an extension to hypervelocity impact calculations of a criterion earlier employed to predict the depth of a crater produced in a target by a metallic jet formed by a shaped charge (ref. 22). The jet penetration theory, however, is steady-state and one-dimensional and Bernoulli's law may be applied with more confidence.

In the present application the dynamic pressure distribution in the region of the target surrounding the forming crater changes with time and, consequently, criterion (5.2) does not define a unique surface. Nevertheless, in the calculations performed in the present studies, it was found that the surface thus defined remains very nearly stationary for an extended time, and the relation (5.2) does indeed locate a surface which will be interpreted as the predicted final crater surface.

23

Before proceeding to the application of the criterion for the normal density α-projectiles, it is convenient to indicate the manner in which the temperature dependence of the yield stress was determined. For a given shock amplitude to which the aluminum is subject, p_H, there will correspond a residual temperature after the material is released to zero pressure which may be computed from the equation of state and thermodynamic data (ref. 17). These corresponding values are plotted in Fig. 11. Also shown there is the temperature variation of the yield strength, $\sigma_y(T)$, of aluminum alloy AL-2024 T3 obtained from the producer's handbook (ref. 23). Elimination of the temperature between these two relations yields a single curve depicting the yield strength of AL-2024 T3 after processing by a shock of amplitude p_H, Fig. 12. The curve is also assumed valid for AL-2024 T6.

5.3   Crater Predictions

During the course of the calculations with PICWICK III, the dynamic-pressure was monitored in each computational cell of the finite difference mesh. Much lower values are attained between the two regions of peak values, one associated with the shock wave in the target and one in the material surrounding the forming crater. Consequently, an examination of the PICWICK III computer output data at a given time cycle allows the determination of the depth into the target at which the dynamic pressure in the region surrounding the forming crater attains a specified value. In Fig. 13(a) the lowest such point in each column of the finite difference mesh is depicted for two distinct times for problem N1. The dots in Fig. 13(a) indicate the depths at which p_{dyn} = 3.4 kb for t = 1.62 μ sec, and the dashes locate this delineation criterion at t = 2.30 μ sec after impact. There is very little variation for this extended time interval, and a smooth surface has been sketched representing the approximate envelope of these depths.

In Fig. 13(b) the computed peak axial pressure, p_{max}, attained at varying distances into the target is plotted. By combining this curve with the curve in Fig. 12, it is possible to estimate the residual yield stress, $\sigma_y(T)$, of the target material, at various depths, in the wake of the shock to which the material at that depth has been subjected. These values of $\sigma_y(T)$ are also plotted in Fig. 13(a). Since the p_{dyn} = 3.4 kb surface at the axis corresponds to a value $\sigma_y(T)$ = 3.4 kb, the surface will be assumed to represent the final crater surface according to the criterion of equation (5.2). Consequently, the final depth, P_c, and radius, R_c, of the crater are predicted on this basis to be

$$P_c/\ell = 2.4, \qquad R_c/\ell = 2.2, \qquad P_c/R_c = 1.09,$$

$$\tag{5.3}$$

$$P_c = 0.66 \text{ cm}, \qquad R_c = 0.61 \text{ cm}.$$

Similar results for problem N2 are presented in Fig. 14. The dots and dashes in Fig. 14(a) indicate the depths surrounding the forming crater at which $p_{dyn} = 3.4$ kb for $t = 1.69 \mu$ sec and $t = 2.70 \mu$sec after impact, respectively. The dashed curve is the approximate envelope of these locations and would represent the predicted final crater if there were no decrease in the yield stress, $\sigma_y(T)$, for the shock processed material on this surface. Combining the data of Figs. 12 and 14(b) allows the approximate yield stress of the shock processed material along the axis to be determined, and this information is also depicted in Fig. 14(a). Along the axis, the $p_{dyn} = 3.4$ kb surface corresponds to a yield stress of $\sigma_y(T) = 1.0$ kb and, consequently does not satisfy criterion (5.2). The solid curve in Fig. 14(a) represents the approximate envelope of the depths corresponding to $p_{dyn} = 2.0$ kb. Since it corresponds to the yield stress, $\sigma_y(T) = 2.0$ kb, of the shock processed material at that depth along the axis, it represents the predicted crater surface on the basis of the criterion of equation (5.2). Thus, for this case,

$$P_c/\ell = 4.4, \qquad R_c/\ell = 4, \qquad P_c/R_c = 1.1, \tag{5.4}$$

$$P_c = 1.22 \text{ cm}, \qquad R_c = 1.11 \text{ cm}.$$

5.4 Verification of Predictions

1. It is of interest to re-examine the flow field calculations for problems N1 and N2 on the basis of the principle of late-stage equivalence. Since the hydrodynamic equations may be scaled, the calculations actually apply for any geometrically similar aluminum-aluminum impact configuration at corresponding velocity. The results of problem N1 will be compared with those of problem N2 on an equal-energy basis. For this purpose, the characteristic length ℓ of problem N1 can be increased to a new value ℓ' to provide a kinetic energy at impact equal to that of problem N2. Since

$$K.E. \propto \rho_o \ell^3 v_o^2,$$

for constant projectile density the characteristic length ℓ' of the scaled problem N1$'$ must satisfy the relation

$$(\ell')^3_{N1'} (v_o')^2_{N1'} = (\ell^3 v_o^2)_{N2}, \tag{5.5}$$

whence

$$\frac{\ell'}{\ell} = \left(\frac{v_o}{v_o'} \right)^{2/3} = \left(\frac{2.0}{0.735} \right)^{2/3} = 1.949$$

Also

$$\frac{mass'}{mass} = \left(\frac{\ell'}{\ell}\right)^3 = 7.404$$

Consequently, distances and times computed for problem N1 are multiplied by 1.949, and the computed total forward momentum Z_+, and the total outward radial momentum R_+, present within the system at any instant of time, (equation (5.1)), are multiplied by 7.404. The scaled N1 problem, denoted by N1', treats a projectile of dimensions $\ell' = D' = 0.5406$ cm and mass $M_o' = 0.335$ gm impacting at velocity $v_o' = 0.735$ cm/μ sec.

In Fig. 15(a) the time dependent values of Z_+ and R_+ are compared for problems N1' and N2. The time dependent positions of the shock front in the target, for each of the two equal energy cases, are depicted in Fig. 15(b). The shock produced by the larger but slower projectile, problem N1', lags the one produced by the smaller but higher velocity projectile, problem N2, by $\Delta t = 0.4\mu$ sec. The results with this correction, corresponding to a translation along the time axis of the R_+ and Z_+ curves for problem N1', are also shown in Fig. 15(a).

The calculated peak pressures realized at various target depths are depicted in Fig. 15(c) for problems N1' and N2. The values attained are very close for depths greater than 1.5 cm, corresponding to pressures less than 110 kb.

The late-stage equivalence criterion is seen from Figs. 15(a) and 15(c) to be very nearly satisfied by energy scaling of the velocity. This implies that the exponent α, for the velocity dependence of the penetration depth, $P_c \sim v_o^\alpha$, is very near to $\alpha = 0.67$. Actually, the corrected values of R_+ and Z_+ for problem N1' are somewhat greater than the corresponding curves for problem N2 and a slightly smaller value of α would be within the accuracy of the computations.

2. The application of the late-stage equivalent criterion leads to results entirely compatible with the predictions obtained by directly applying criterion (5.2) to problems N1 and N2. The corresponding value of the exponent α, for the velocity dependence of the penetration depth is implied by (5.3) and (5.4). For $P_c \sim v_o^\alpha$,

$$\left(\frac{2.0}{.735}\right)^\alpha = \frac{4.4}{2.4} \quad , \text{ whence } \alpha = \frac{\log 1.83}{\log 2.72} = 0.60 \qquad (5.6)$$

A value of $\alpha = 0.67$ would correspond to pure energy scaling, whereas a value of $\alpha = 0.33$ would correspond to pure momentum scaling of the velocity effect on penetration depth. The sensitivity of estimate for α becomes apparent when it is observed that a change of P_c/ℓ in (5.4) to 4.3 would yield an estimate of $\alpha = 0.58$; if the change were simultaneous with an increase in the estimate of P_c/ℓ in (5.3) to 2.5, $\alpha = 0.54$ would be obtained.

3. The prediction (5.3) for problem N1 can be tested against available experimental data. A survey of the literature revealed six data points with aluminum projectiles impacting aluminum targets at velocities very close to that simulated in this calculation. Four impacts are reported in references 24 and 25. The remaining two data points were obtained by the General Motors Defense Research Laboratories under Contract No. NASW468 to the Lewis Research Center. Two of the thick targets are aluminum alloy AL-2024 T6 and four are AL-2014 T6. These data are listed in Table IV. To provide a direct comparison with prediction (5.3) the data were adjusted to a common velocity and projectile mass (or size) to compensate for variations in the projectile size and velocity in the experimental data, and it was assumed that the crater resulting from a sphere is the same as for a unit aspect ratio cylinder of the same mass. The adjustments, made under the assumption of energy equivalence, $M_o' v_o'^2 = M_o v_o^2$, are also listed in Table IV. The prediction $P_c = 0.66$ cm contained in (5.3) is seen to lie near the midpoint of the adjusted experimental observations.

VI. RESULTS FOR LOW-DENSITY PROJECTILES

The strength dependent criterion, (5.2), for predicting the final crater from the VISTA-PICWICK III calculations may now be applied to the five impact configurations simulating impact by low density projectiles (Table II). The β-, γ- and δ- projectiles, each of average bulk density of 0.5 gm/cc, were all treated for the case of impact at v_o = 2.0 cm/μsec. These problems, N3, N4 and N5 respectively, are set up to study the effect of the mass distribution within the projectile. The β-projectile was also considered at impact velocities of v_o = 0.735 and 5.0 cm/μsec. The corresponding problems, N6 and N7, respectively, together with N3, are examined to determine the effect of impact velocity for heterogeneous projectiles. Since problem N3 is involved in the study of both effects it will be examined first.

6.1 Heterogeneous β-Projectile (Problems N3, N6 and N7)

1. The early stage deformation mechanisms computed with the VISTA code for a β-projectile impacting at v_o = 2.0 cm/μsec, problem N3, are depicted in the SC-4020 plots shown in Figs. 16(a) through 16(h). The initial representation of the β-projectile is illustrated in Fig. 16(a). The irregular deformation of the target during the early stages is shown in Figs. 16(b) through 16(h). The shape of the shock front in the target, however, becomes more regular as it propagates, and at t = 0.703 μsec (Fig. 16(h)), the distortions in the flow field are apparent only near the surface of the forming crater.

The LINK program was employed at t = 0.703 μsec and calculations resumed with PICWICK III. The mass flux field computed for problem N3 is depicted in Figs. 16(i) and 16(j) for these later stages. It was necessary to rezone the finite difference mesh during the time interval between the times depicted in Figs. 16(i) and 16(j) in order for the mesh to encompass the entire flow field.

The time variation of the partition of the total axial momentum, scalar radial momentum, and total energy between projectile and target materials for the VISTA calculations are displayed in Fig. 17. The irregular flow observed in the graphical displays of the flow field in Fig. 16 are reflected in the irregularity of these gross features of the flow field. By the time of the LINK process, however, the partition of these gross quantities between projectile and target materials is varying smoothly with time. At that time (t = 0.703 μsec), the radial momentum content of the projectile is less than 10%. The axial momentum content of the projectile is actually negative. Much of the total energy carried by the projectile material, approximately 25%, is therefore contained in the blow-off or back splash of the

projectile illustrated in the plots of Fig. 16.

As discussed earlier for normal density projectiles, an examination of the PICWICK III computer output data at a given time cycle allows the determination of the depth into the target at which the dynamic pressure in the region surrounding the forming crater attains a specified value. In Fig. 18(a) the upper dots indicate the depths at which $p_{dyn} = 3.4$ kb for $t = 1.85 \mu$sec, and the upper dashes locate the delineation criterion for $t = 3.17 \mu$sec after impact. The dashed curve forming the approximate envelope of these locations would represent the predicted final crater if there were no decrease in the yield stress, $\sigma_y(T)$, for the shock processed material. Combining the data of Figs. 12 and 18(b) allows the approximate yield stress of the shock processed material along the axis to be determined and this information is also depicted in Fig. 18(a). Along the axis the $p_{dyn} = 3.4$ kb surface corresponds to a yield stress of $\sigma_y(T) = 0.3$ kb and, consequently, does not satisfy criterion (5.2). The solid curve in Fig. 18(a) represents the approximate envelope of the depths corresponding to $p_{dyn} = 1.8$ kb and, since it corresponds to a residual yield stress of approximately the same value, it represents the predicted crater surface according to criterion (5.2). For the crater thus defined:

$$P_c / \ell = 2.1 , \qquad R_c / \ell = 2.4, \qquad P_c / R_c = 0.87,$$

$$P_c = 1.03 \text{ cm}, \qquad R_c = 1.17 \text{ cm} \qquad (6.1)$$

2. In Figs. 19(a) and 19(b) the initial stages of the flow process are depicted for the case of a β-projectile impacting at $v_o = 0.735$ cm/μsec, problem N6. The combination of low bulk density and low impact velocity prevented the VISTA calculations from being carried until the projectile had buried itself into the target. The discrete mass representation used in VISTA did not permit an adequate resolution of the low pressures produced. Consequently, the LINK process was employed at $t = 0.4354 \mu$sec and the calculations continued with PICWICK III. The subsequent mass flux field is illustrated by the graphical displays in Figs. 19(c) and 19(d).

For the much higher impact velocity treated in problem N7, the β-projectile is completely buried, Figs. 20(a) and 20(b), and is then blown backwards out of the forming crater, Figs. 20(c) through 20(f), prior to the LINK at $t = 0.4110 \mu$sec. Representative mass flux fields computed with PICWICK III are given in Figs. 20(g) and 20(h).

The time variation of the partition of the total axial momentum, scalar radial momentum, and total energy between projectile and target materials during the VISTA calculations are shown in Figs. 21 and 22 for problems N6 and N7 respectively. For problem N6, 50% of the total axial momentum and 60% of the total energy still remains in the projectile at the time it was necessary to make the LINK calculations. For the much higher impact

velocity, $v_o = 5.0$ cm/μsec, in problem N7, less than 5% of the total energy in the mesh remains in the projectile material at the time of the LINK process. Much of this, moreover, remains in the back splash since the total axial momentum in the projectile is negative at $t = 0.4110\,\mu$sec.

For problem N6, application of the strength dependent dynamic pressure criterion, (5.2), is made in Fig. 23. The predicted crater dimensions are as follows:

$$P_c/\ell = 1.0\,, \qquad R_c/\ell = 1.2, \qquad P_c/R_c = 0.83,$$

$$P_c = 0.49\,, \qquad R_c = 0.59\text{ cm} \qquad\qquad (6.2)$$

The application of the criterion for problem N7, given in Fig. 24, predicts the following crater dimensions:

$$P_c/\ell = 3.9\,, \qquad R_c/\ell = 4.3\,, \qquad P_c/R_c = 0.91\,,$$

$$P_c = 1.91\text{ cm,} \qquad R_c = 2.10\text{ cm} \qquad\qquad (6.3)$$

6.2   Heterogeneous γ-Projectile (Problem N4)

The early stage mechanisms resulting from a γ-projectile impacting at $v_o = 2.0$ cm/μsec are depicted in Figs. 25(a) through 25(g), problem N4. The results are similar to those for problem N3 in that the heterogeneity of the projectile produces an irregular flow field. The VISTA calculations were continued to $t = 0.766\,\mu$sec at which time the LINK program was employed. The low density region at the axis of symmetry, apparent in Figs. 25(g) and 25(h), was smoothed during the process and the computations continued with PICWICK III. The mass flux fields computed during later stages again show the separation into two principal regions, Figs. 25(i) and 25(j). The finite difference mesh was rezoned between the times depicted in these last two graphical displays.

The partition of the total axial momentum, scalar radial momentum, and total energy between projectile and target materials for time prior to the LINK process are depicted in Fig. 26, for problem N4. Less than 10% of each is contained in the projectile material at the time the PICWICK III calculations are initiated.

The strength dependent dynamic pressure criterion, (5.2), has again been applied to determine the final crater dimensions for problem N4. In Fig. 27, the dynamic pressure in the regions surrounding the forming crater equals the residual yield stress at the value of 1.2 kb. Accordingly, the predicted crater surface, shown there, has the following dimensions:

$$P_c/\ell = 2.3, \qquad R_c/\ell = 2.5, \qquad P_c/R_c = 0.92,$$

$$P_c = 1.12 \text{ cm}, \qquad R_c = 1.22 \text{ cm} \qquad (6.4)$$

6.3 Homogeneous δ-Projectile (Problem N5)

Quite different mechanisms are produced by the homogeneous low density δ -projectile impacting at $v_o = 2.0$ cm/μ sec. In this case, problem N5, the projectile is not rapidly torn apart by inner and outer radial flow, but is almost uniaxially compressed until the crush up wave travels upward to the rear surface of the projectile, Figs. 28(a) through 28(d). Equal pressures are obtained in the projectile and target at the interface, but the mass density of the target material remains greater than the compressed projectile material. The specific internal energy in the projectile material is correspondingly higher than it is in the target material.

Some caution must be exercised in interpreting the graphical displays of the projectile-target configurations for problem N5. The mass particles representing the projectile material, are less than one-fifth the mass of those representing the target material at a given initial radial position. The greater density of the dots representing the mass particles in the projectile material, Figs. 28(a), 28(c), and 28(e), actually corresponds to a smaller mass density than in the neighboring target material. What appears to be a very low density region just below the interface in these plots reflects this situation. The mass density in this region of the configuration is actually greater than that of the adjacent projectile material. The rarefaction wave originating from the rear surface of the crushed up projectile leaves the low density material with a very high residual internal energy. This causes a rapid blow-off of the projectile material, Figs. 28(g) and 28(h).

The VISTA calculations were terminated at t = 0.7117μsec and the LINK made with PICWICK III. Representative mass flux plots made subsequent to rezoning the PICWICK III finite difference mesh are shown in Figs. 28(i) and 28(j).

The partition of the total axial momentum, scalar radial momentum, and total energy between projectile and target materials for times prior to the LINK process are depicted in Fig. 29 for problem N5. The content of the projectile material at the time of the LINK process is less than 10% except for the energy content. Much of the 25% of the energy remaining in the projectile is contained in that blown-off from the forming crater, as depicted in Fig. 28(h).

For problem N5, application of criterion (5.2) is made in Fig. 30. The predicted crater dimensions are as follows:

$$P_c/\ell = 2.4, \qquad R_c/\ell = 2.7, \qquad P_c/R_c = 0.89,$$

$$P_c = 1.17 \text{ cm}, \qquad R_c = 1.32 \text{ cm} \qquad (6.5)$$

VII. COMPARISON OF RESULTS

In Table V the predicted crater characteristics are summarized for all of the seven problems treated in this study. The dimensionless crater characteristics (P_c/ℓ, R_c/ℓ, P_c/R_c) and the predicted crater depth (P_c) and radius (R_c), which have been listed earlier for the various impact conditions, are presented. Also listed is the approximate volume of each of the craters, computed from

$$V_c \doteq \frac{2}{3} \pi P_c R_c^2 \ . \tag{7.1}$$

These values divided by the projectile kinetic energy, V_c/E_o, represent the cratering efficiency,

$$\frac{V_c}{E_o} \doteq \frac{4\pi}{3 v_o^2} \left(\frac{P_c}{M_o^{1/3}} \right) \left(\frac{R_c}{M_o^{1/3}} \right)^2 \tag{7.2}$$

Since an uncertainty of 5% in the linear dimensions, P_c and R_c, results in an uncertainty of 15% in V_c/E_o, however, the values of $\sqrt[3]{V_c/E_o}$ are also given in Table V. Finally, the predicted crater depth and radius, normalized through division by the cube root of the projectile mass, are also listed.

In Section 5.4 it was found that the normal density α-projectile impacting at $v_o = 0.735$ cm/μsec, problem N1, and at $v_o = 2.0$ cm/μsec, problem N2, produced flow fields satisfying the late-stage equivalence criterion. It is also of interest to compare the flow fields produced by two projectiles of the same velocity and mass but with different distribution of the mass. This is the case, for example, in problems N2 and N3 in which the α- and β-projectiles impact at $v_o = 2.0$ cm/μsec.

In Fig. 31(a) the time dependent values of Z_+ and R_+ are depicted for problems N2 and N3. The time dependent positions of the shock front in the target, for each of the two cases, are shown in Fig. 31(b). From this latter figure it is seen that the shock produced by the heterogeneous projectile lags the one produced by the normal density projectile only by approximately $\Delta t \doteq 0.1$ μsec. A corresponding correction of the time scale for the R_+ and Z_+ curves associated with problem N3, Fig. 31(a) would still leave them very far apart. It is apparent that the late-stage equivalence criterion cannot be applied to these two problems even though the momentum and energy delivered by the projectiles are identical. This negative result is consistent with the fact that the crater predictions arrived at through the application of

the dynamic pressure criterion are different, Table V. The low bulk density of the projectile in problem N3 results in a decrease in crater depth of about 20%, but an increase in the radius of the crater of approximately 6%. If late-stage equivalence were actually obtained, the final crater shapes and dimensions for problems N2 and N3 would be predicted to be the same.

The velocity dependence of crater depth for the β-projectile is given by the results of problems N3, N6 and N7, Table V. For the velocity range $0.735 \leqq v_o \leqq 2.0$ cm/μsec the results for N6 and N3 imply that the exponent α, for the velocity dependence $P_c \sim v_o^\alpha$, is determined by

$$\left(\frac{2.0}{.735}\right)^\alpha = \frac{2.1}{1.0} \quad \text{whence} \quad \alpha = \frac{\log 2.1}{\log 2.72} = 0.74 \quad (7.3)$$

For the velocity range $2.0 \leqq v_o \leqq 5.0$ the results for N3 and N7 imply a value determined by

$$\left(\frac{5.0}{2.0}\right)^\alpha = \frac{3.9}{2.1} \quad \text{whence} \quad \alpha = \frac{\log 1.86}{\log 2.5} = 0.68 \quad (7.4)$$

The relatively high values of α reflect the reduction in the penetrating ability of the low density projectiles for lower velocities. These values for the exponent are subject to the same uncertainties as the value $\alpha = 0.60$ associated with a normal density projectile (see Section 5.4).

The predicted crater depths for all seven problems, normalized through division by the cube root of the projectile mass, are displayed as a function of impact velocity in Fig. 32. From this $P_c/M_o^{1/3}$ vs v_o plot, the overall effects of the mass distribution of the projectile on its penetrating ability in an aluminum alloy AL-2024 T6 target are clearly demonstrated:

1. At $v_o = 0.735$ cm/μsec the heterogeneous β-projectile of average bulk density 0.5 gm/cc produces a crater approximately 75% as deep as that produced by the normal density, $\rho_o = 2.7$ gm/cc, α-projectile of the same mass.

2. At $v_o = 2.0$ cm/μsec the heterogeneous β- and γ-projectiles and the homogeneous δ-projectile, all of average bulk density 0.5 gm/cc, produce craters of depths from 85% to 95% as deep as that produced by the normal density α-projectile. The 85% corresponds to the β-projectile and the 95% corresponds to the homogeneous δ-projectile.

3. At $v_o = 5.0$ cm/μsec the heterogeneous β-projectile produces a crater approximately 90% as great as the extrapolated value of crater depth for the normal density α-projectile.

The normalized values of the predicted crater radii for all seven problems are displayed as a function of impact velocity in Fig. 33. The lines through the data corresponding to the heterogeneous β-projectile and the normal density α-projectile do not bracket the γ- and δ- projectile data as is the case in Fig. 32. This reflects the fact that the depth of the crater for the normal density α-projectile exceeds its radius by about 10%, Table V. For the low density β-, γ-, and δ-projectiles, however, the opposite is true, the depth being from 83% to 92% of the radius.

In Fig. 34 the parameter $\sqrt[3]{V_c/E_0}$ is presented as a function of impact velocity for all seven problems treated. For a given projectile geometry the value tends to decrease slightly with increasing impact velocity. At $v_0 = 2.0$ cm/μsec, the homogeneous δ-projectile removes a greater amount of target material than do the other three configurations.

In an early study (ref. 26), a particle-in-cell code of much lower resolution than VISTA was employed and the equation of state (3.1) was used for both the aluminum target and homogeneous aluminum projectiles of densities 0.44, 0.90, and 2.7 gm/cc. Calculations were made only for $v_0 = 2.0$ cm/μsec. The present more careful treatment for homogeneous projectiles of density 0.5 and 2.7 gm/cc impacting at $v_0 = 2.0$ cm/μsec (problems N2 and N5) predicts that the final crater depths for the two densities differ by 5%, a difference not evident in the earlier study.

The calculated results here may also be compared where there is overlap with those reported in ref. 17. In ref. 17, the dynamic pressure criterion was employed in the particle-in-cell calculations for homogeneous reduced-density projectiles impacting thick steel and aluminum targets. Homogeneous aluminum projectiles of densities 0.44 and 2.7 gm/cc were treated for impact onto aluminum targets (AL-2024 T3) at $v_0 = 2.0$ and 7.2 cm/μsec. The crater depths and crater volumes predicted in ref. 17 for these four problems are also shown in Figs. 32 and 34 respectively. Although ref. 17 does not explicitly present the associated predictions for the crater radius, relation (7.2) has been employed to estimate $R_c/M_0^{1/3}$ from the listed values of V_c/E_0 and $P_c/M_0^{1/3}$. The four values obtained are shown in Fig. 33.

These four normalized crater depth estimates, together with the present predictions, are also displayed in Fig. 35 where dashed lines join points corresponding to low density and normal density homogeneous projectiles of the same impact velocity. The slopes of the dashed lines are quite small as is the slope of the solid line joining the present predictions for the δ- and α-projectiles at impact velocity of $v_0 = 2.0$ cm/μsec (problems N2 and N5). There is agreement relative to the insensitivity of the penetration of homogeneous projectiles to projectile density in the impact range $v_0 \cong 2.0$ cm/μsec. However, the current study shows a significant bulk density sensitivity for heterogeneous projectiles.

VIII. CONCLUSIONS

The shape and size of a crater formed in a thick 2024 T6 aluminum alloy target vary significantly with the structure and bulk density of the projectile. The craters produced by the reduced density projectiles are shallower and wider. The effect is greater for reduced density heterogeneous projectiles than for a homogeneous projectile of the same velocity and average bulk density. The effect diminishes with an increase in impact velocity, but remains significant throughout the meteoroid velocity range.

SYMBOLS

A	constant in relation $D = A + Bu$
B	constant in relation $D = A + Bu$
D	shock velocity
E	total energy
E_o	projectile impact energy
F	shock polar function
h	radial dimension of finite difference cell
I	internal energy per unit mass
k	axial dimension of finite difference cell
ℓ	length of unit aspect cylindrical projectile
m	porosity ratio, $\rho_o / \bar{\rho}_o$
M	total mass
M_o	projectile mass
p	thermodynamic pressure
P_{dyn}	dynamic pressure
P_c	crater depth
r	radial coordinate
R	total radial momentum
R_c	crater radius
$\dot{R}_H$	shock velocity
T	temperature
u	radial particle velocity

v	axial particle velocity
v_o	impact velocity
V_c	crater volume
Z	total axial momentum
α	exponents in relation $P_c \sim v_o^{\alpha}$
α	homogeneous projectile of normal density
β	first heterogeneous projectile of reduced density
γ	second hetereogeneous projectile of reduced density
δ	homogeneous projectile of reduced density
η	density ratio, ρ/ρ_o
λ	$1/m$
ρ	mass per unit volume
ρ_o	normal density
$\bar{\rho}_o$	bulk density
σ_y	yield stress of target

Subscripts

H	Hugoniot value
i	column i of finite difference mesh
j	row j of finite difference mesh
+	denotes sum of positive components

Superscripts

n	n-th time cycle
$\sim$	denotes value at end of phase 1 calculations
$'$	denotes scaled value

38

REFERENCES

1. Loeffler, I. J.; Lieblein, Seymour; and Clough, Nestor: Meteoroid Protection for Space Radiators. Power Systems for Space Flight. Progress in Astronautics and Aeronautics, Vol. 11, M. Zipkin and R. N. Edwards, eds., Academic Press, Inc., 1963, pp. 551-579.

2. Lieblein, Seymour; Clough, Nestor; and McMillan, A. R.: Hypervelocity Impact Damage Characteristics in Armored Space Radiator Tubes. NASA TN D-2472, 1964.

3. Clough, Nestor; McMillan, A. R.; and Lieblein, Seymour: Dimple, Spall, and Perforation Characteristics in Aluminum, Columbium, and Steel Plates under Hypervelocity Impact. NASA TN D-3468, 1966.

4. Clough, Nestor; and Lieblein, Seymour: Significance of Photographic Meteor Data in the Design of Meteoroid Protection for Large Space Vehicles. NASA TN D-2958, 1965.

5. Heyda, J. F.: The Plate-Gap Model of a Porous Solid and its Application to Impact by Reduced Density Projectiles. NASA Contractor Report, NAS 3-8512, 1967.

6. Sedgwick, R. T.: Theoretical Study of Size Scaling in Cratering Resulting from Hypervelocity Impact. NASA Contractor Report, NAS 8-20239, 1966.

7. Halda, E. J.; and Riney, T. D.: VISTA - A Two-Dimensional Particle-in-Cell Code for Three Materials. Document No. 66SD409, Contract AF 04(694)-667, 1966.

8. Johnson, W. E.: OIL - A Continuous Two-Dimensional Eulerian Hydrodynamic Code. Document No. GAMD-5580, Contract DA-04-495-AMC-116, 1965.

9. Evans, M. W.; and Harlow, F. H.: The Particle-in-Cell Method for Hydrodynamic Calculations. Los Alamos Scientific Laboratory Report LA-2139, 1957.

10. Harlow, F. H.: Two-Dimensional Hydrodynamic Calculations, Los Alamos Scientific Laboratory Report LA-2301, 1959.

11. Bjork, R. L.; Brooks, N. B.; and Papetti, R.: A Numerical Technique for Solution of Multidimension Hydrodynamic Problems. The Rand Corporation Report RM 2628-PR, 1963.

12. Rich, M.: A Method for Eulerian Fluid Dynamics. Los Alamos Scientific Laboratory Report LAMS, 1963.

13. Gentry, R. A.; Martin, R. E.; and Daly, B. J.: An Eulerian Differencing Method for Unsteady Compressible Flow Problems Journal of Computational Physics, 1966.

14. Jewell, J. G.: Analysis of Some Numerical Problems Encountered in Solving Equations Describing Meteoroid Impact. Unpublished report submitted under Contract NAS 3-8512, August 1966.

15. Riney, T. D.: Theoretical Hypervelocity Impact Calculations Using the PICWICK Code. Document No. ATL-TDR-64-8, Contract AF 08(635)-3781, 1964.

16. Walsh, J. M.; and Tillotson, J. H.: Hydrodynamics of Hypervelocity Impact. Document No. GA-3827, Contract AF 29 (601)-4759, 1963.

17. Bjork, R. L.; Kreyenhagen, K. N.; and Wagner, M. J.: Analytical Study of Impact Effects as Applied to the Meteoroid Hazard. NASA CR-757, 1967.

18. Kormer, S. B., Funtikov, A. I., Urlin, V. D., and Kolesnikova, A. N.: Dynamic Compression of Porous Metals, Soviet Physics JETP, Vol. 15, No. 3, September 1962, pp. 477-488.

19. McCloskey, D. J.: An Analytic Formulation of Equation of State. The Rand Corporation Report RM-3095-PR, 1964.

20. Thouvenin, J.: Action d'une Onde de Choc sur un Solide Poreaux, Fourth Symposium on Detonation, U.S. Naval Ordnance Laboratory, Silver Spring, Maryland, Vol. B, October 1965, pp. 146-155.

21. Heyda, J. J.: and Riney, T. D.: Peak Pressures in Thick Targets Generated by Reduced Density Projectiles. NASA CR-609, 1966.

22. Eichelberger, R. J.: Experimental Test of the Theory of Penetration by Metallic Jets. Jour. Appl. Phys. Vol. 27, No. 1, 63-8 (1956).

23. Anon.: Alcoa Aluminum Handbood. Published by Aluminum Company of America, Pittsburgh, Penna. p. 20 and p. 26.

24. Halperson, S. M.: Some Phenomena Associated with Impacts into Aluminum. Proc. Sixth Hypervelocity Impact Symposium, Vol. 2, Part 2, 1963.

25.   Halperson, S. M.: Comparisons Between Hydrodynamic Theory and
       Impact Experiments. Proc. Seventh Hypervelocity Impact Symposium,
       Vol. 5, 1965.

26.   Riney, T. D., and Heyda, J. F.: Hypervelocity Impact Calculations
       and Their Correlation with Experiments. Document No. ATL-TDR-
       64-64, Contract AF 08(635)-3781, 1964.

Table I. Equation of state constants for aluminum in the gram-centimeter-microsecond system of units (eq. 3.1). Pressure is expressed in megabars (mb).

ρ_o (gm/cc)	2.700
a_1 (mb^2)	1.1867
a_2 (mb^2)	0.7630
b_o (mb)	3.4448
b_1 (mb)	1.5451
b_2 (mb)	0.9643
c_o (gm/cc)	0.4338
c_1 (gm/cc)	0.5487
φ_o (mb)	1.5000

TABLE II. Specification of projectile configuration, projectile bulk density, and impact velocity for each of the seven problems treated

Problem	Projectile	$\bar{\rho}_o$ (gm/cc)	v_o (cm/μ sec)
N1	α	2.7	0.735
N2	α	2.7	2.0
N3	β	0.5	2.0
N4	γ	0.5	2.0
N5	δ	0.5	2.0
N6	β	0.5	0.735
N7	β	0.5	5.0

TABLE III. Initial pressure, shock velocity and compression in homogeneous projectiles and target at impact. Values computed using equations of state (3.1) and (3.22), respectively, for normal density and reduced density aluminum. Units are in the gram-centimeter-microsecond system.

	$v_o = 0.735$	$v_o = 2.0$	$v_o = 5.0$
A. Projectile and target of normal density aluminum			
P_H (mb)	1.032	4.904	24.0
$\dot{R}_H$ (cm/μsec)	1.039	1.810	3.550
ρ_H/ρ_o	1.547	2.242	3.390
B. Target of normal density aluminum and projectile of reduced density, 0.5 gm/cm^3, aluminum.			
P_H (mb)	0.238	1.498	8.408
$\dot{R}_H$ (Target) (cm/μsec)	0.712	1.174	2.248
$\dot{R}_H$ (Proj.) (cm/μsec)	0.777	1.961	4.649
ρ_H/ρ_o (Target)	1.210	1.672	2.601
ρ_H/ρ_o (Proj.)	0.869	0.838	0.833

TABLE IV. Experimental data giving crater depth produced in thick aluminum alloy targets by aluminum spherical projectiles. The primes denote the data extrapolated over the small changes of size and velocity required for comparison with the predicted value for problem N1. Units are in the gram-centimeter-microsecond system.

			REPORTED DATA			ADJUSTED VALUES			
Ref.	Shot #	Target	Impact Velocity v_o, cm/μsec	Projectile Mass M_o, gm	Crater Depth P_c, cm	Impact Velocity v_o', cm/μsec	Projectile Mass M_o', gm	Crater Depth P_c', cm	Deviation From Theoretical Prediction %
24	' -----	Al 2014 T6	.695	.377	1.28	.735	.04525	.663	+0.5
25	5-268	Al 2014 T6	.775	.158	0.98	.735	.04525	.680	+3.0
25	5-281	Al 2014 T6	.735	.158	1.00	.735	.04525	.636	-3.6
25	5-283	Al 2014 T6	.697	.158	0.96	.735	.04525	.660	0.0
*	D-906	Al 2024 T6	.753	.0473	0.69	.735	.04525	.702	+6.4
*	D-898	Al 2024 T6	.789	.0470	0.66	.735	.04525	.680	+3.0

*GM Defense Research Laboratories, NASA Contract No. NASW468.

TABLE V. Summary of predicted crater characteristics for the seven impact problems treated. Units are in the gram-centimeter-microsecond system.

Problem	Dimensionless Crater Characteristics			Crater Depth	Normalized Depth	Crater Radius	Normalized Radius	Crater Volume	Normalized Volume
	P_c/l	R_c/l	P_c/R_c	P_c, cm	$P_c/M_o^{1/3}$	R_c, cm	$R_c/M_o^{1/3}$	V_c, cc	$(V_c/E)^{1/3}$
N1	2.4	2.2	1.09	0.66	1.87	0.61	1.71	0.52	3.49
N2	4.4	4.0	1.10	1.22	3.43	1.11	3.12	3.15	3.30
N3	2.1	2.4	0.87	1.03	2.89	1.17	3.29	2.95	3.20
N4	2.3	2.5	0.92	1.12	3.15	1.22	3.43	3.50	3.38
N5	2.4	2.7	0.89	1.17	3.28	1.32	3.71	4.27	3.61
N6	1.0	1.2	0.83	0.49	1.38	0.59	1.66	0.35	3.07
N7	3.9	4.3	0.91	1.91	5.36	2.10	5.90	17.6	3.15
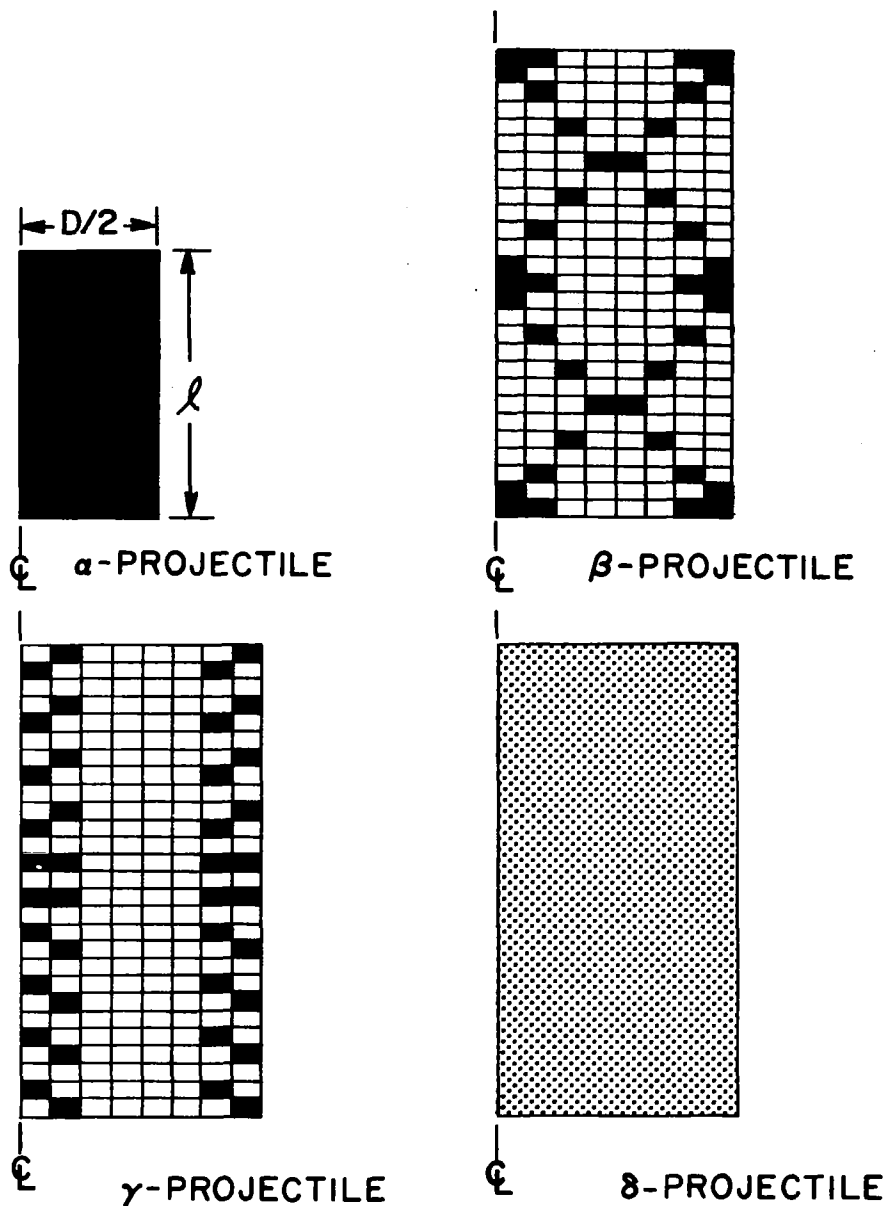
PROJ.	$\ell = D(CM)$	ρ_0 (GM/CC)	$\bar{\rho}_0$ (GM/CC)	MASS (GM)
α	.2774	2.7	2.7	.04525
β	.4886	2.7 OR 0	0.5	.04525
γ	.4886	2.7 OR 0	0.5	.04525
δ	.4886	0.5	0.5	.04525

N402-213

Figure 1. Axial sections depicting mass distribution in the four projectile configurations treated. The symbols ρ_0 and $\bar{\rho}_0$ denote the local and average densities respectively.
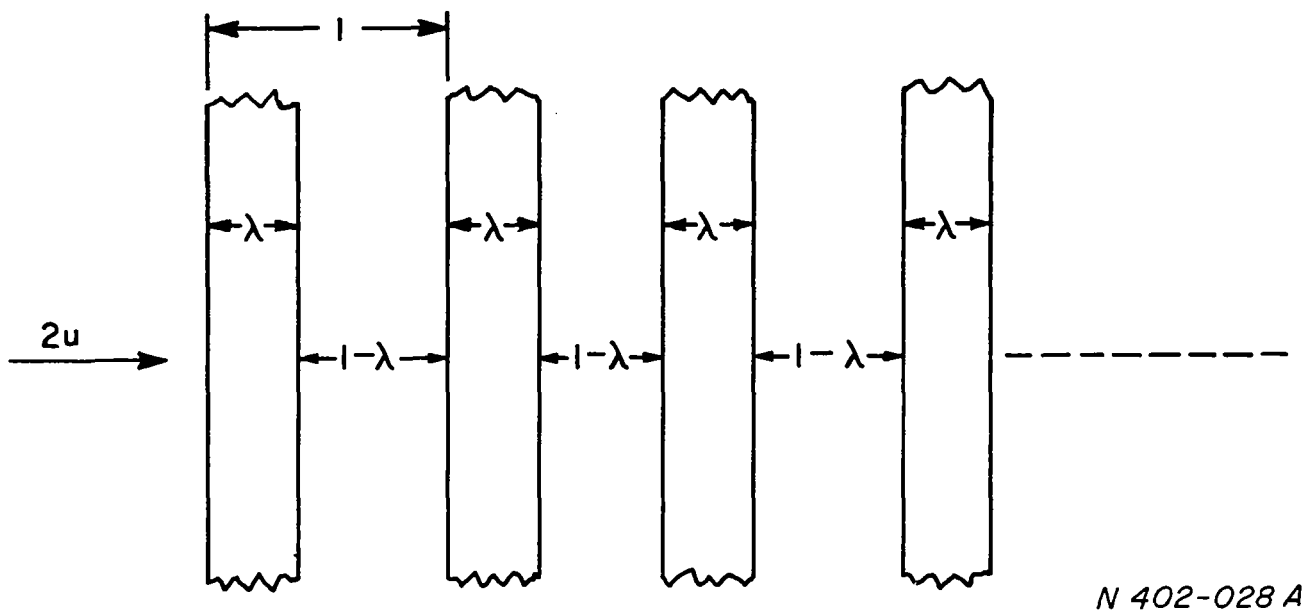
Figure 2. Plate-gap model of a porous solid.
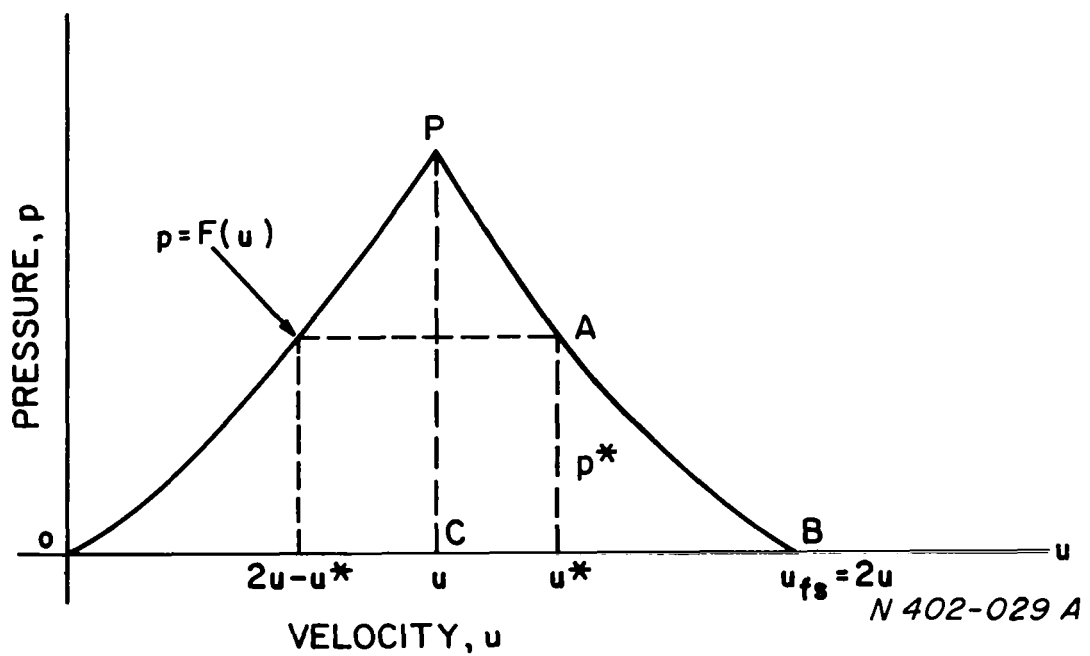
Figure 3. Loading and unloading paths for a porous solid.
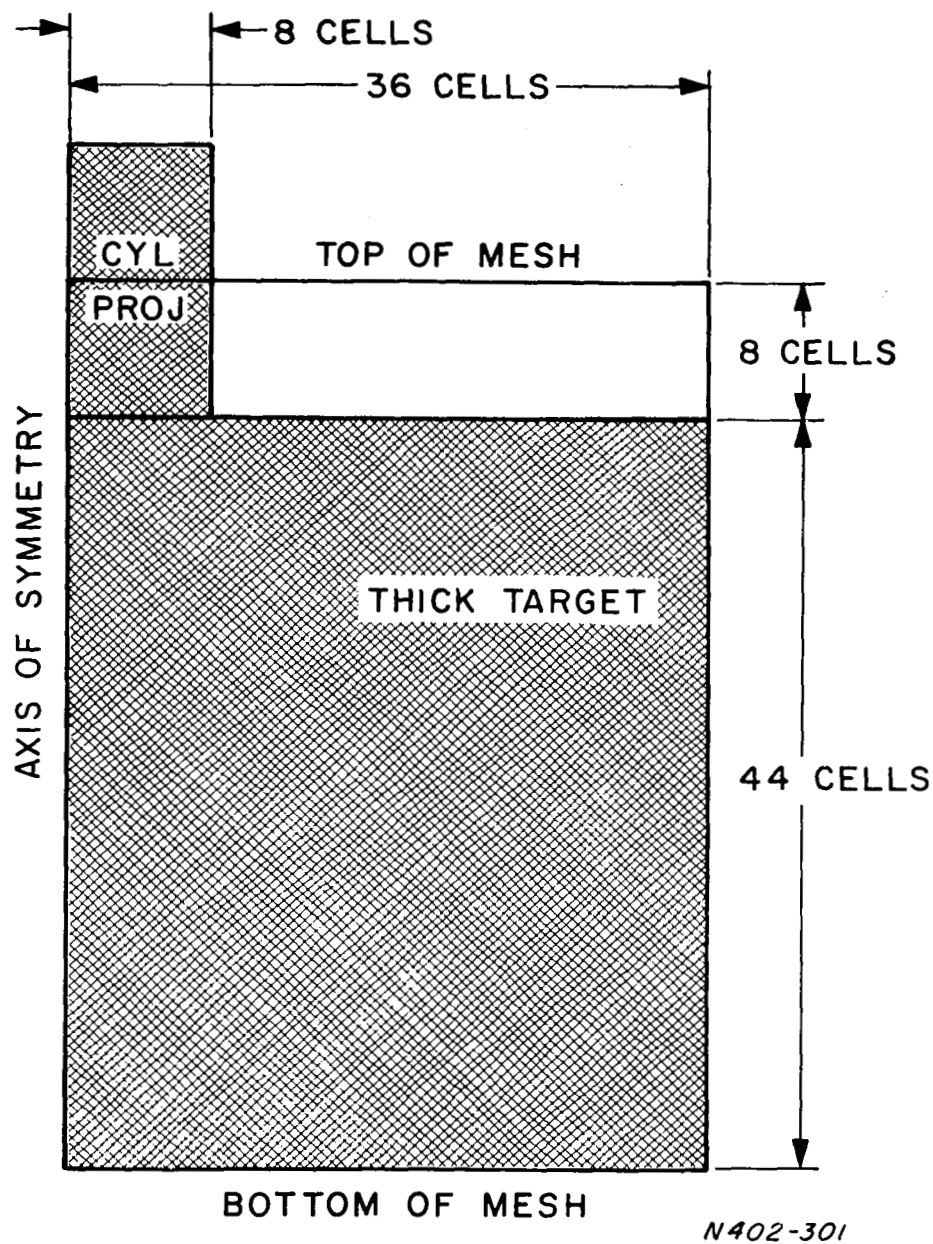
Figure 4. Schematic of finite difference mesh at initiation of calculations
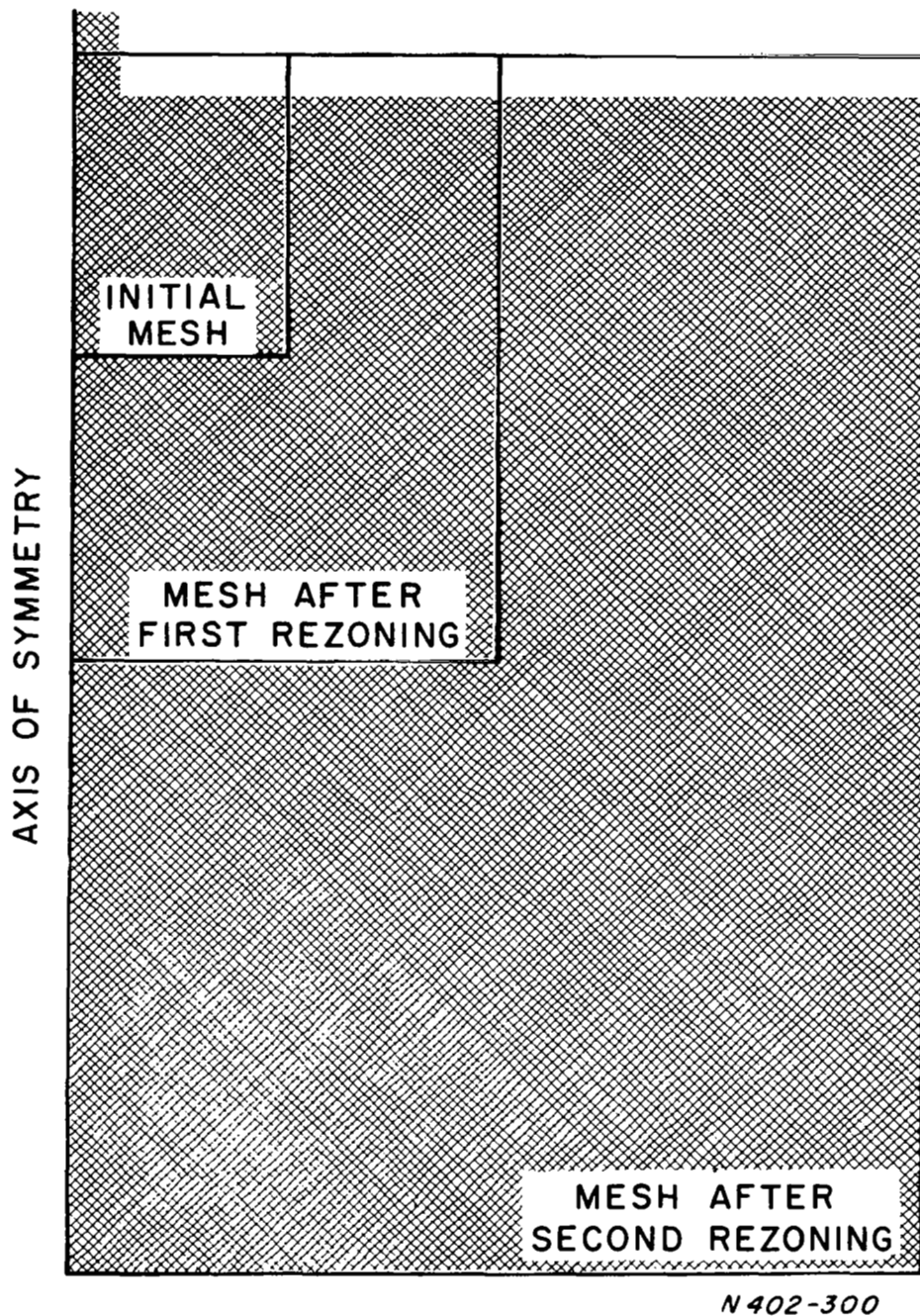
Figure 5. Enlargement of initial finite difference mesh by successive repartitions
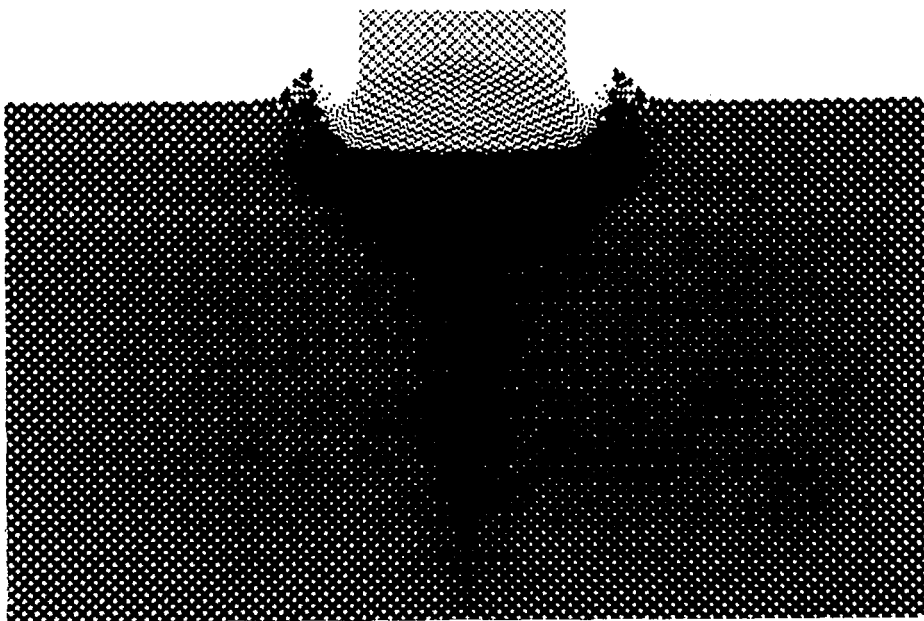
(a) Projectile-target configuration, t = 0.203 μsec (VISTA)
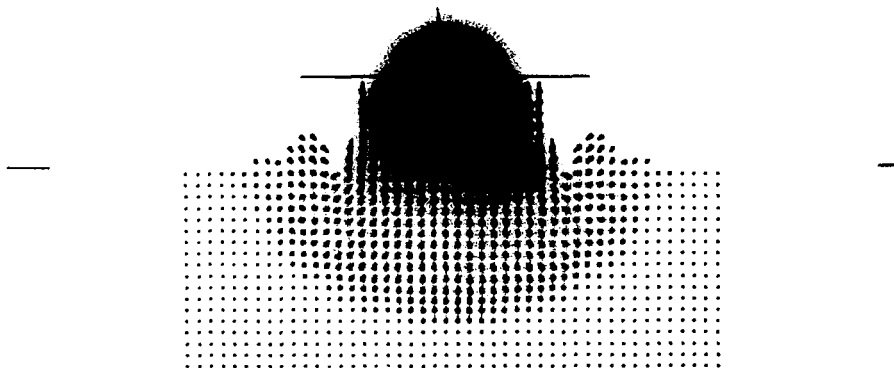
(b) Velocity field, t = 0.203 μsec (VISTA)

Figure 6. Normal-density projectile, problem N1: α-projectile impacting target at v_o = 0.735 cm/μsec. Graphical displays of projectile-target configuration, velocity field, and mass flux fields at indicated times.
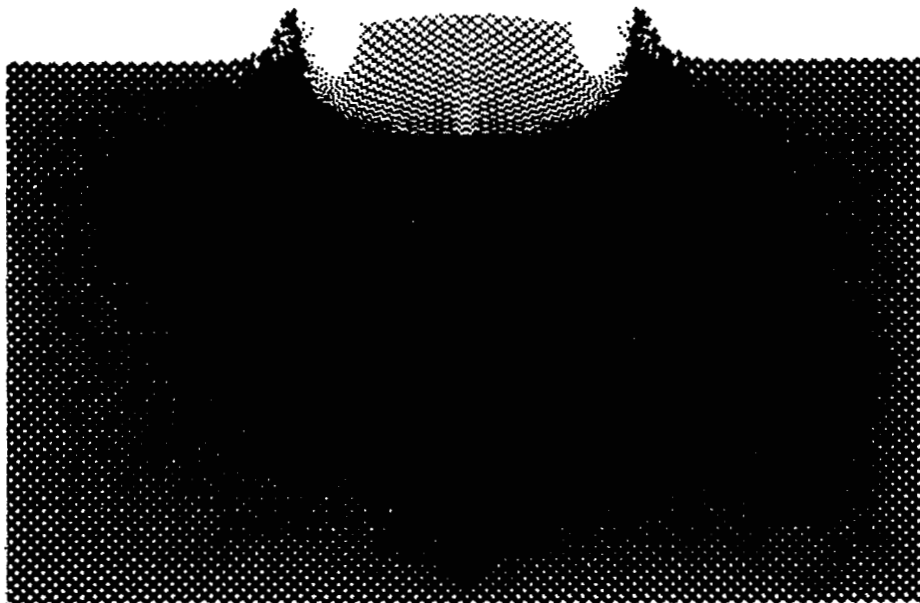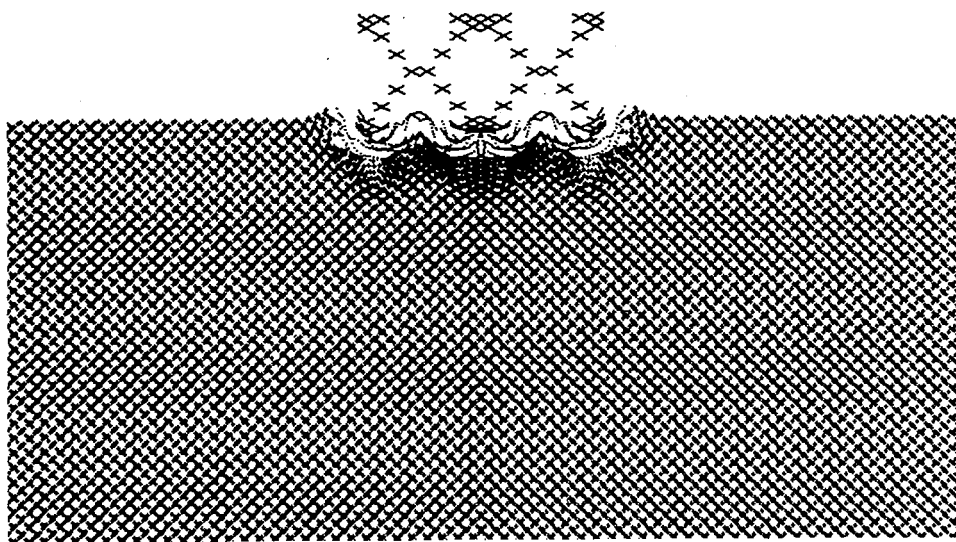
(c) Projectile-target configuration, t = 0.305 μsec (VISTA)
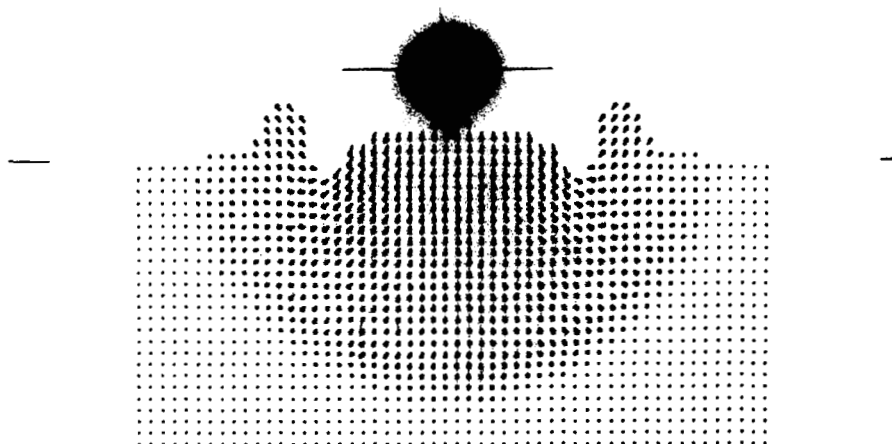
(d) Velocity field, t = 0.342 μ sec (VISTA)

Figure 6 continued.   Problem N1
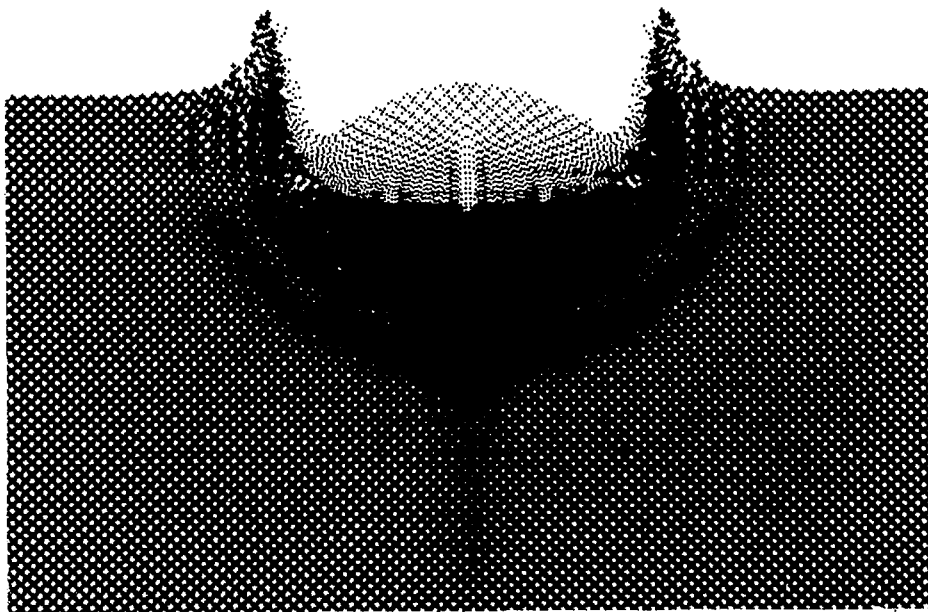
(e) Projectile-target configuration, t = 0.452 μsec (VISTA)
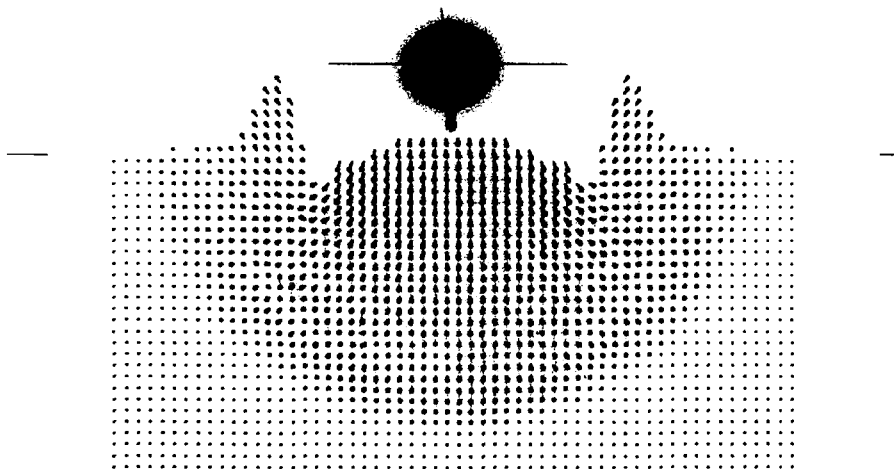
(f) Velocity field, t = 0.415 μsec (VISTA)

Figure 6 continued.   Problem N1
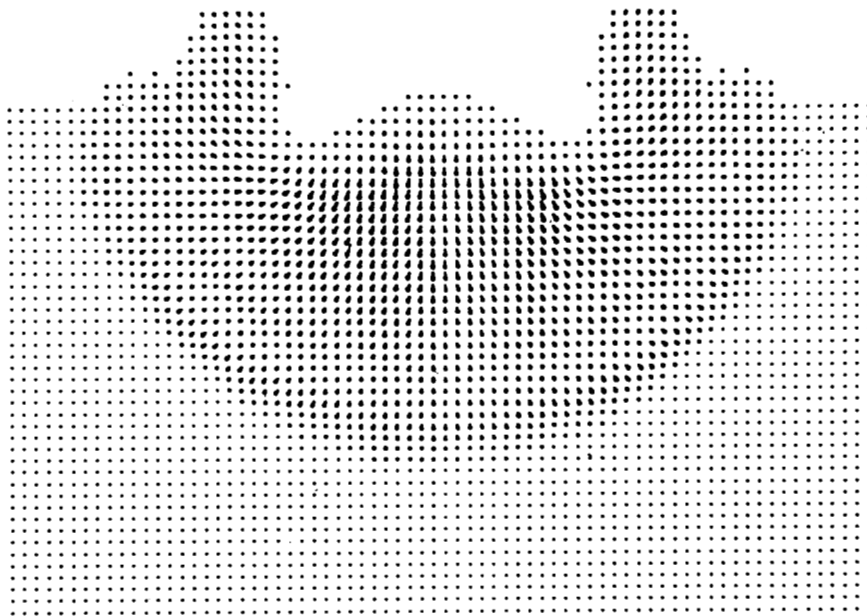
(g) Mass flux field, t = 0.584 μsec (PICWICK III)
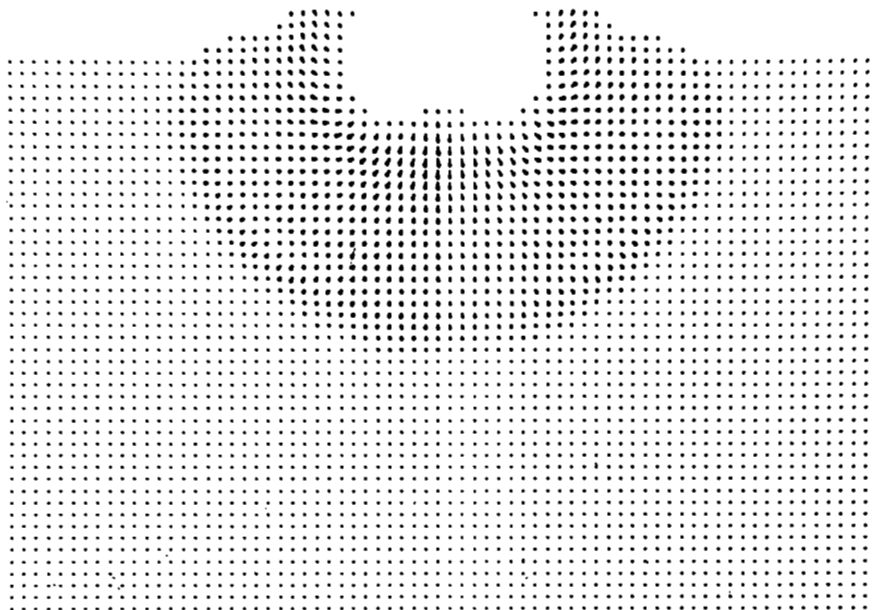
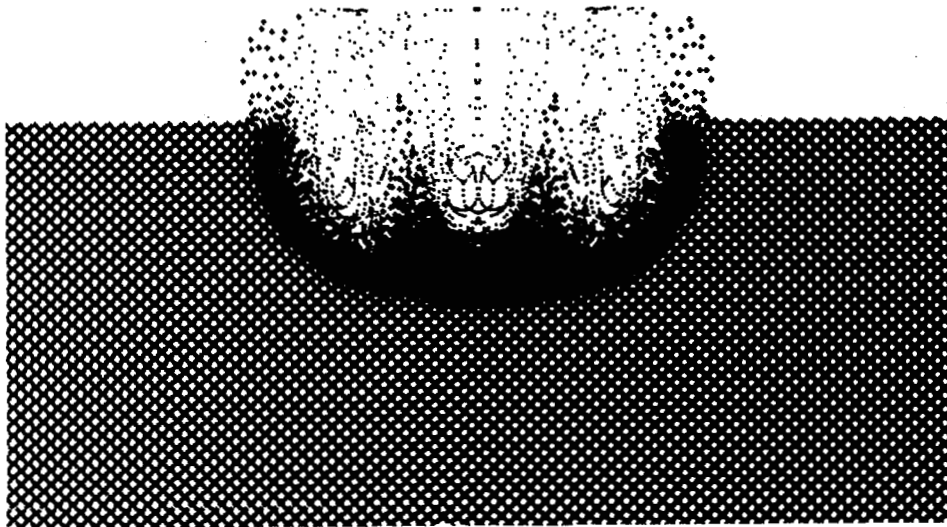(h) Mass flux field, t = 1.069 μsec (PICWICK III)

Figure 6 continued. Problem N1
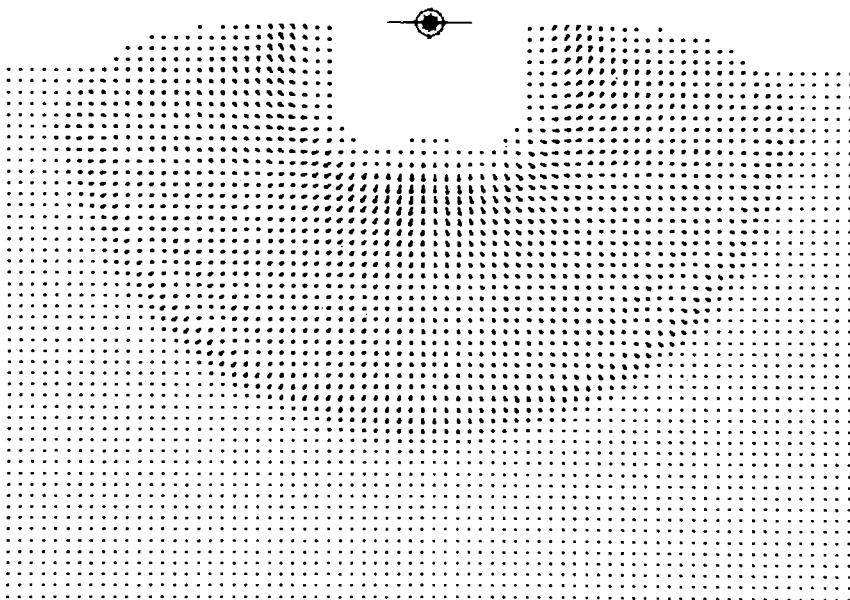
(i) Mass flux field, t = 1.623 μ sec (PICWICK III)
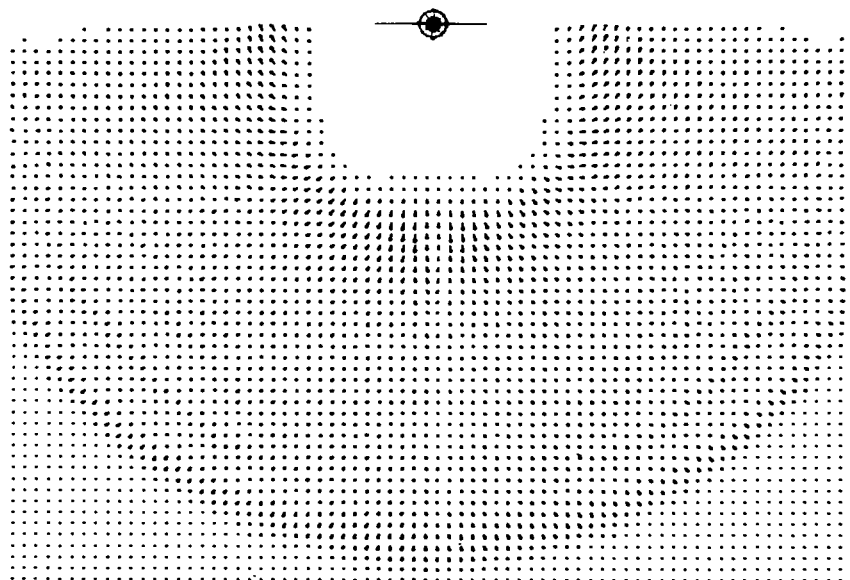
(j) Mass flux field, t = 2.297 μ sec (PICWICK III)

Figure 6 concluded. Problem N1

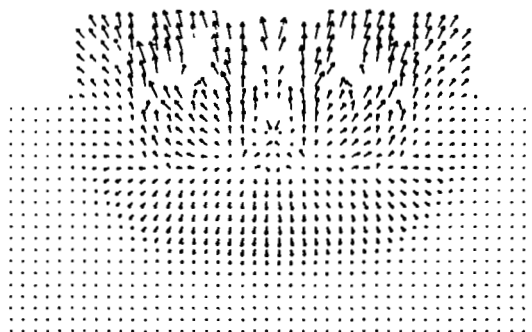(a) Projectile-target configuration, t = 0.158 μsec (VISTA)
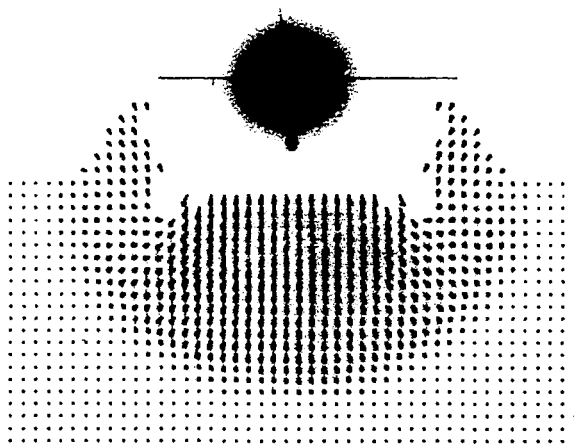
(b) Velocity field, t = 0.158μsec (VISTA)

Figure 7. Normal-density projectile, problem N2: α-projectile impacting
target at v_o = 2.0 cm/μsec. Graphical displays of projectile-
target configuration, velocity field, and mass flux field at indi-
cated times.
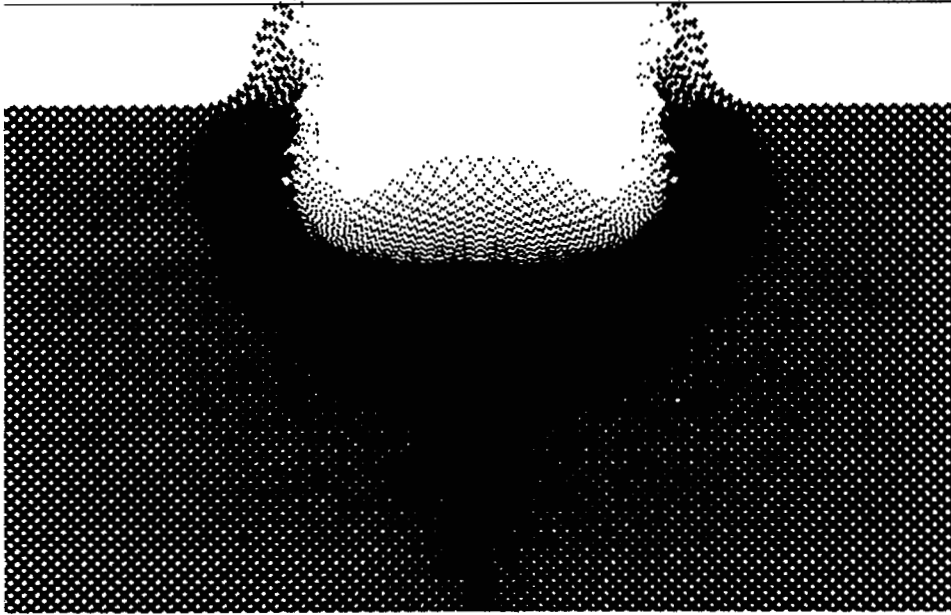
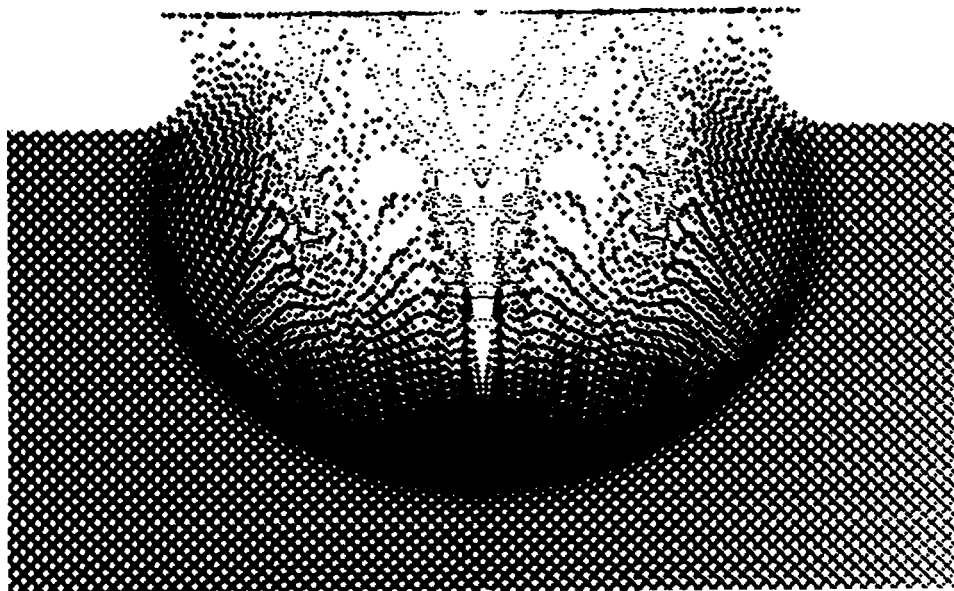(c) Projectile-target configuration, t = 0.247 μsec (VISTA)
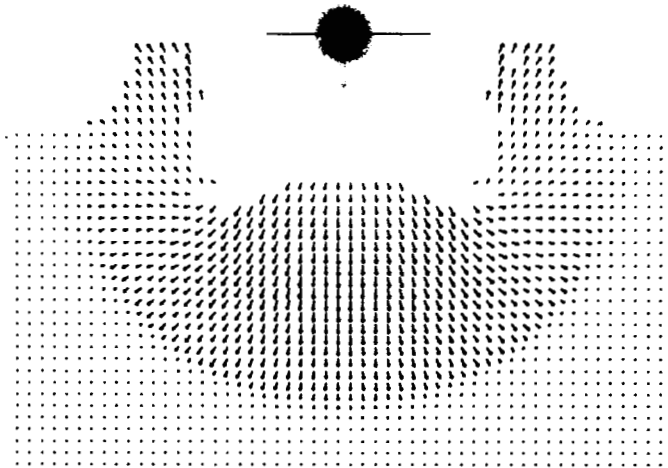
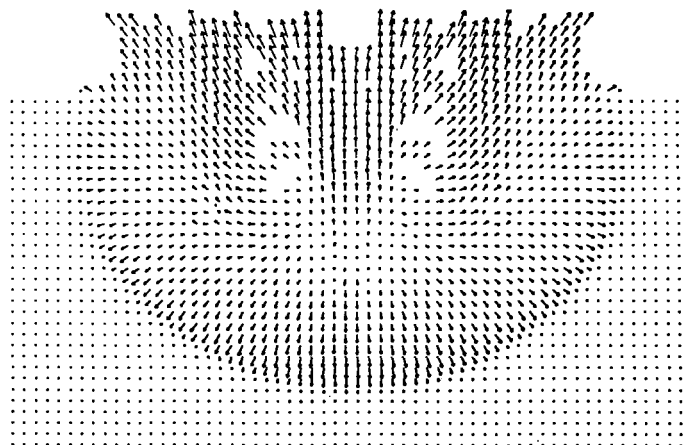(d) Velocity field, t = 0.247 μ sec (VISTA)

Figure 7 continued. Problem N2
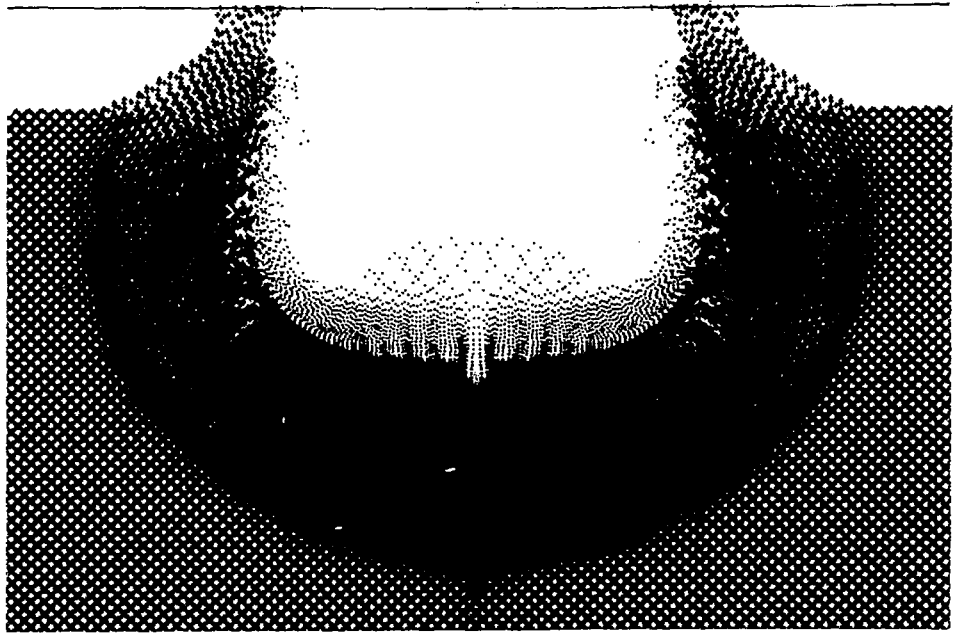
(e) Projectile-target configuration, t = 0.449 μsec (VISTA)
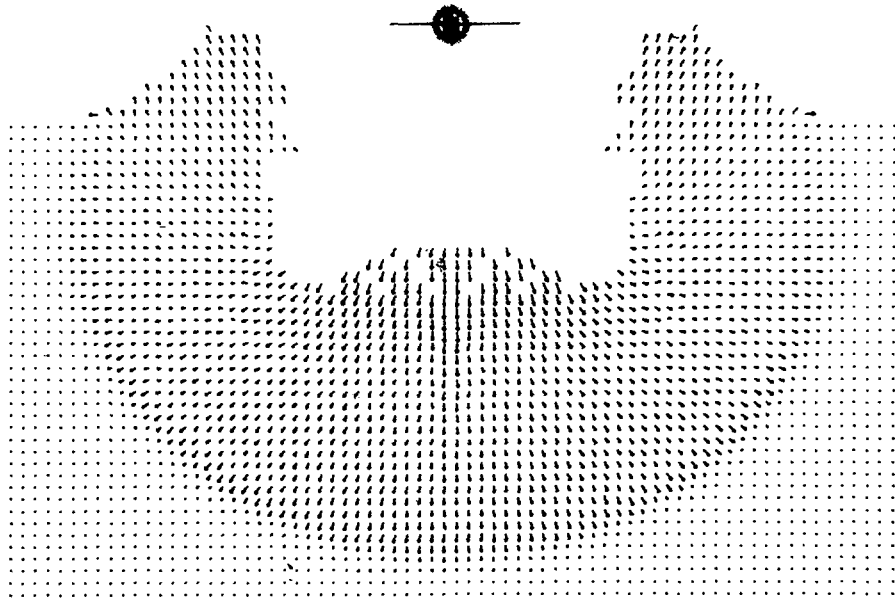
(f) Velocity field, t = 0.449 μsec (VISTA)

Figure 7 continued. Problem N2
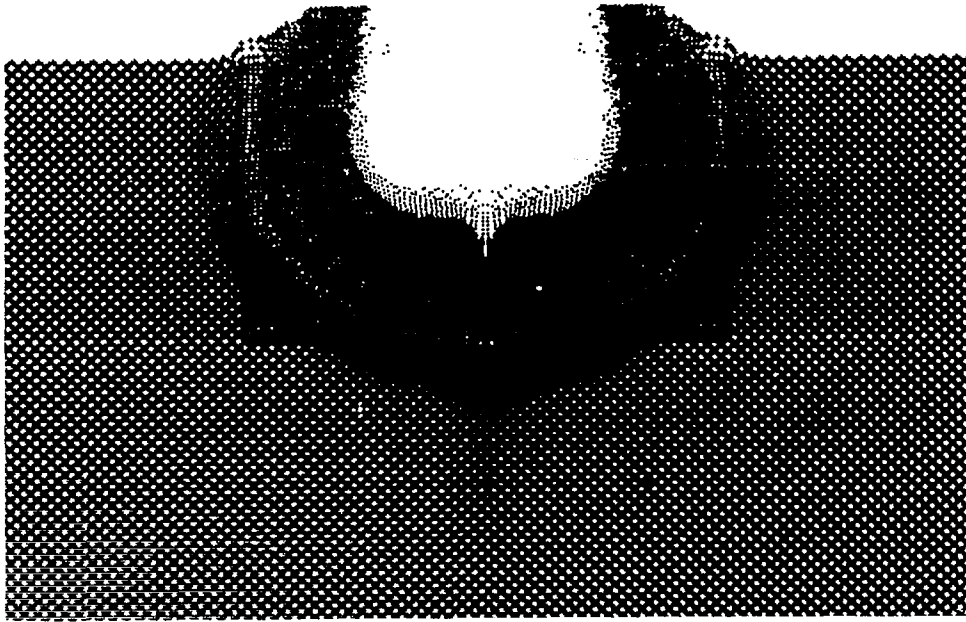
(g) Projectile-target configuration, t = 0.756 μsec (VISTA)
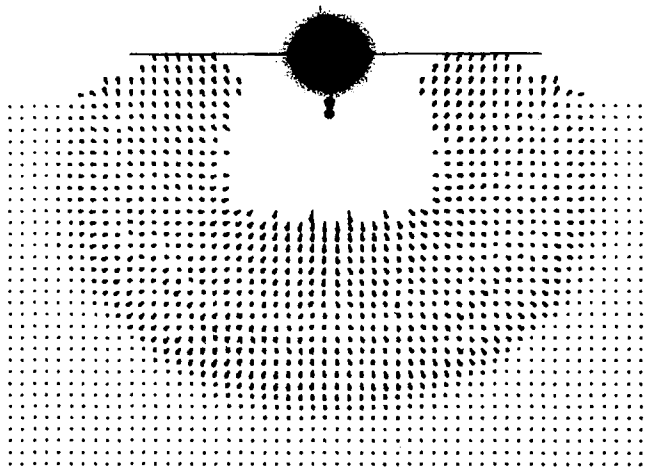
(h) Velocity field, t = 0.756 μsec (VISTA)

Figure 7 continued. Problem N2
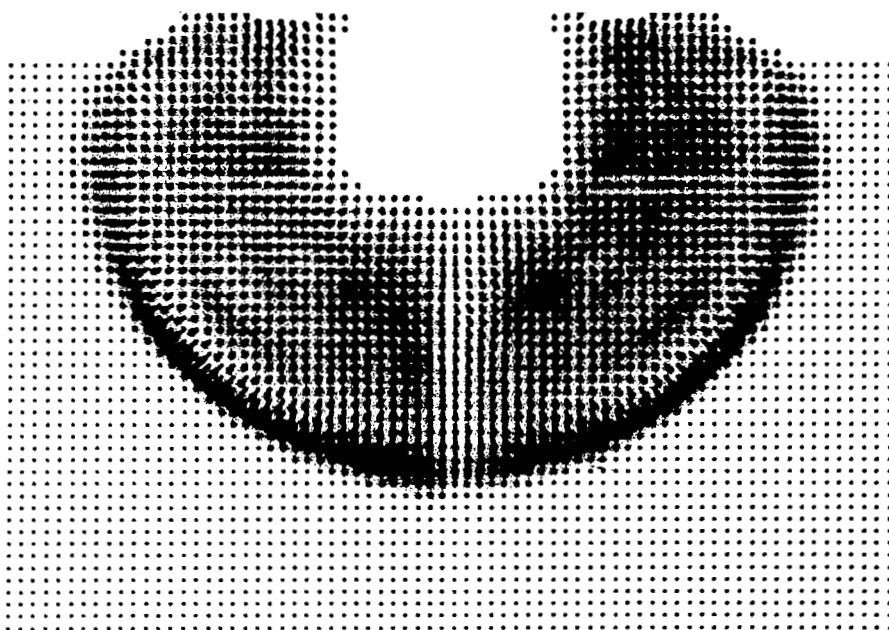
(i) Mass flux field, t = 1.113 μsec (PICWICK III)
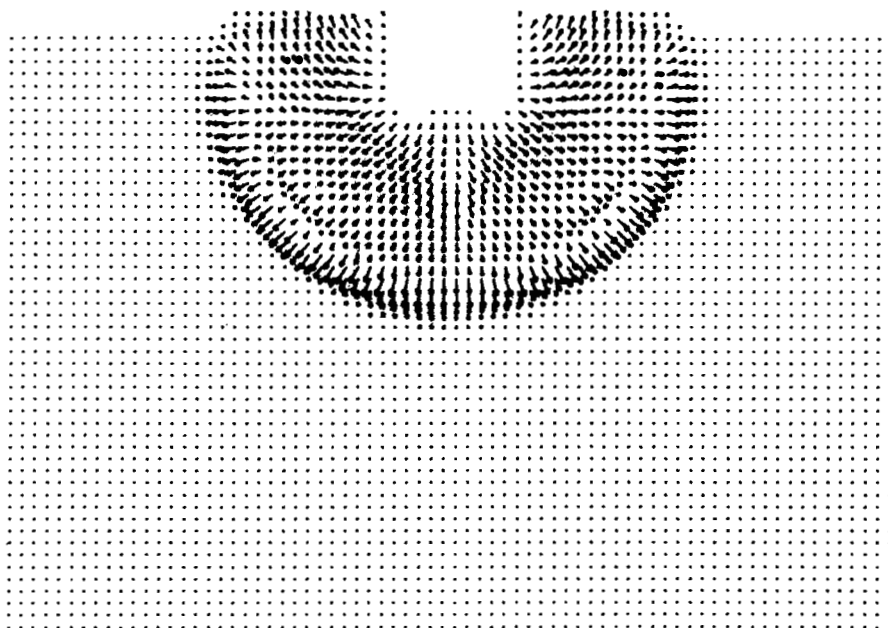
(j) Mass flux field, t = 1.699 μsec (PICWICK III)
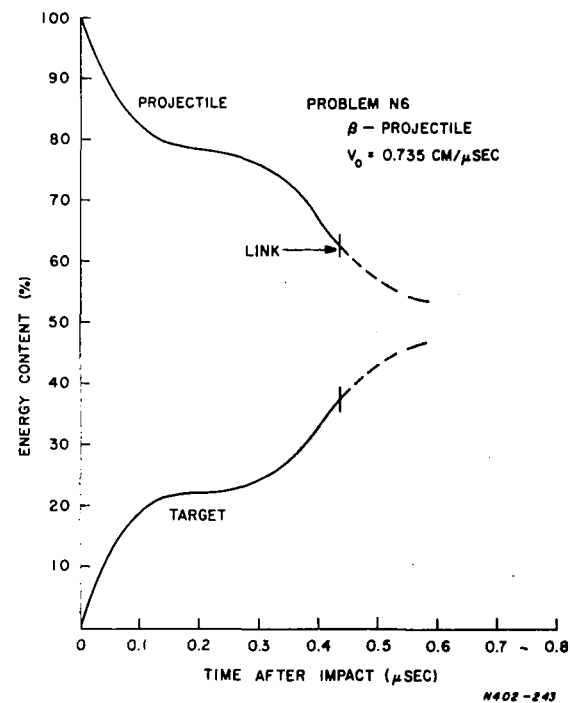
Figure 7 concluded. Problem N2
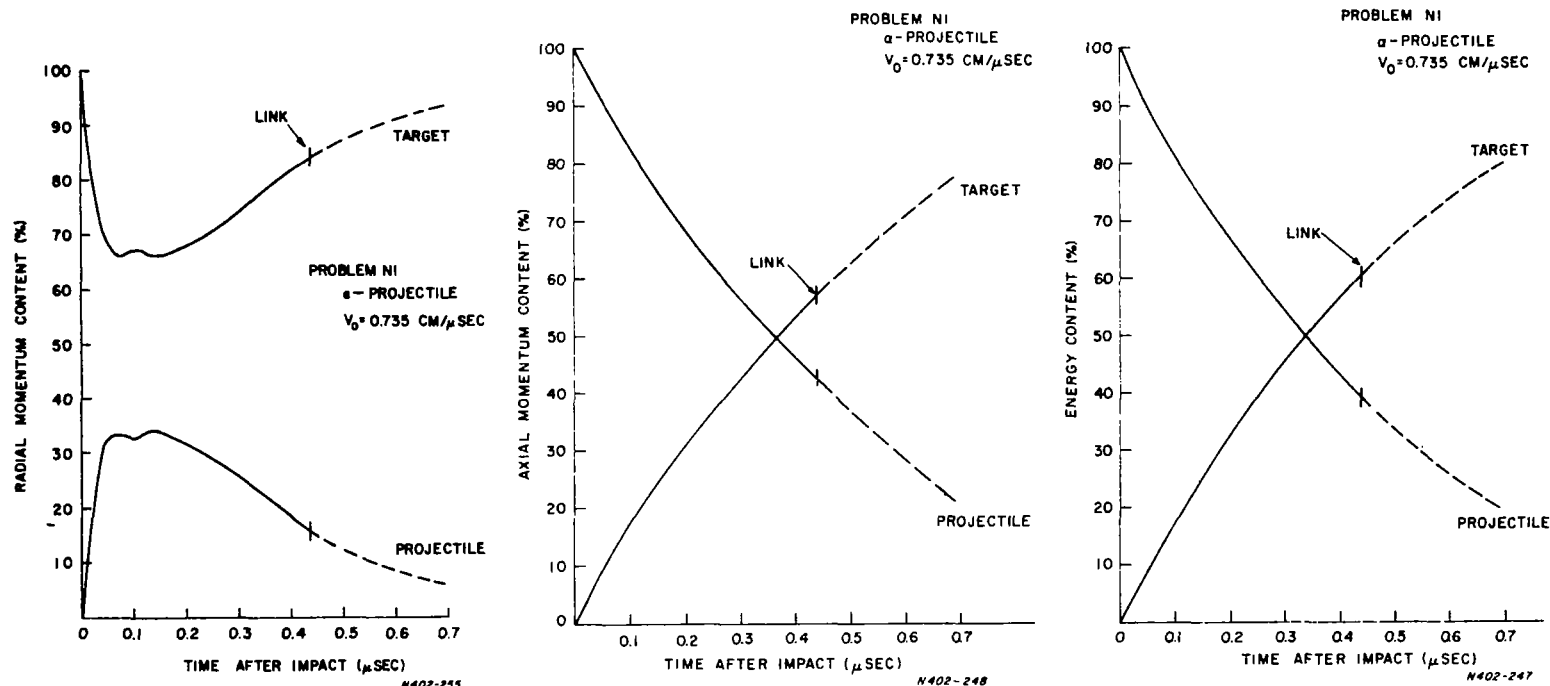
(a) Scalar radial momentum   (b) Axial momentum   (c) Total Energy

Figure 8. Normal-density projectile, problem N1: α - projectile impacting target at v_o = 0.735 cm/μsec.
Time variation of partition of momentum and energy content between projectile and target materials.

(a) Scalar radial momentum   (b) Axial momentum   (c) Total energy

Figure 9.   Normal-density projectile, problem N2: α-projectile impacting target at v_o = 2.0 cm/μsec.
Time variation of partition of momentum and energy content between projectile and target materials.
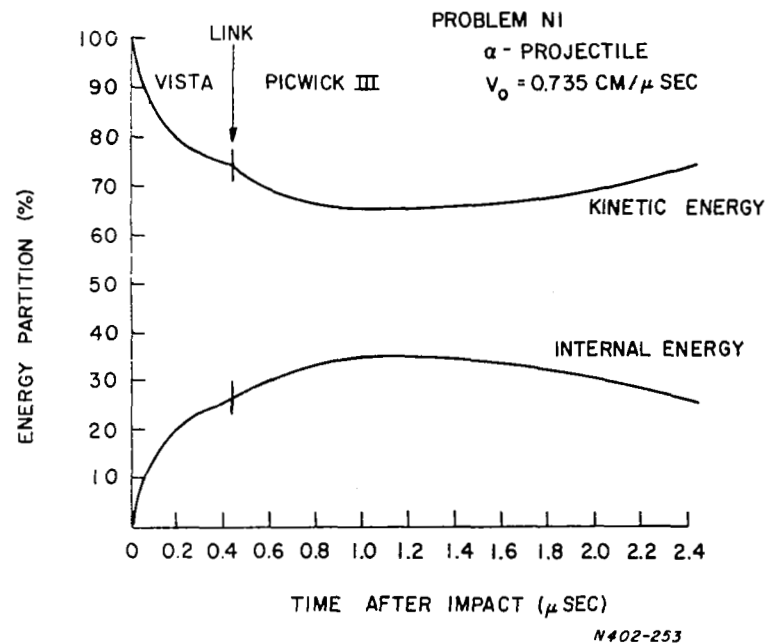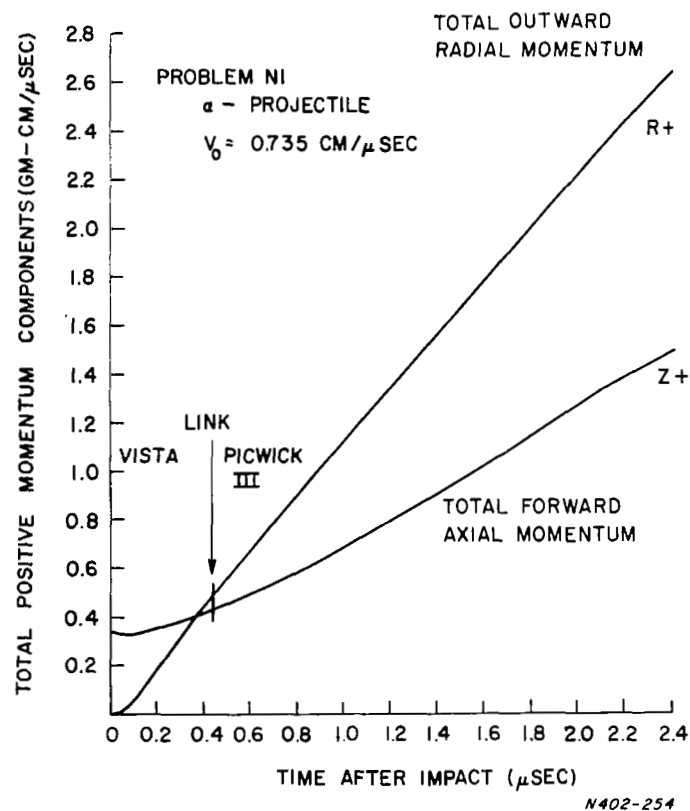
(a) Total positive momentum components   (b) Total energy division

Figure 10. Normal-density projectile, problem N1: α-projectile impacting target at v_o = 0.735 cm/μ sec. Continuity of gross features of the flow field through the LINK process is shown.

N402-239
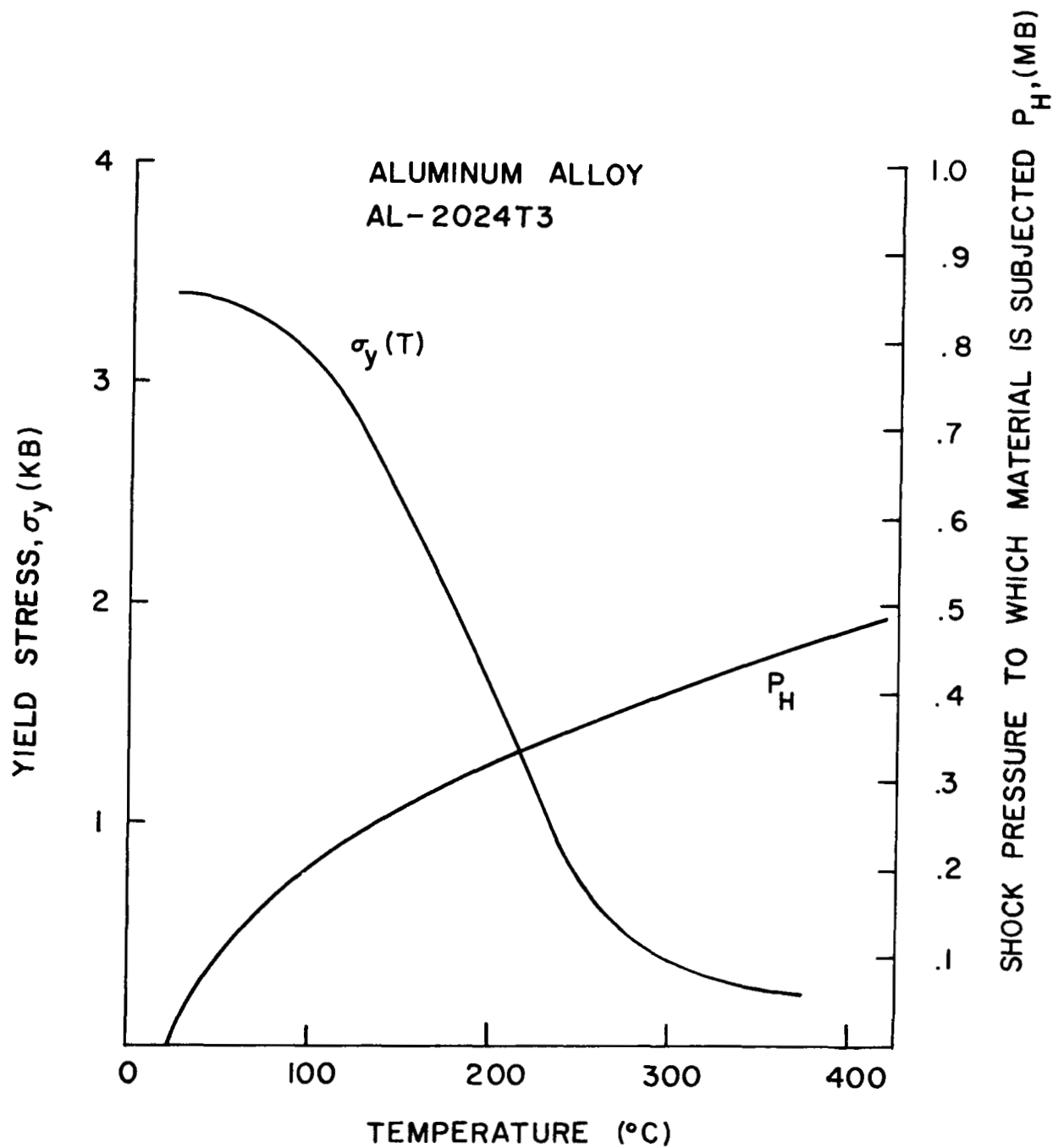
Figure 11. Dependence of yield stress of aluminum alloy Al-2024 on temperature, and the residual temperature of shock-processed aluminum.
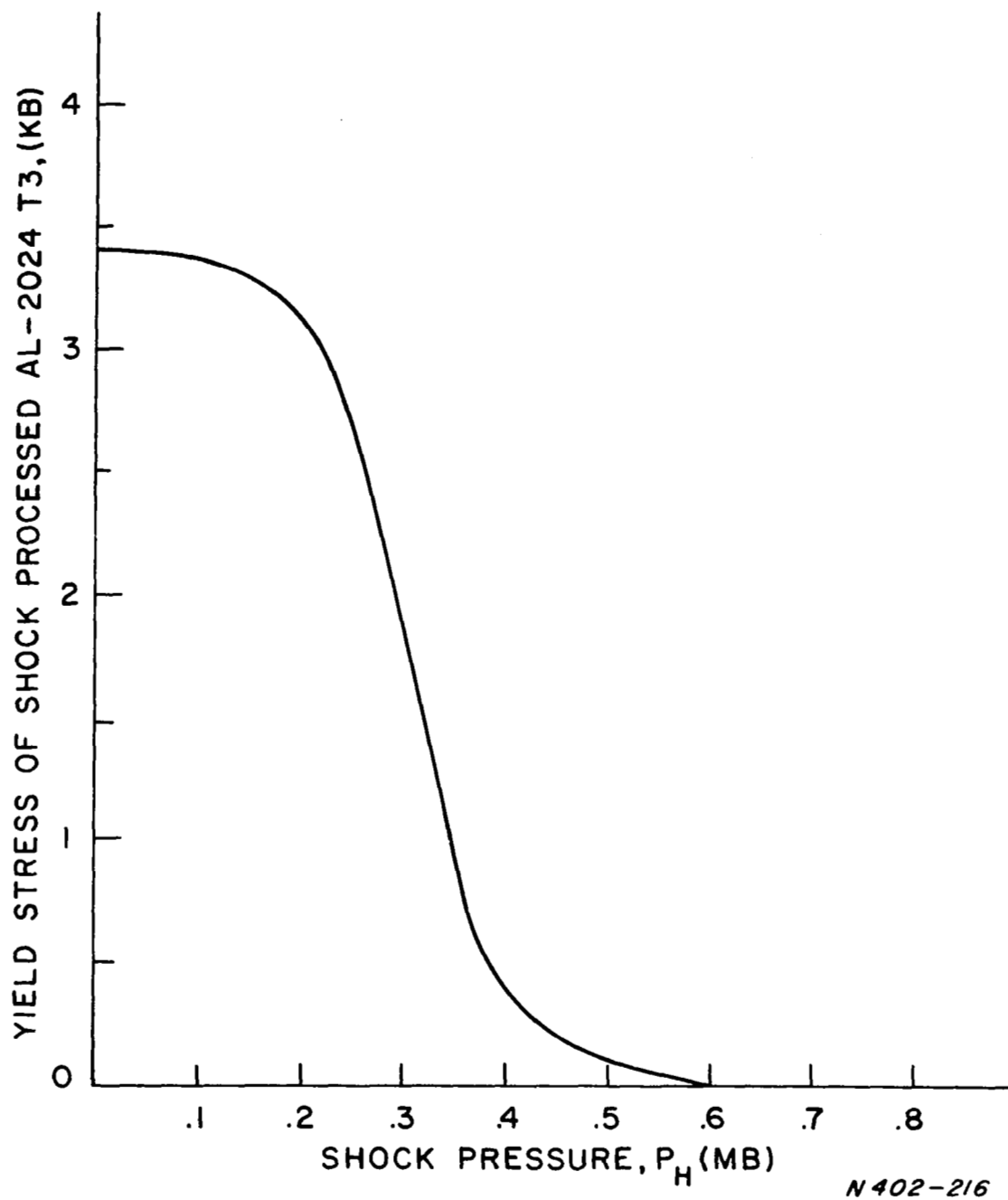
Figure 12. Yield stress of aluminum alloy Al-2024 subsequent to the passage of a shock wave.

PROBLEM NI
α – PROJECTILE
V_0 = .735 CM/μSEC

ℓ = .27736

DEPTH INTO TARGET, Z/ℓ

P_{DYN} = 3.4 KB

TIME, μSEC
····· 1.62
—— 2.30

DEPTH INTO TARGET AT AXIS OF SYMMETRY, Z/ℓ

3.4 KB

YIELD STRESS, σ_Y (T), IN WAKE OF SHOCK

N 402-256

PEAK AXIAL PRESSURE (MB), P_{max}

.2   .4   .6   .8   1.0   1.2   1.4

PROBLEM NI
α – PROJECTILE
V_0 = 0.735 CM/μSEC

DEPTH INTO TARGET, Z/ℓ

o   VISTA CALCULATIONS
σ   PICWICK Ⅲ CALCULATIONS
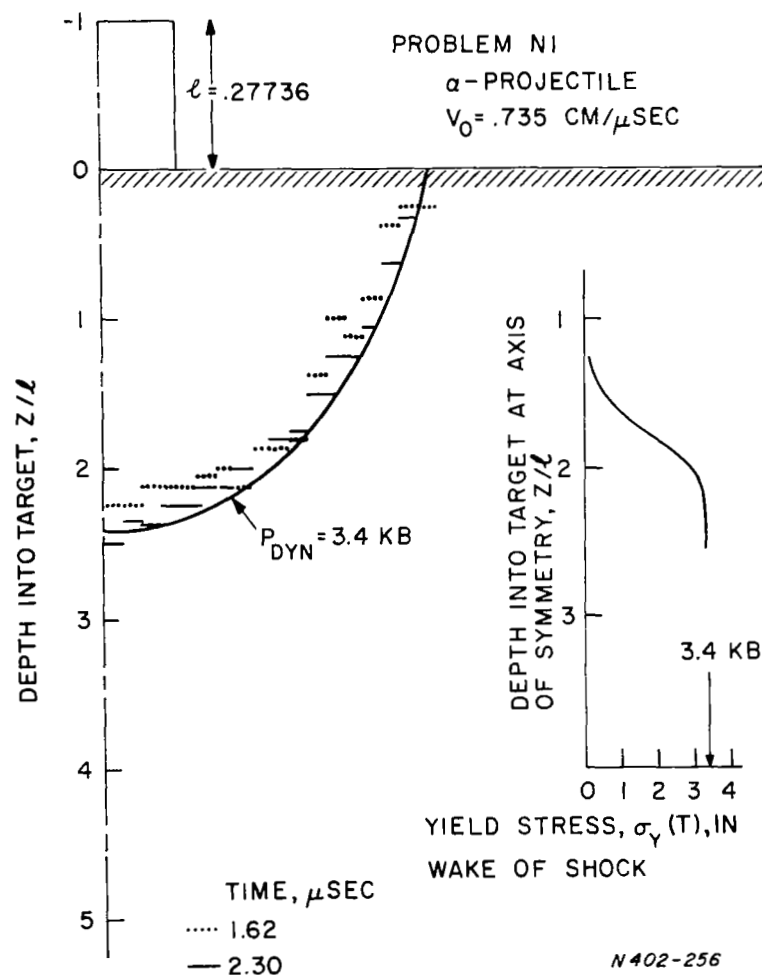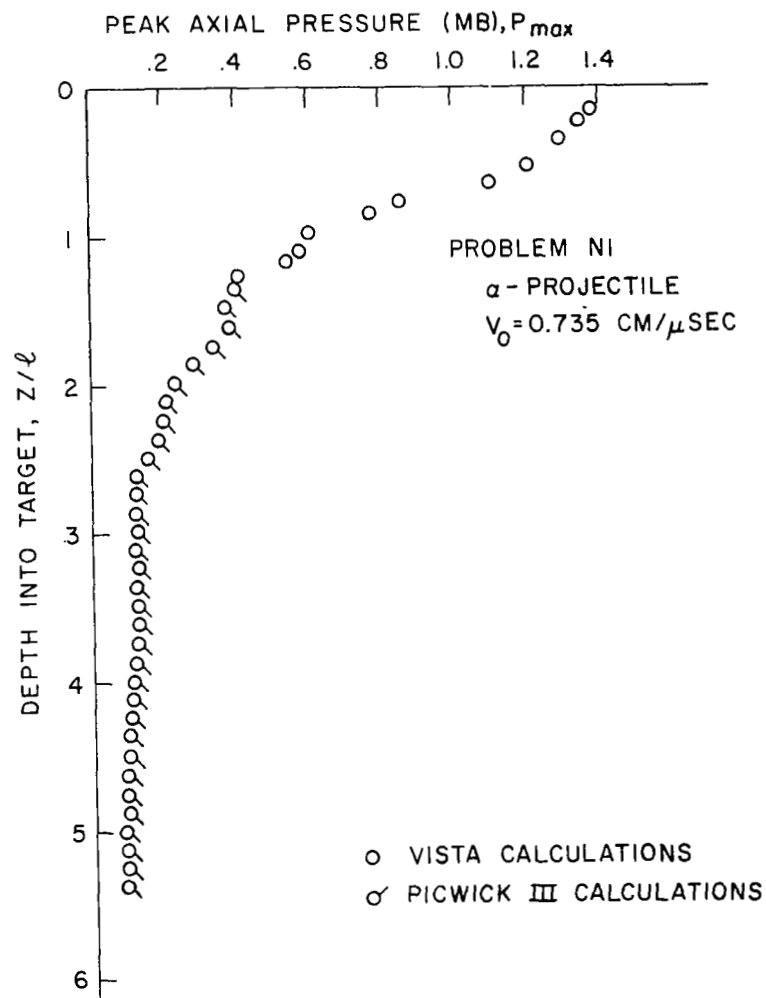
N402-257
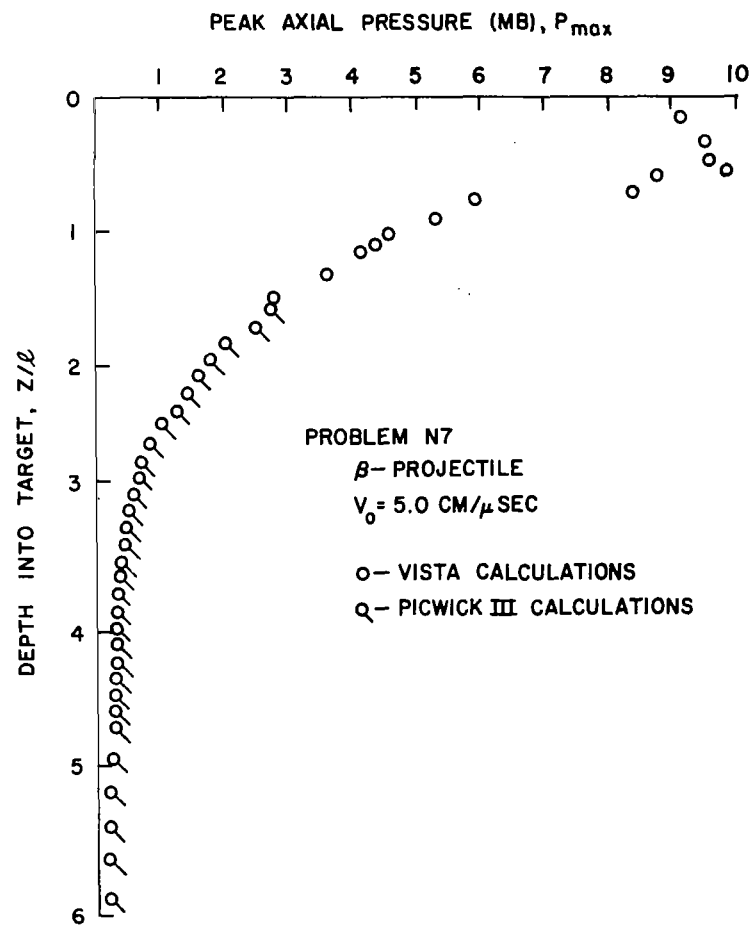
(a) Predicted crater

(b) Peak axial pressure along axis

Figure 13.   Normal-density projectile, problem N1: α-projectile impacting target at v_0 = 0.735 cm/μsec. Crater prediction based on dynamic pressure criterion.
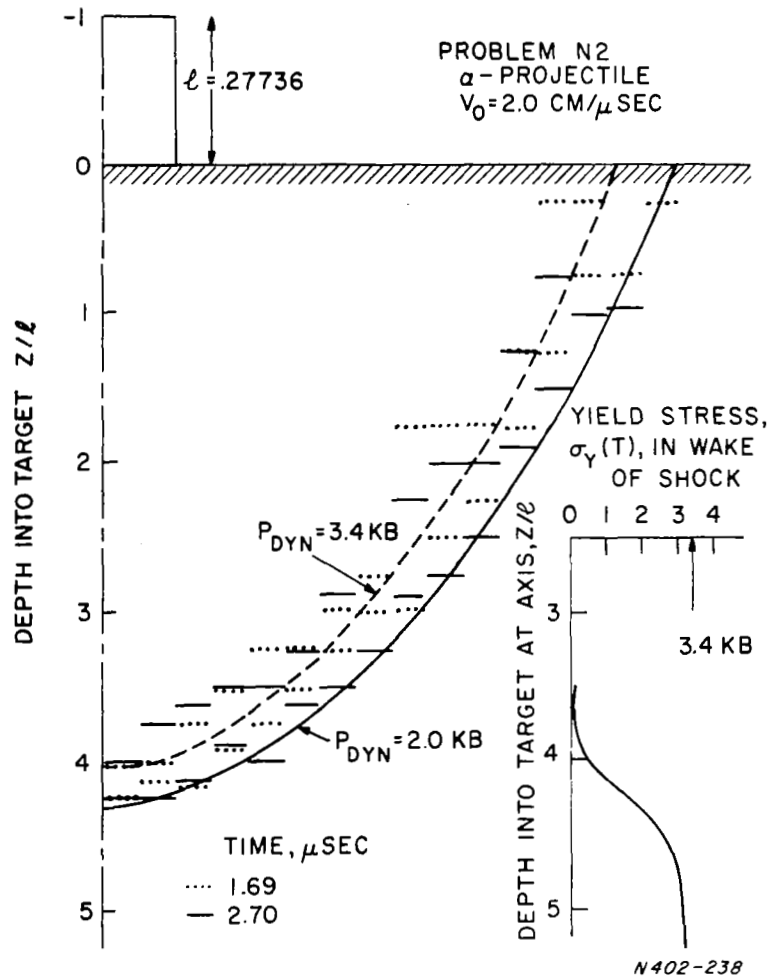
(a) Predicted crater
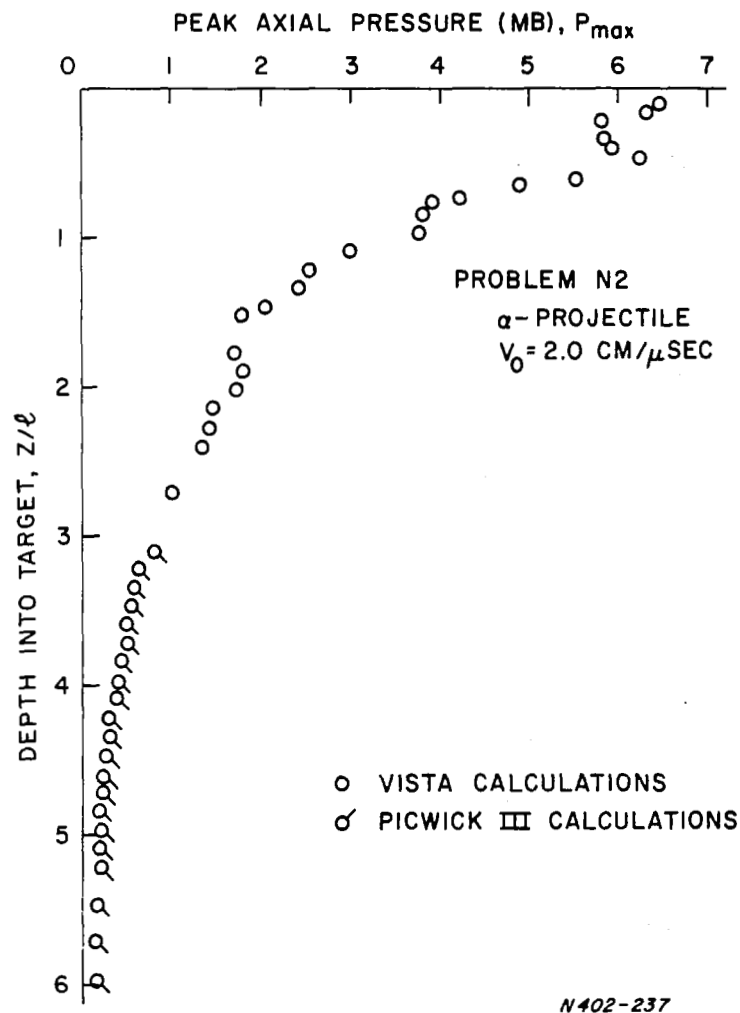
(b) Peak axial pressure along axis

Figure 14. Normal-density projectile, problem N2: α-projectile impacting target at $v_o = 2.0$ cm/μsec. Crater prediction based on dynamic pressure criterion.
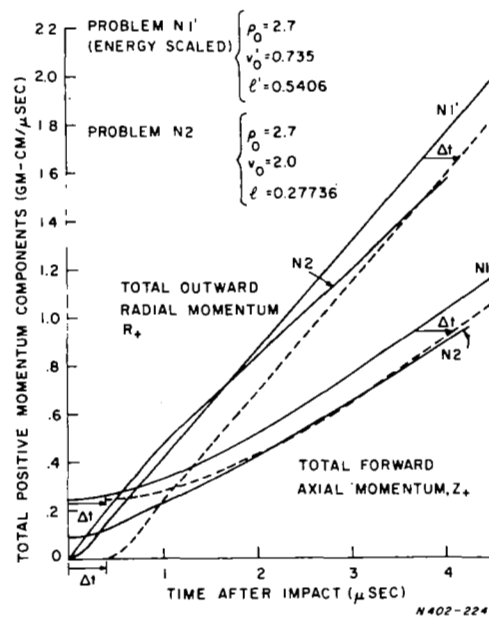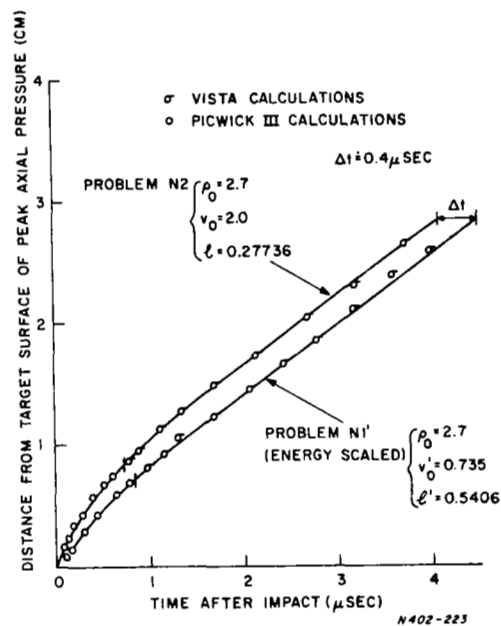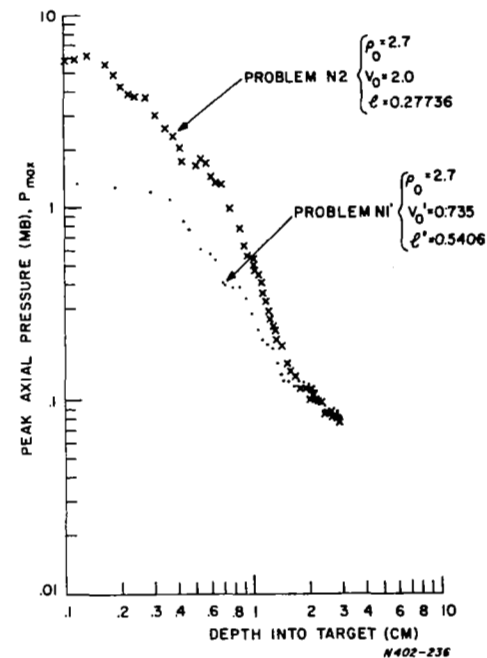
(a) Total positive momentum   (b) Time correction   (c) Axial pressure amplitude

Figure 15. Normal-density projectiles. Test of late-stage equivalence of problem N1 when scaled for comparison with problem N2 on equal energy basis.
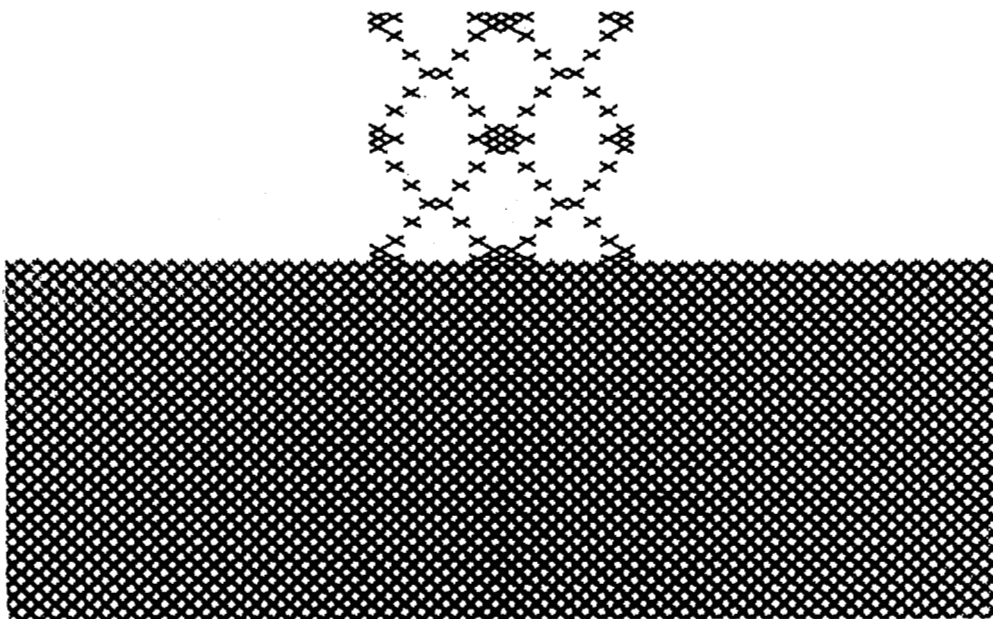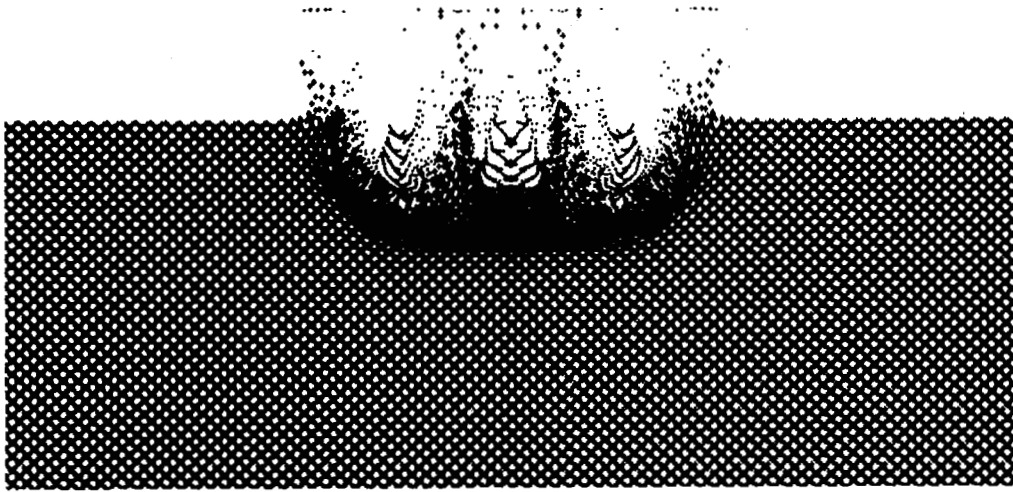
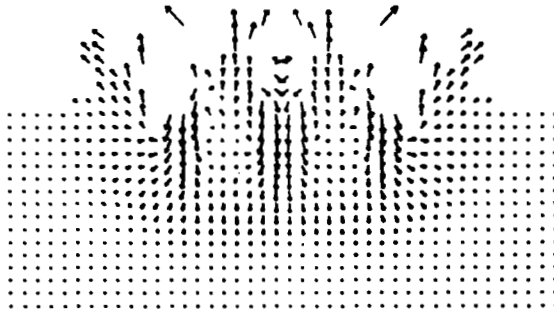(a) Projectile-target configuration, t = 0.004 μ sec (VISTA)
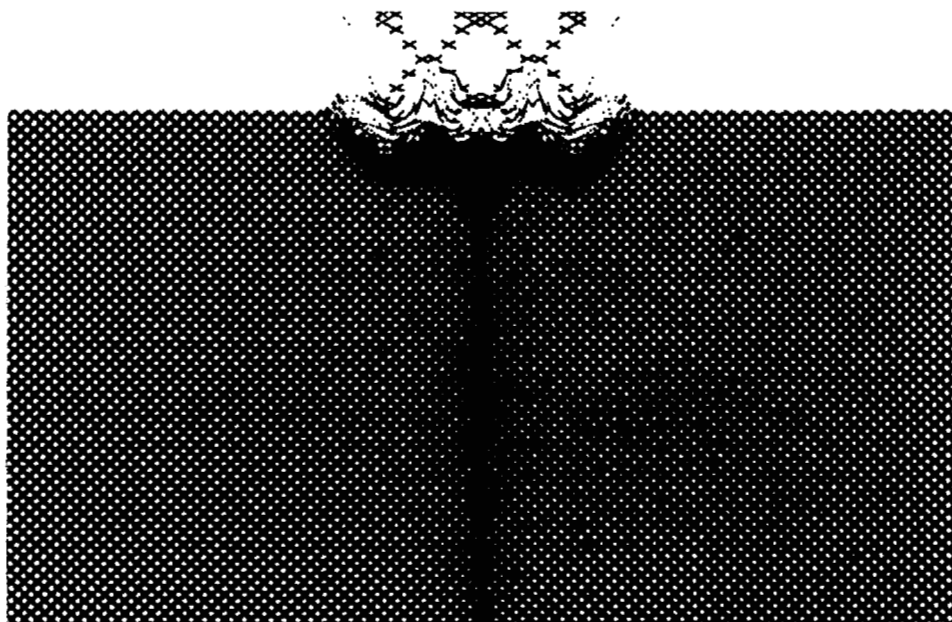
(b) Projectile-target configuration, t = 0.122 μ sec (VIST

Figure 16. Heterogeneous reduced-density projectile, problem N3: β-pro-
jectile impacting target at v_o = 2.0 cm/μ sec. Graphical displays of
projectile-target configuration, velocity field and mass flux
at indicated times.
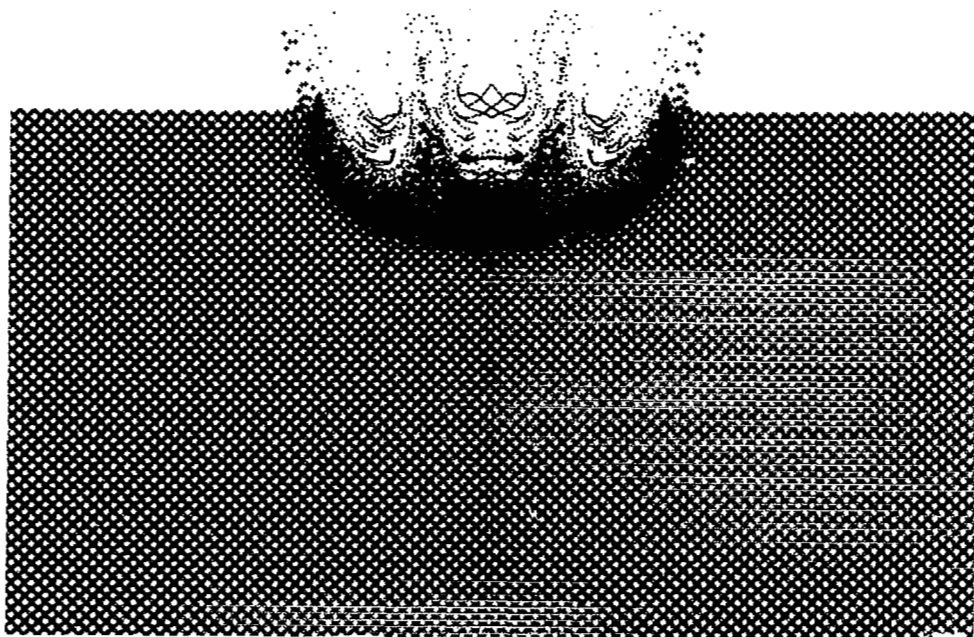
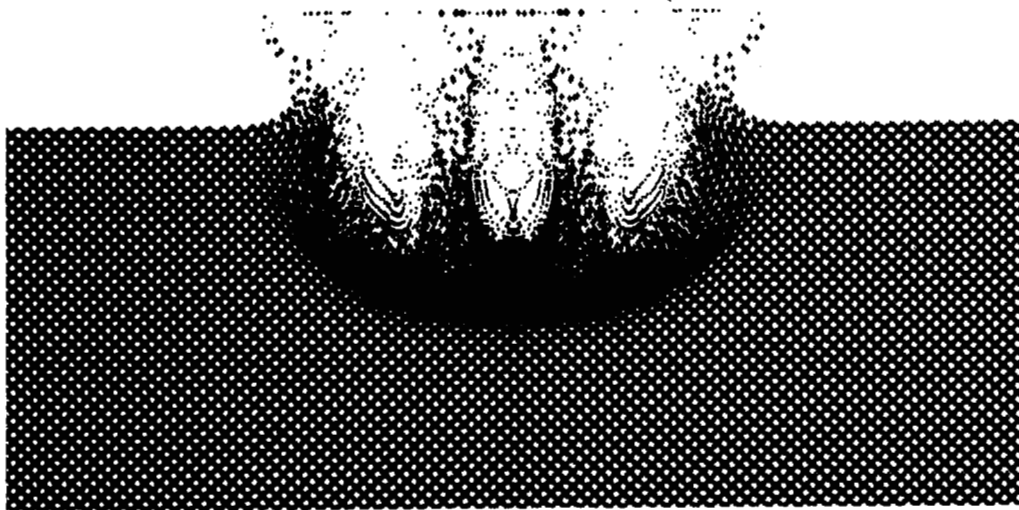(c) Projectile-target configuration, t = 0.273 sec (VISTA)
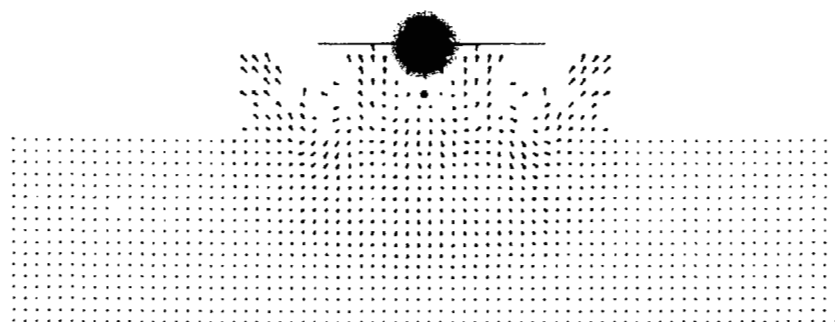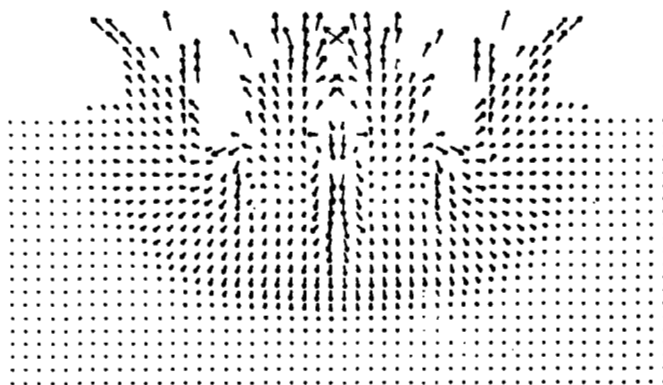

(d) Velocity field, t = 0.278 μ sec (VISTA)

Figure 16 continued. Problem N3.
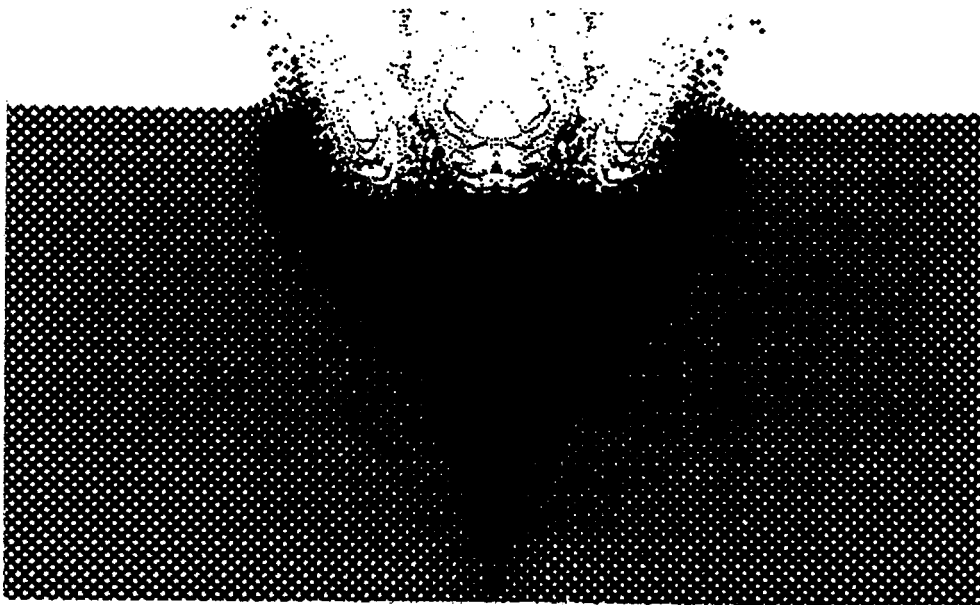
(e) Projectile-target configuration, t = 0.394 μ sec (VISTA)
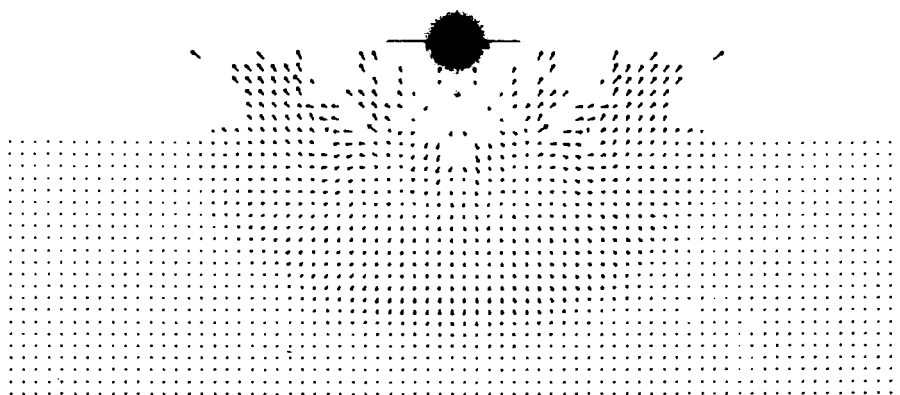
(f) Velocity field, t = 0.412 μ sec (VISTA)

Figure 16 continued. Problem N3.
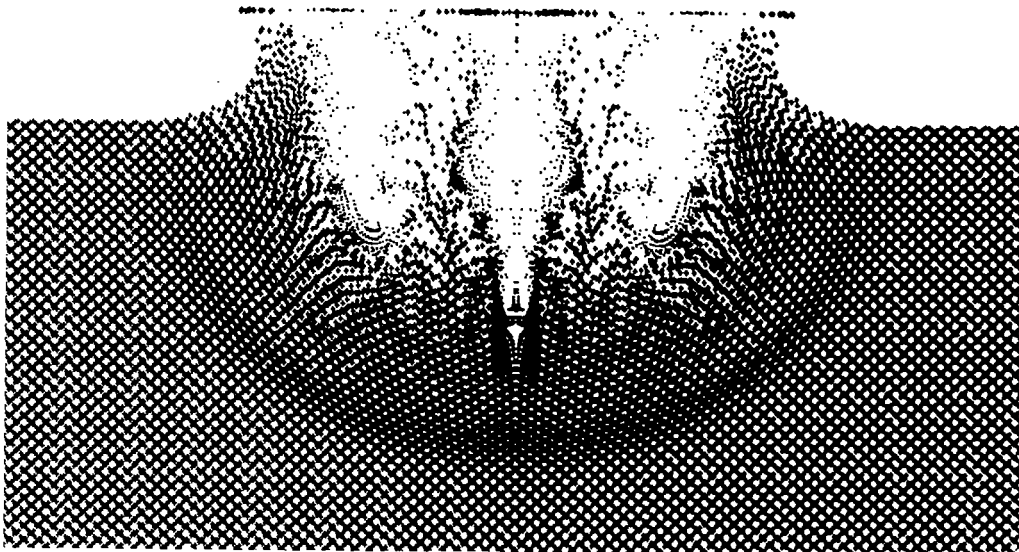
(g) Projectile-target configuration, t = 0.662 μ sec (VISTA)
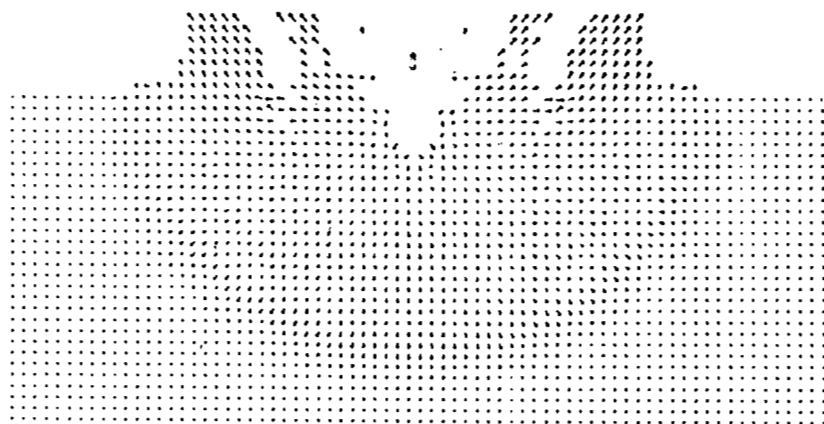
(h) Velocity field, t = 0.703 μ sec (VISTA)

Figure 16 continued. Problem N3.

72
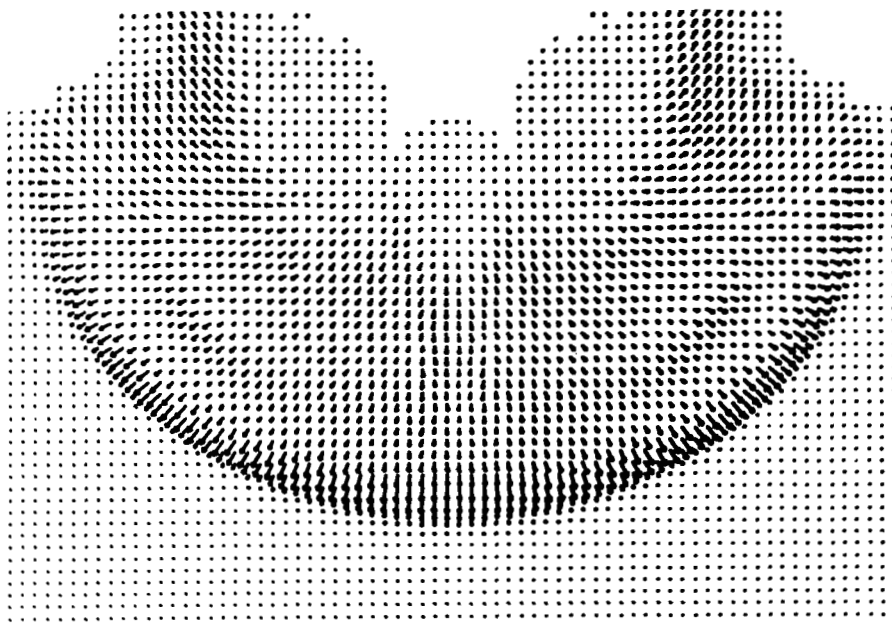
(i) Mass flux field, t = 1.121 μ sec (PICWICK III)
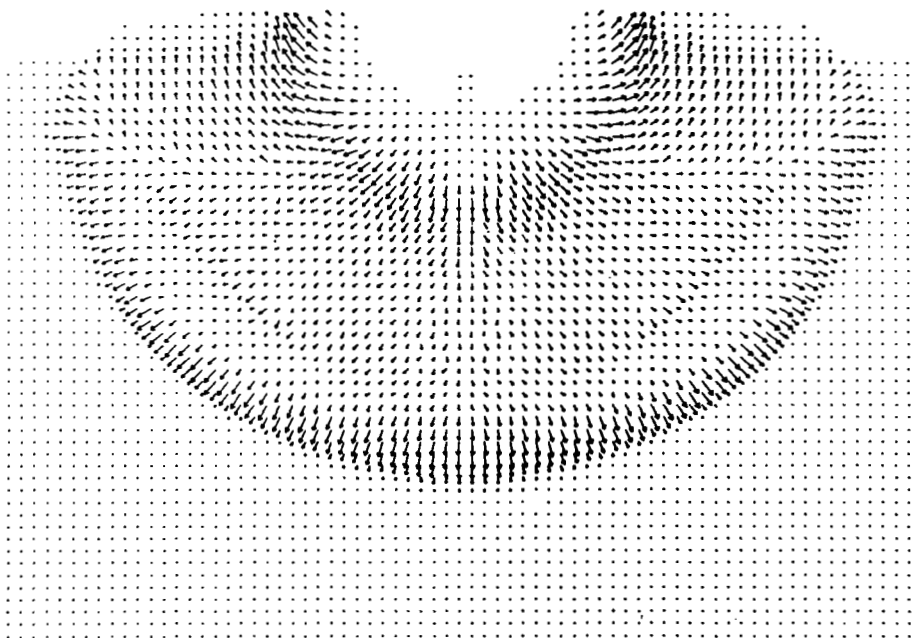
(j) Mass flux field, t = 2.719 μ sec (PICWICK III)

Figure 16 concluded.   Problem N3.
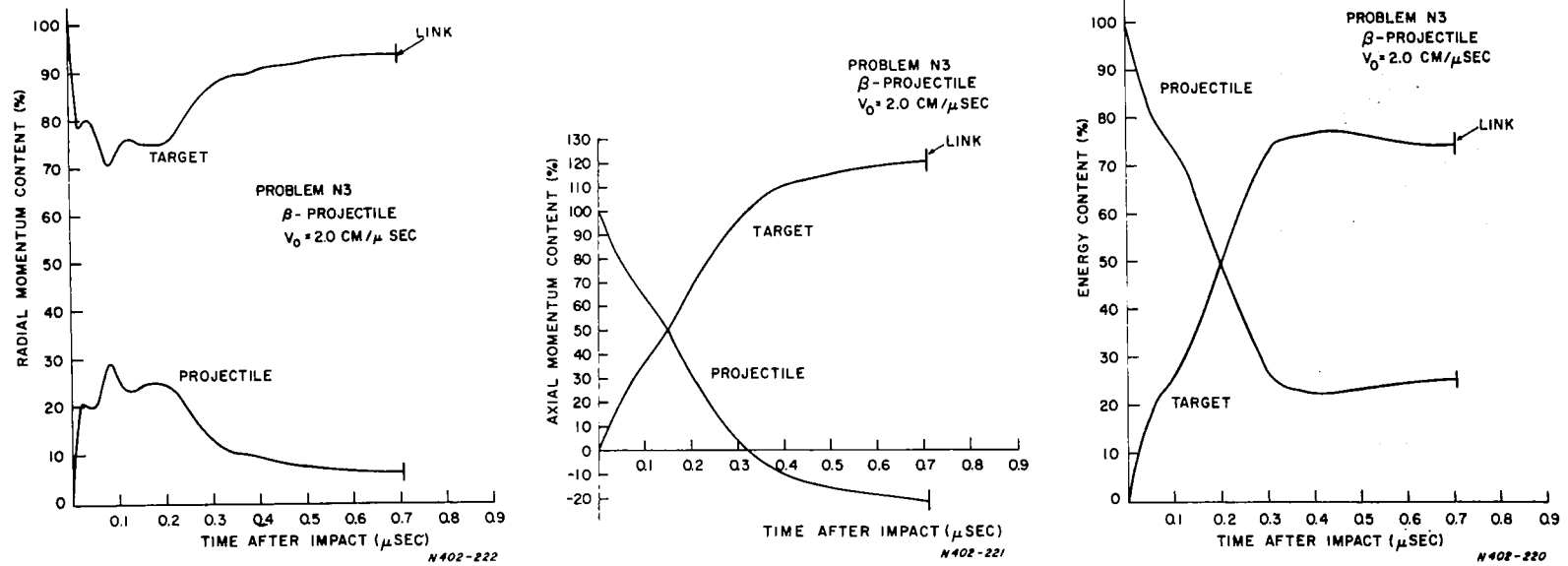
(a) Scalar radial momentum   (b) Axial momentum   (c) Total energy

Figure 17. Heterogeneous low-density projectile, problem N3: β-projectile impacting target at $v_o = 2.0$ cm/μsec. Time variation of partition of momentum and energy content between projectile and target materials
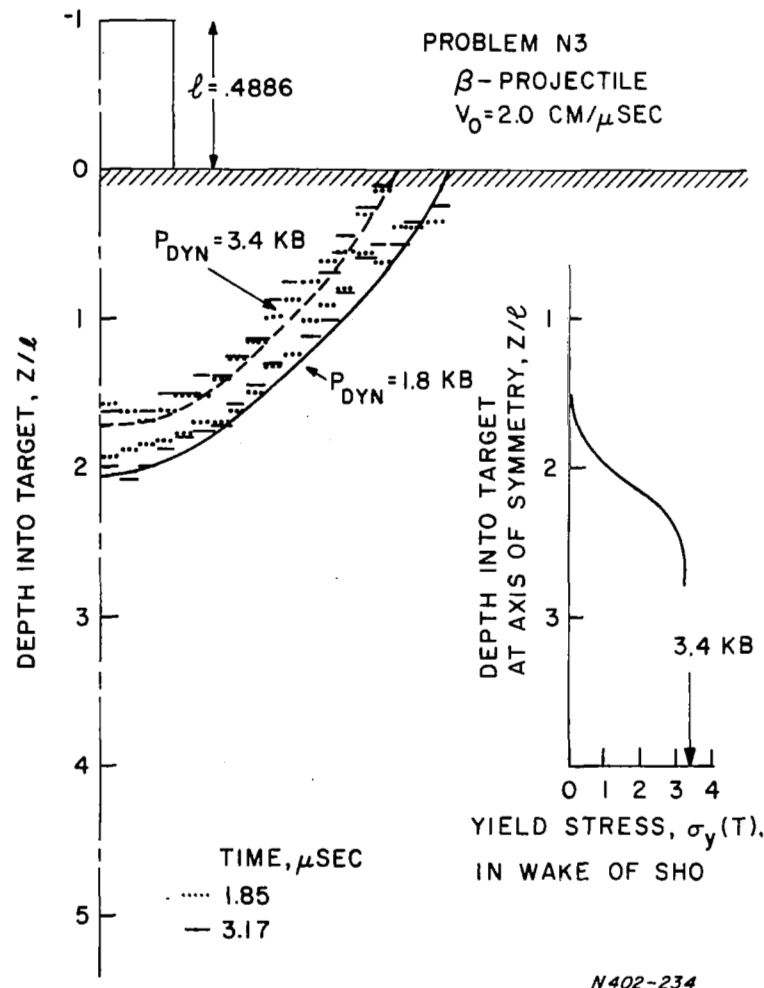
(a) Predicted crater
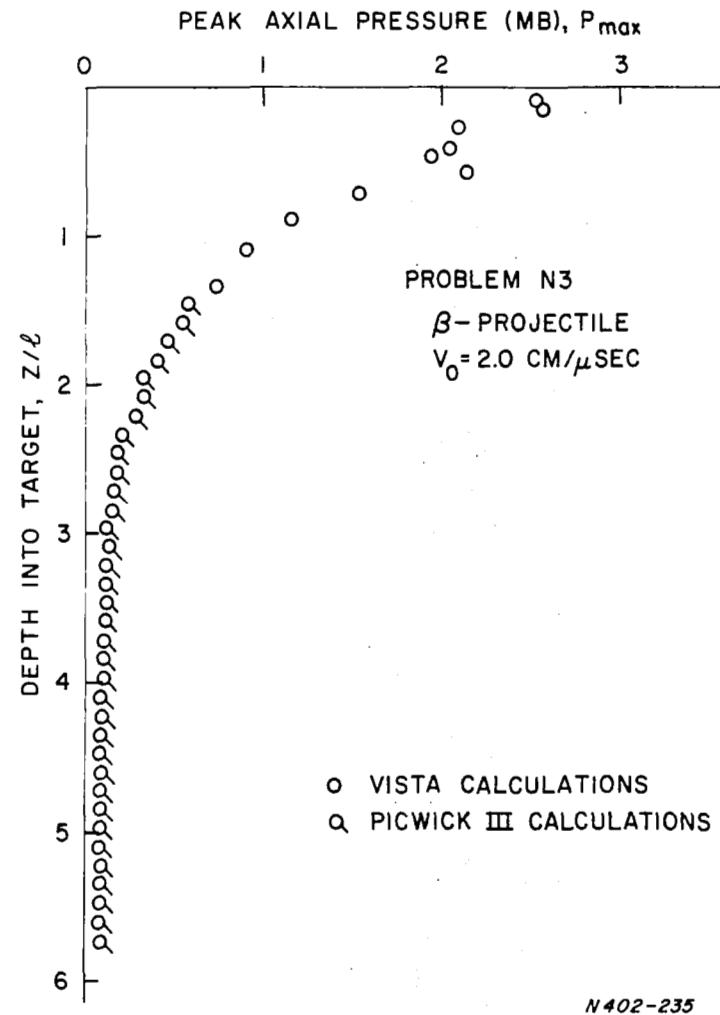
(b) Peak axial pressure along axis

Figure 18. Heterogeneous low-density projectile, problem N3: β-projectile impacting target at $v_o = 2.0$ cm/μsec. Crater prediction based on dynamic pressure criterion.
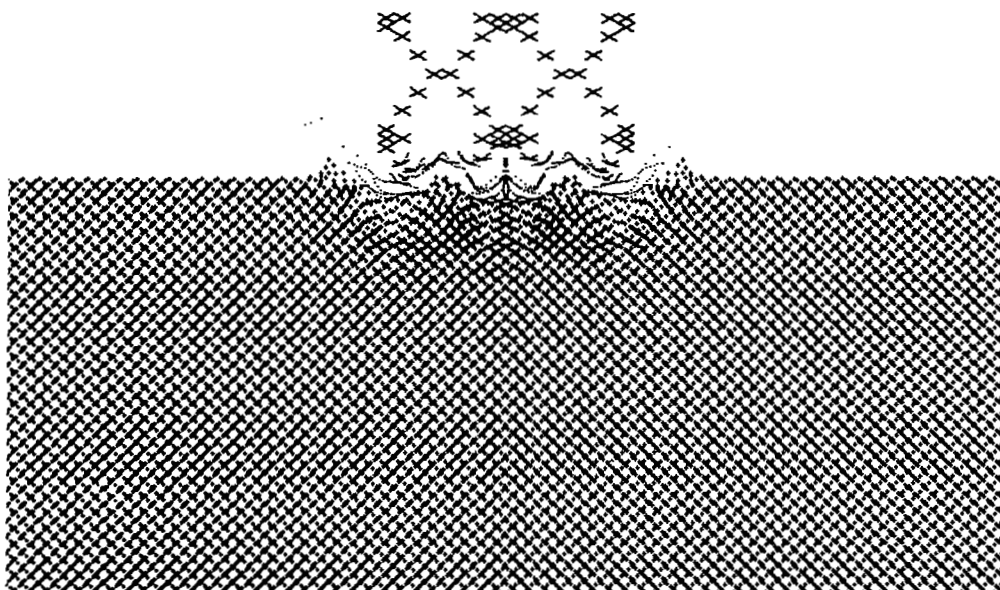
(a) Projectile-target configuration, $t = 0.227\ \mu\mathrm{sec}$ (VISTA)
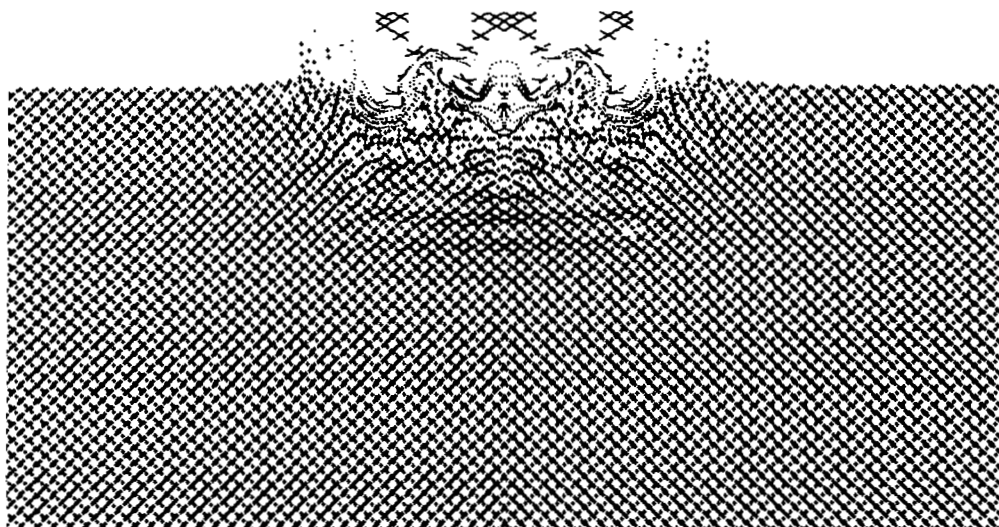
(b) Projectile-target configuration, $t = 0.465\ \mu\mathrm{sec}$ (VISTA)

Figure 19. Heterogeneous reduced-density projectile, problem N6: β-projectile impacting target at $v_{o} = 0.735\ \mathrm{cm}/\mu\mathrm{sec}$. Graphical displays of projectile-target configuration and mass flux field at indicated times.

76
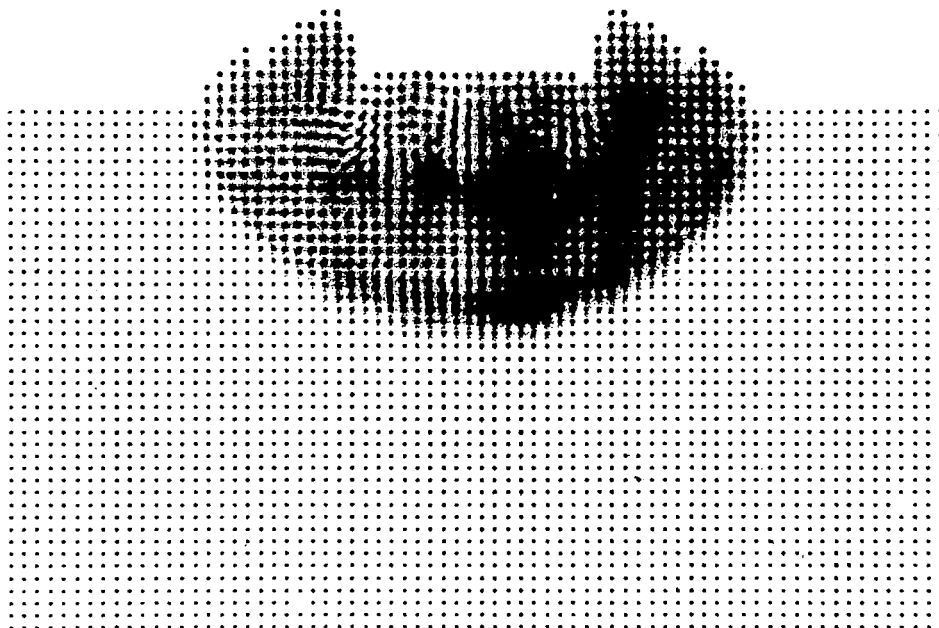
(c) Mass flux field, t = 0.674 μsec (PICWICK III)
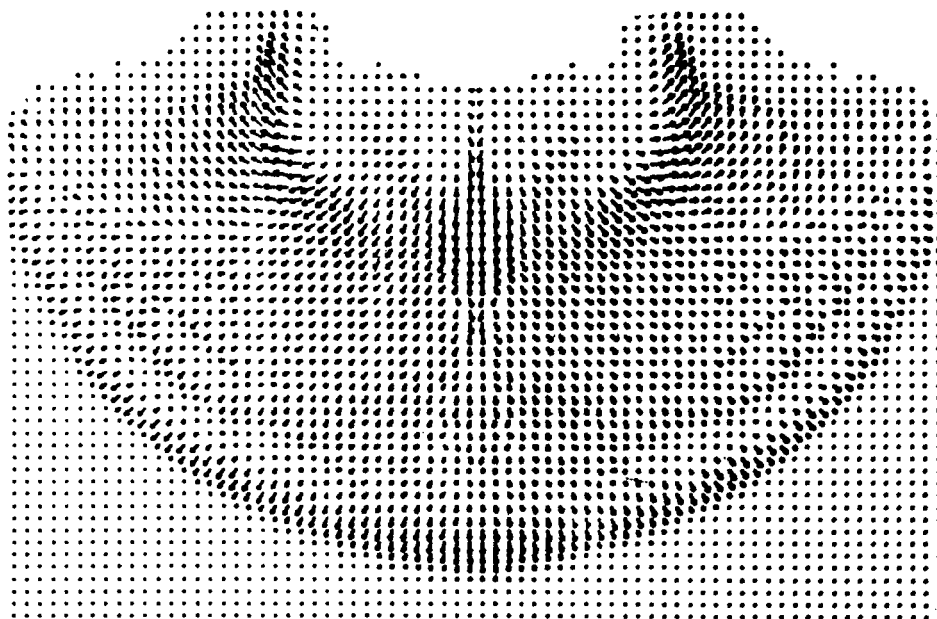
(d) Mass flux field, t = 1.703 μsec (PICWICK III)

Figure 19 concluded. Problem N6

(a) Projectile-target configuration, t = 0.054 μsec (VISTA)
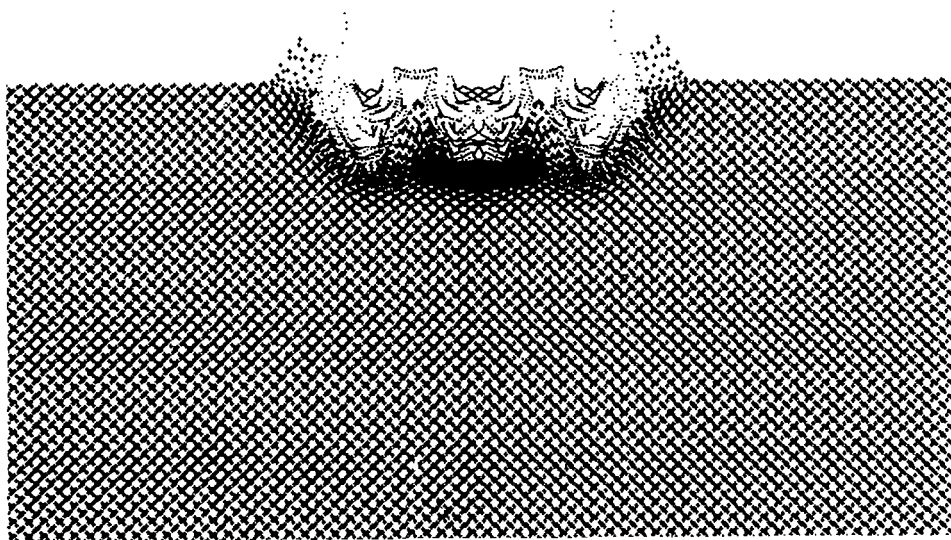
(b) Projectile-target configuration, t = 0.100 μsec (VISTA)

Figure 20. Heterogeneous reduced-density projectile, problem N7: β-projectile impacting target at v_o = 5.0 cm/μsec. Graphical displays of projectile-target configuration, velocity field, and mass flux field at indicated times.

(c) Projectile-target configuration, t = 0.176 μsec (VISTA)

(d) Velocity field, t = 0.176 μsec (VISTA)

Figure 20 continued. Problem N7

(e) Projectile target configuration, t = 0.411 μ sec (VISTA)

(f) Velocity field, t = 0.411 μsec (VISTA)

Figure 20 continued. Problem N7

80
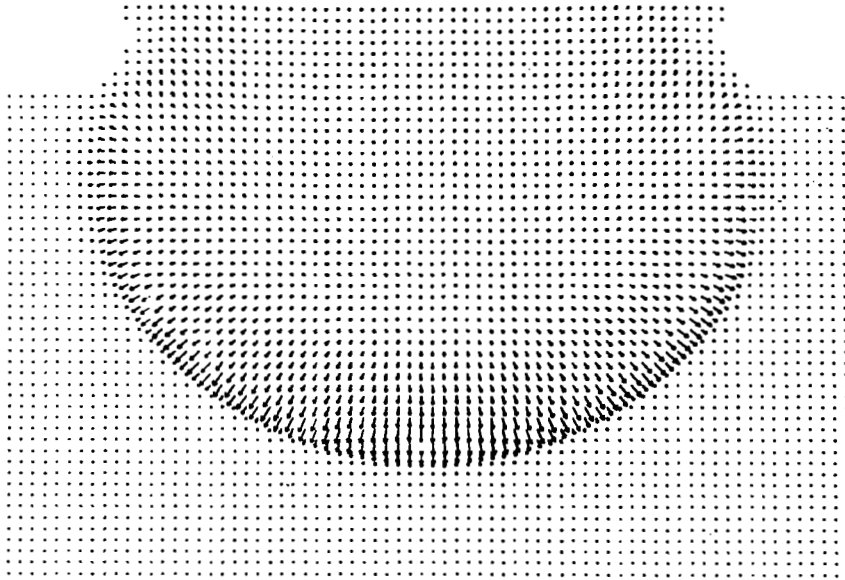
(g) Mass flux field, t = 0.580 μsec (PICWICK III)
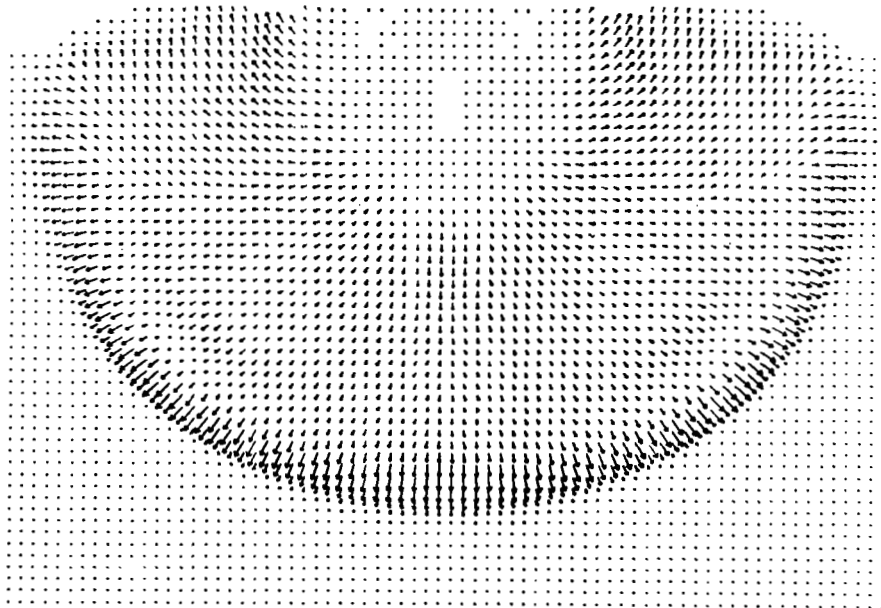
(h) Mass flux field, t = 2.266 μsec (PICWICK III)

Figure 20 concluded.   Problem N7
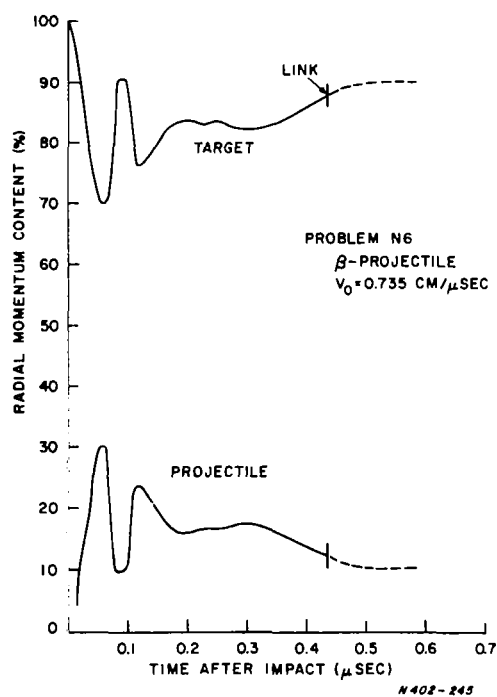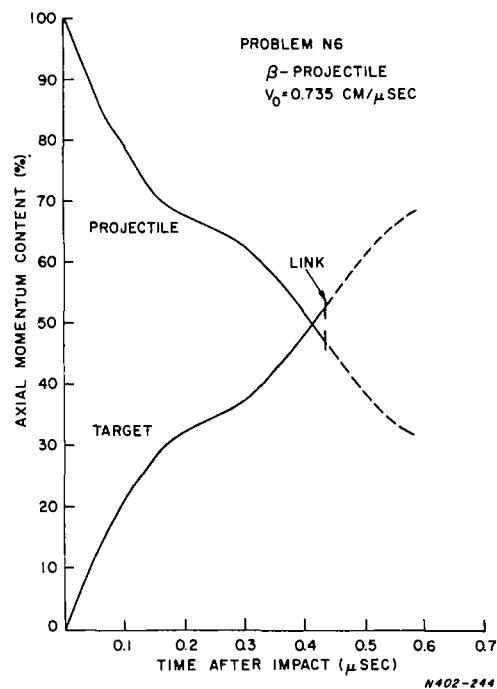
(a) Scalar radial momentum   (b) Axial momentum   (c) Total energy

Figure 21. Heterogeneous reduced-density projectile, problem N6: β-projectile impacting target at $v_o = 0.735$ cm/μsec. Time variation of partition of momentum and energy content between projectile and target materials.
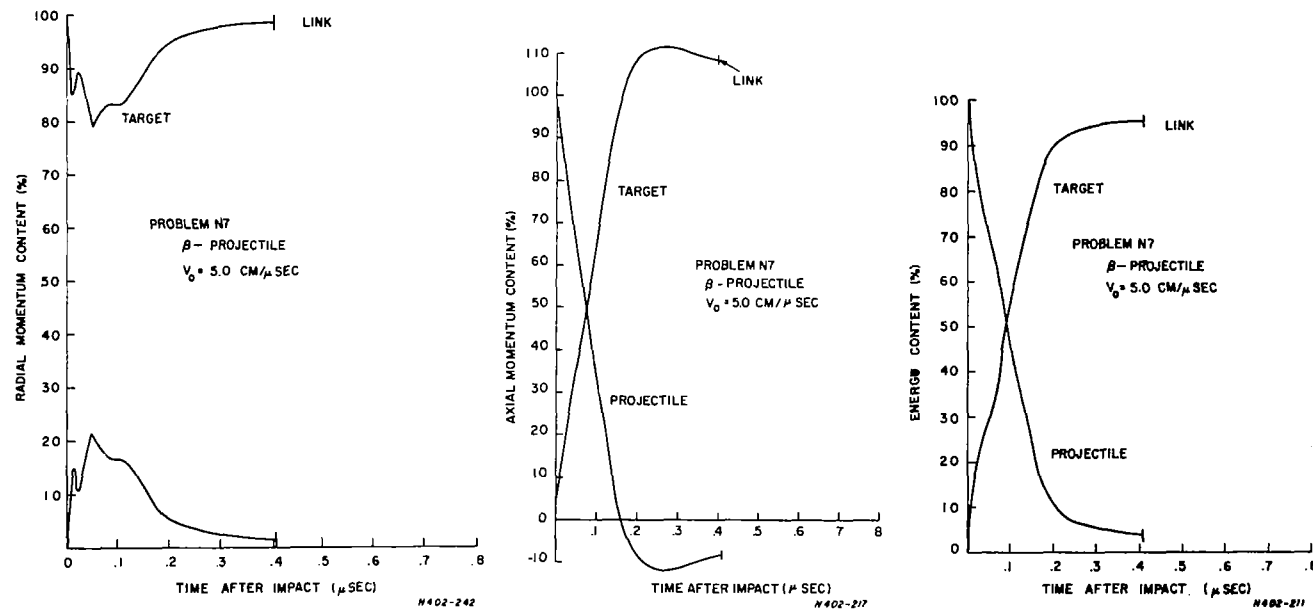
(a) Scalar radial momentum   (b) Axial momentum   (c) Total energy

Figure 22. Heterogeneous reduced-density projectile, problem N7: β-projectile impacting target at v_o = 5.0 cm/μsec. Time variation of partition of momentum and energy content between projectile and target materials.
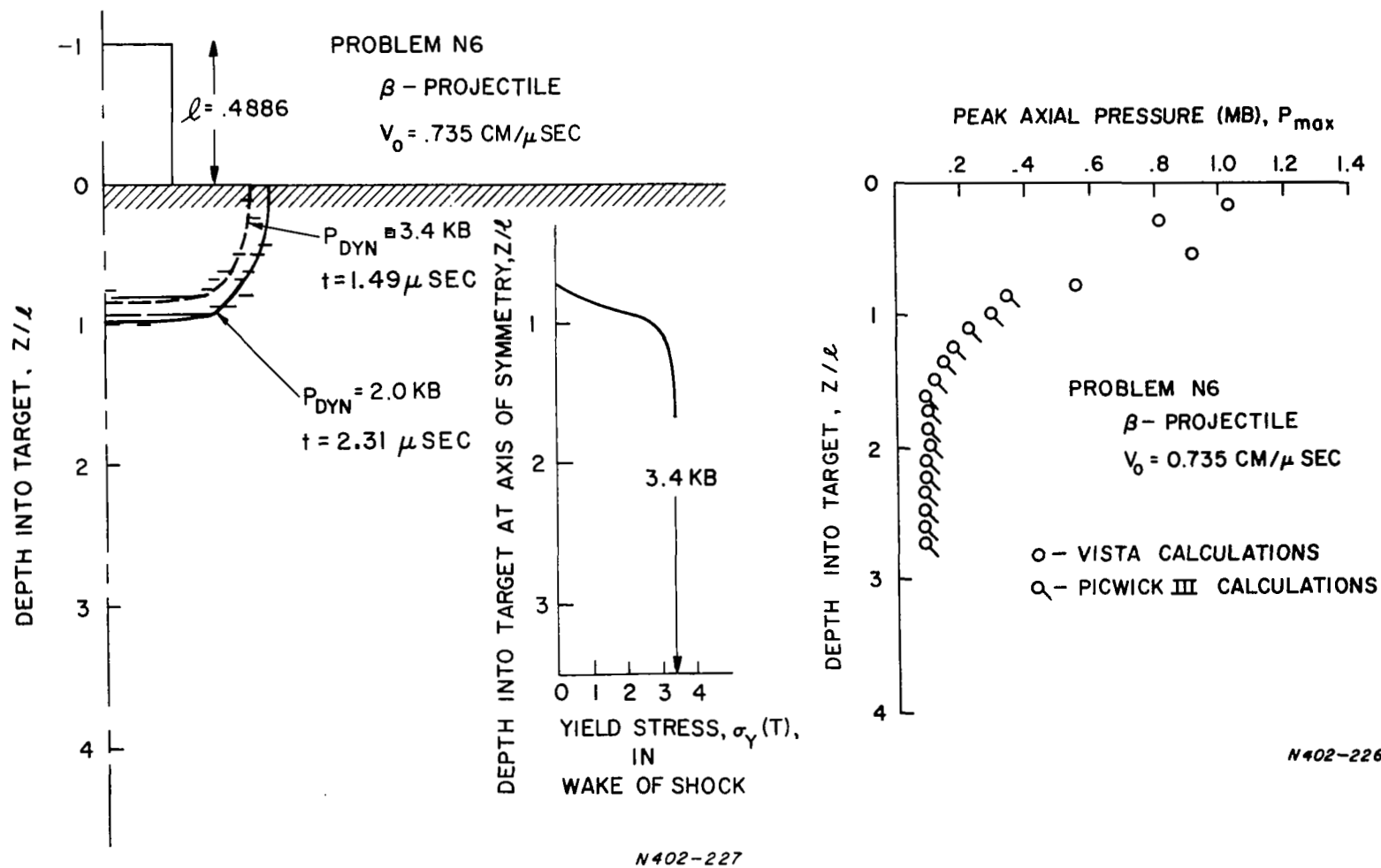
(a) Predicted crater

(b) Peak axial pressure along axis

Figure 23. Heterogeneous reduced-density projectile, problem N6: β-projectile impacting target at $v_o = 0.735$ cm/μsec. Crater prediction based on dynamic pressure criterion.
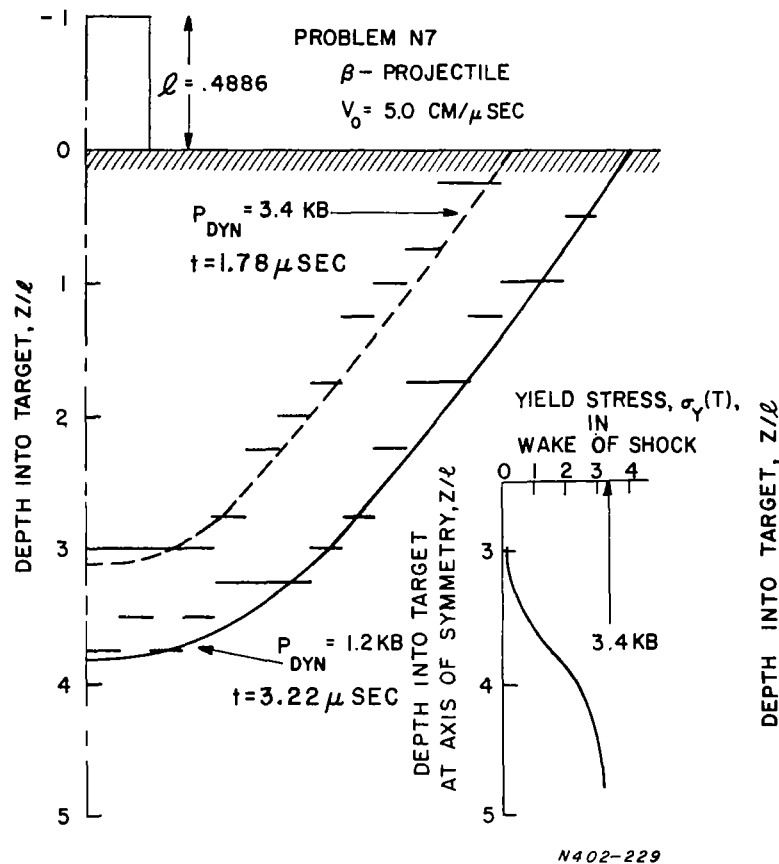
(a) Predicted crater

(b) Peak axial pressure along axis *N402-228*

Figure 24. Heterogeneous reduced-density projectile, problem N7: β-projectile impacting target at $v_0 = 5.0$ cm/μsec. Crater prediction based on dynamic pressure criterion.
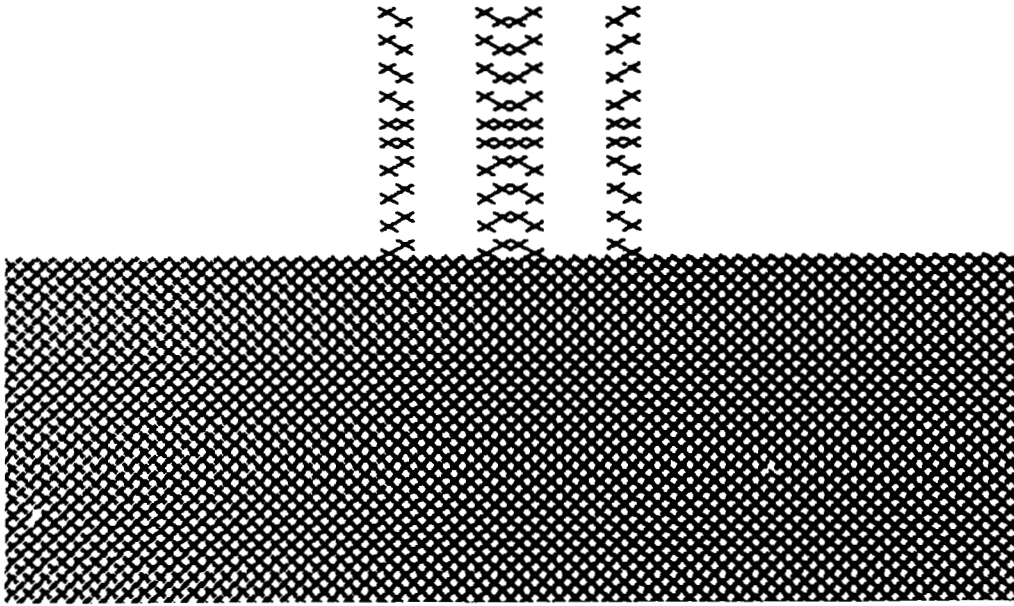
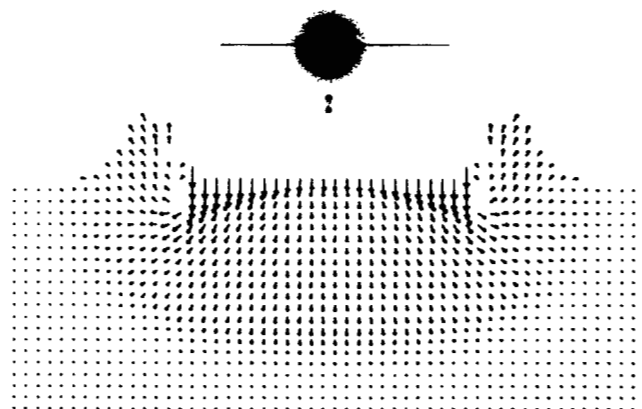(a) Projectile-target configuration, t = 0.002 μsec (VISTA)
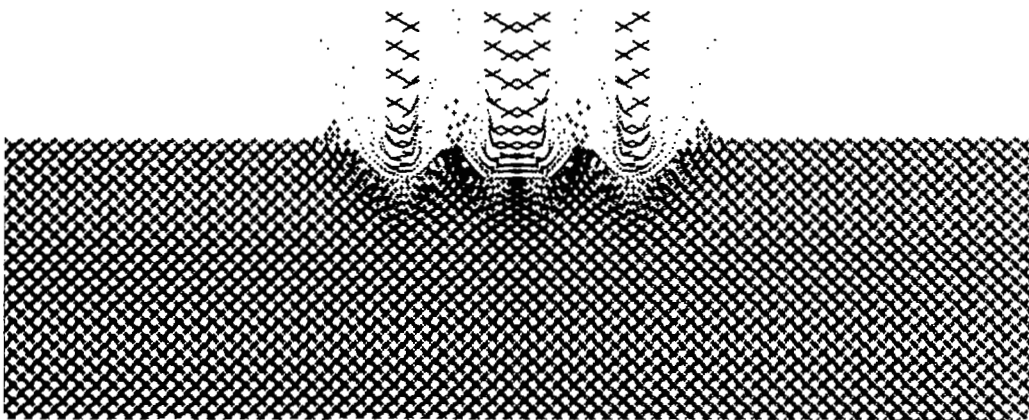
(b) Projectile-target configuration, t = 0.122 μsec (VISTA)

Figure 25. Heterogeneous reduced-density projectile, problem N4: γ - projectile impacting target at v_o = 2.0 cm/μsec. Graphical displays of projectile-target configuration, velocity field, and mass flux at indicated times.
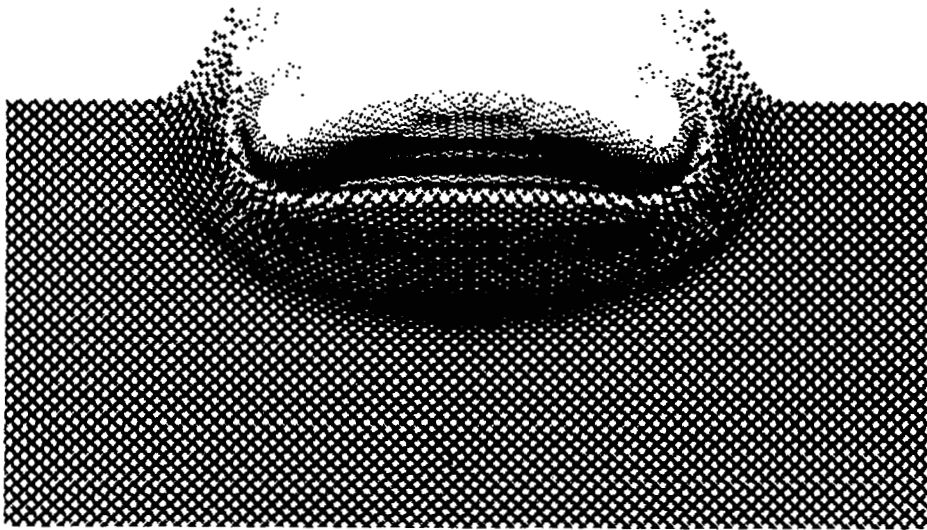
(c) Projectile-target configuration, t = 0.265 μ sec (VISTA)

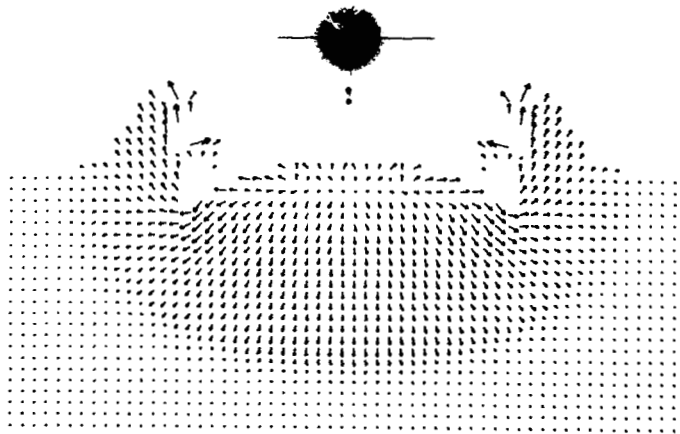(d) Velocity field, t = 0.265 μ sec (VISTA)

Figure 25 continued.   Problem N4.
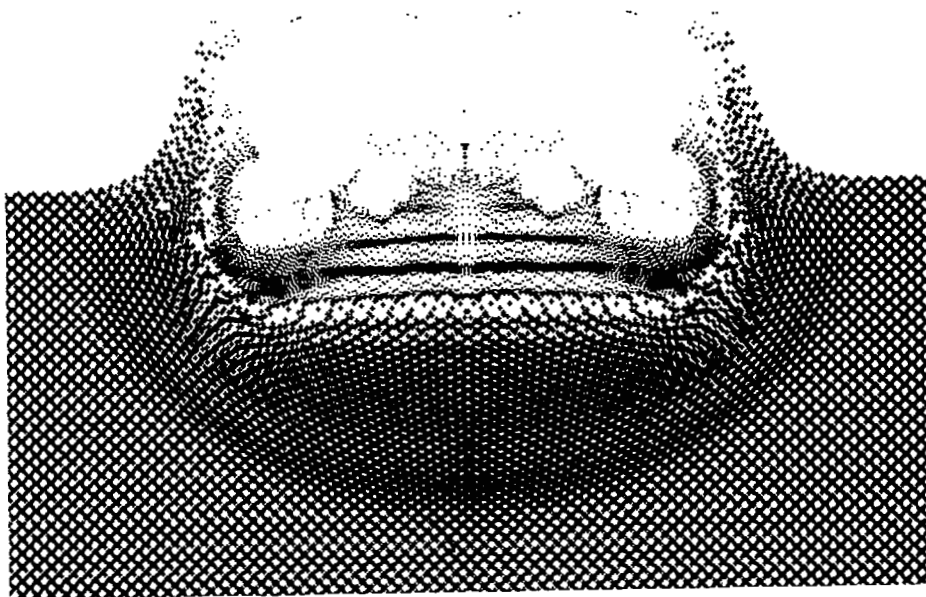
(e) Projectile-target configuration, t = 0.394 μsec (VISTA)

(f) Velocity field, t = 0.394 μsec (VISTA)

Figure 25 continued. Problem N4.

(g) Projectile-target configuration, t = 0.707 μsec (VISTA)
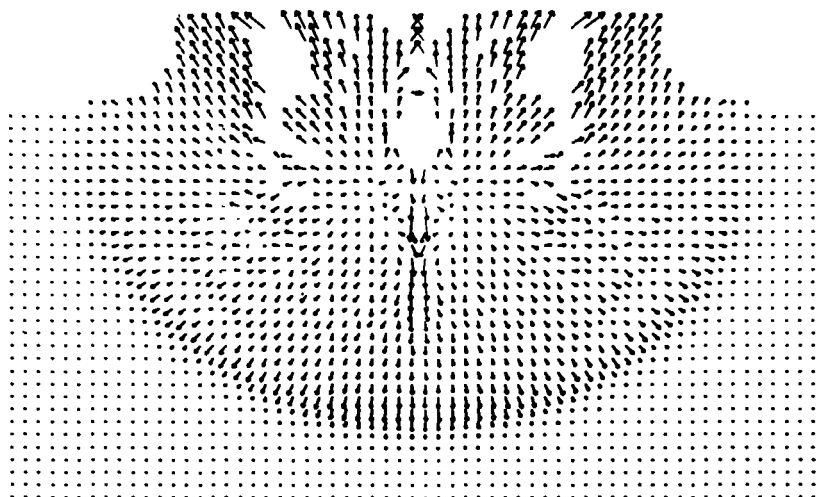
(h) Velocity field, t = 0.707 μsec (VISTA)

Figure 25 continued. Problem N4.
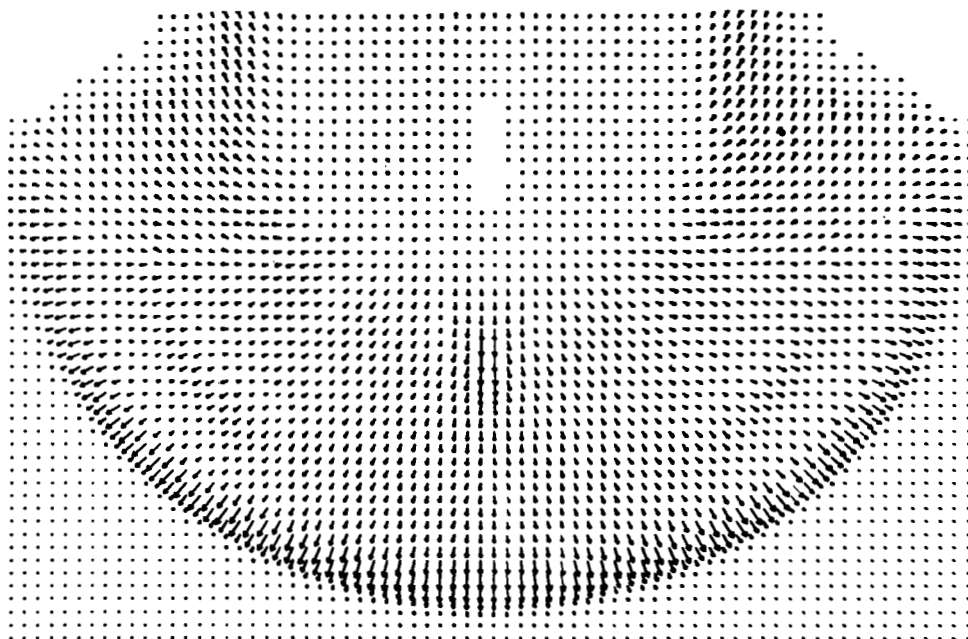
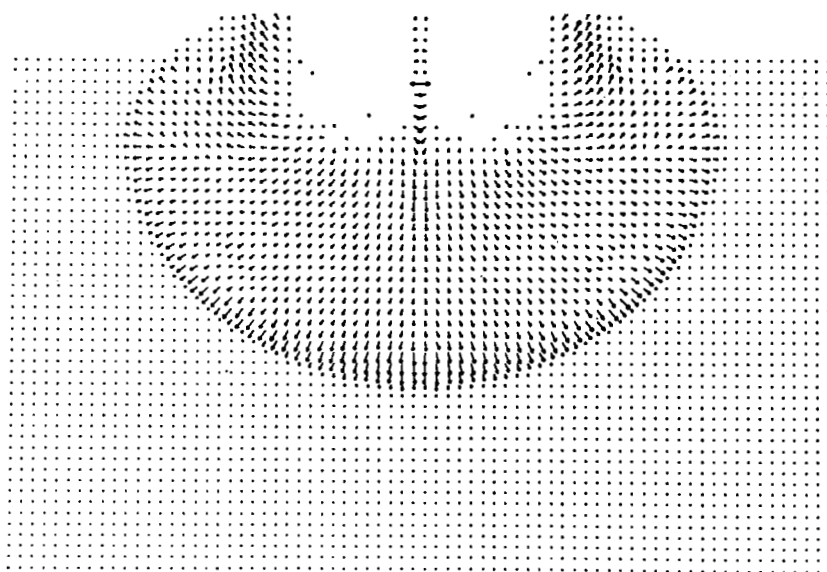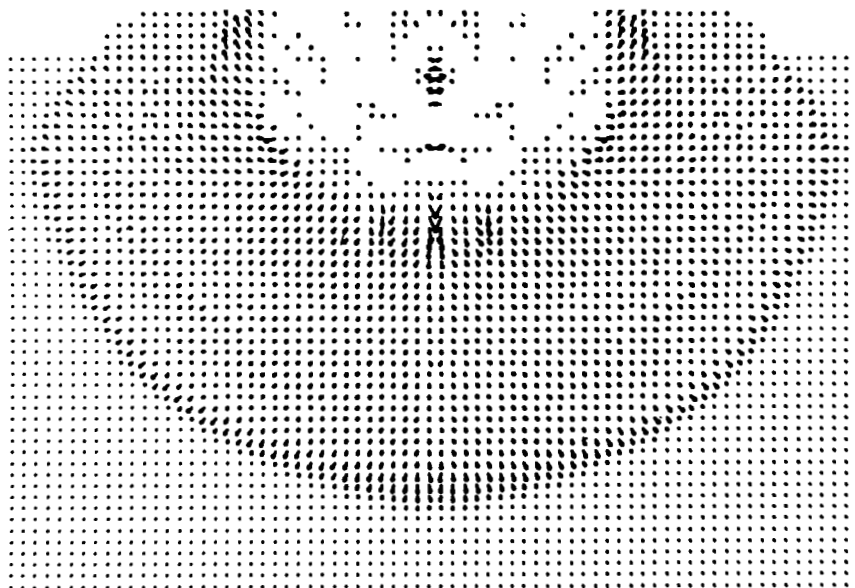(i) Mass flux, t = 1.191 μsec (PICWICK III)
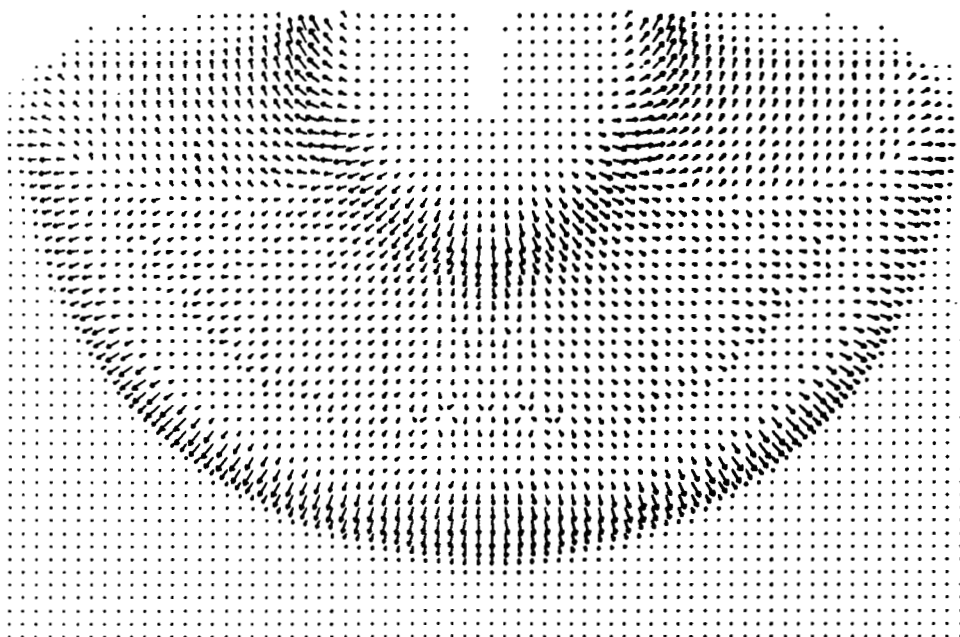
(j) Mass flux, t = 3.020 μsec PICWICK III)

Figure 25 concluded.   Problem N4.

90
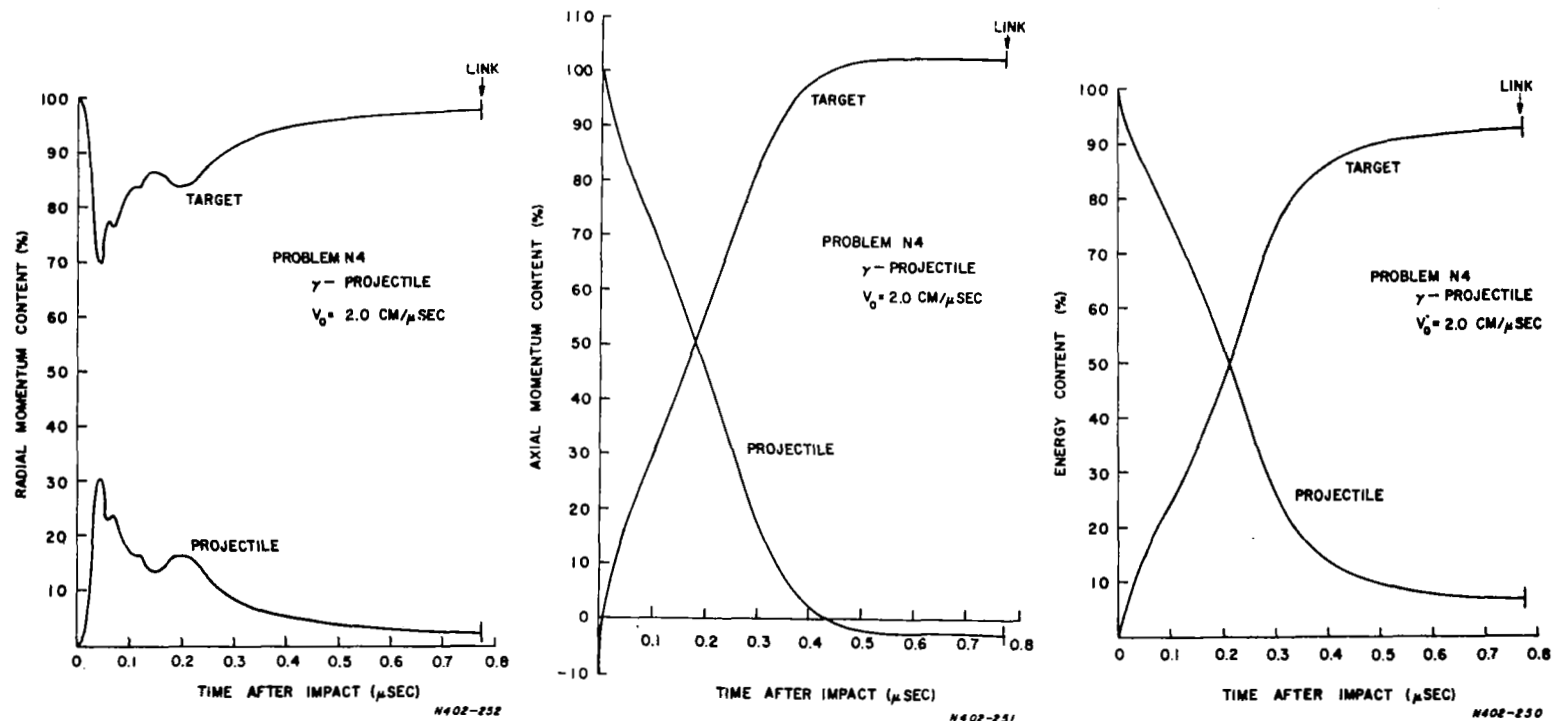
(a) Scalar radial momentum   (b) Axial momentum   (c) Total energy

Figure 26. Heterogeneous reduced-density projectile, problem N4: γ-projectile impacting target at $v_o = 2.0$ cm/μsec. Time variation of partition of momentum and energy content between projectile and target material.
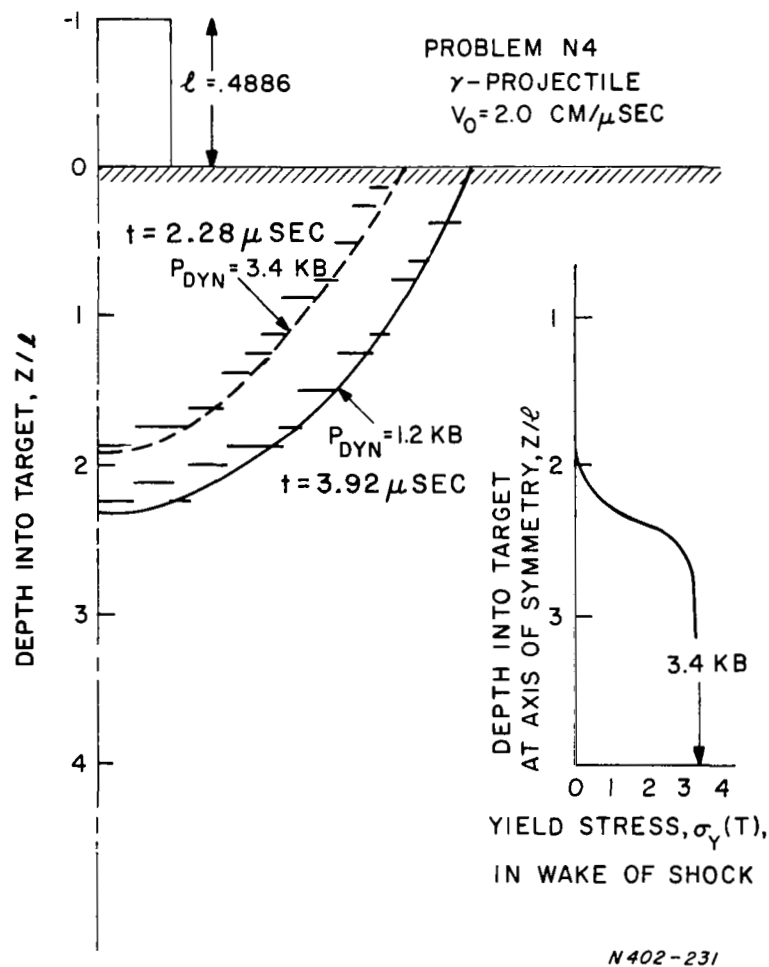
(a) Predicted crater
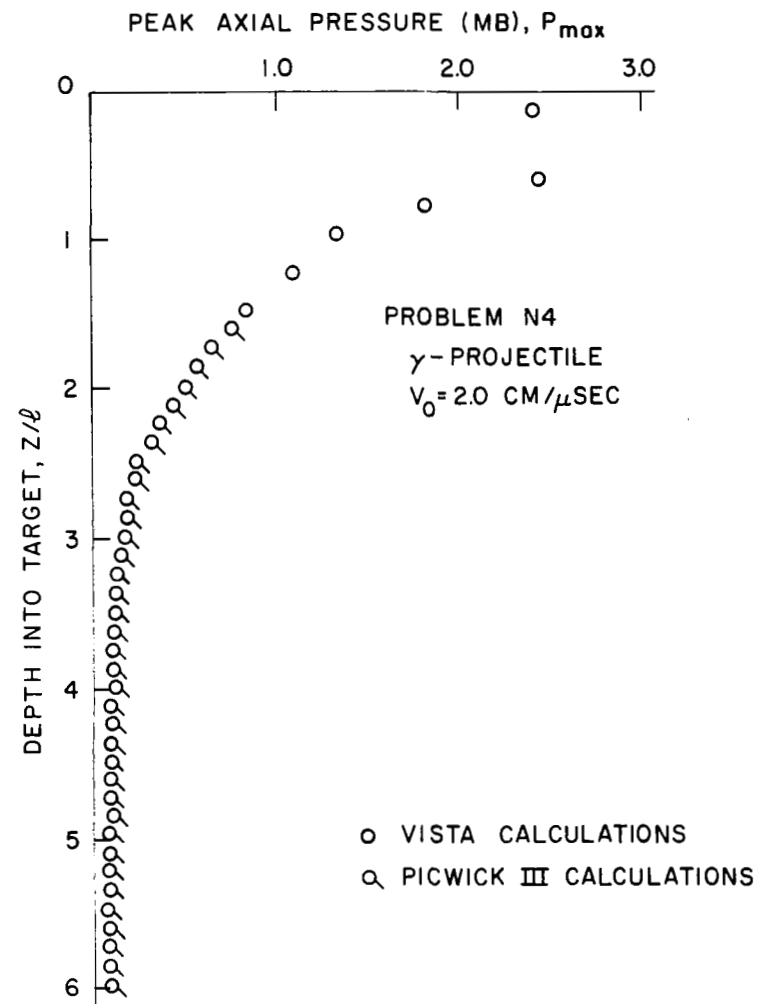
(b) Peak axial pressure along axis

Figure 27. Heterogeneous reduced-density projectile, problem N4: γ-projectile impacting target at $v_o = 2.0$ cm/μsec. Crater prediction based on dynamic pressure criterion.
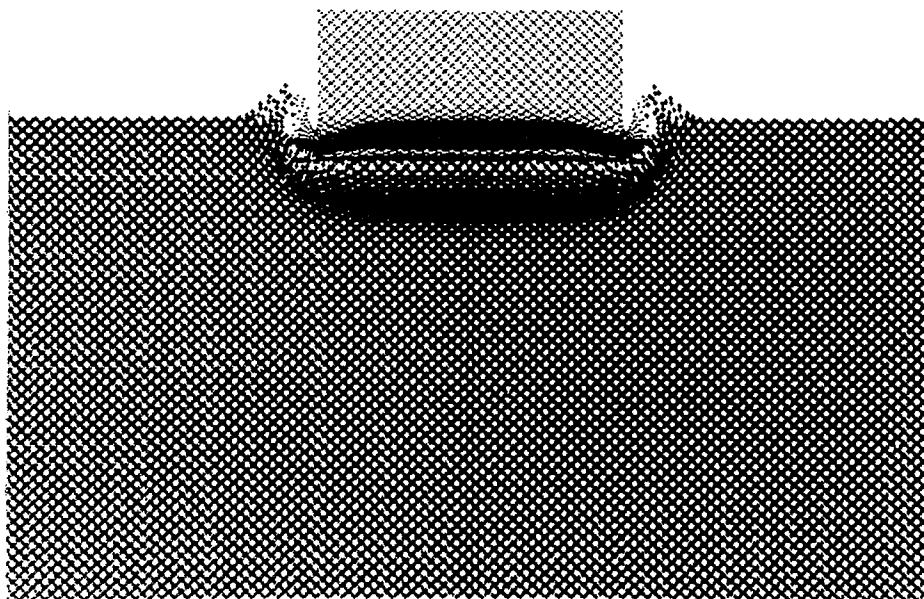
(a) Projectile-target configuration, t = 0.152 μ sec (VISTA)
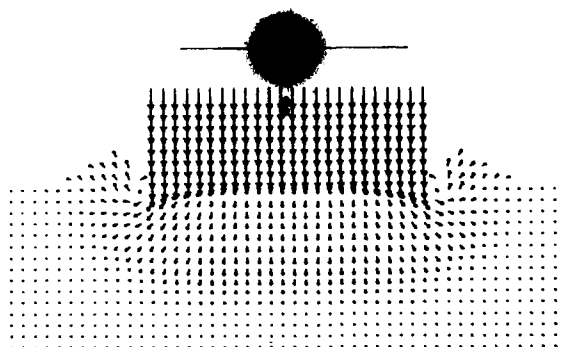
(b) Velocity field, t = 0.152 μ sec (VISTA)

Figure 28. Homogeneous reduced-density projectile, problem N5: δ-projectile impacting target at v_o = 2.0 cm/μsec. Graphical displays of projectile-target configuration, velocity field, and mass flux at indicated times.
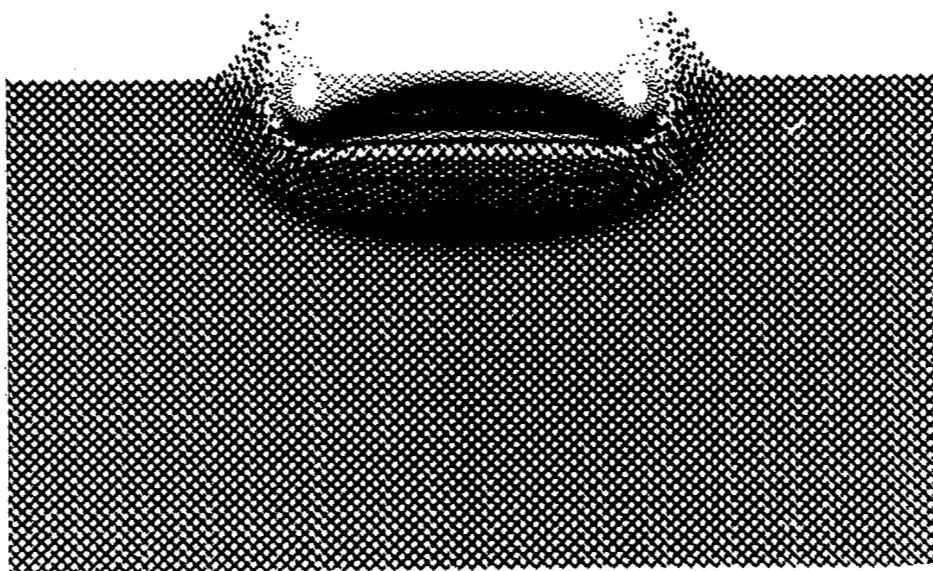
(c) Projectile-target configuration, t = 0.238 μ sec (VISTA)

(d) Velocity field, t = 0.238 μ sec (VISTA)

Figure 28 continued. Problem N5.

94

(e) Projectile-target configuration, $t = 0.290\ \mu$ sec (VISTA)

(f) Velocity field, $t = 0.290\ \mu$ sec (VISTA)

Figure 28 continued. Problem N5.

(g) Projectile-target configuration, t = 0.418 μsec (VISTA)
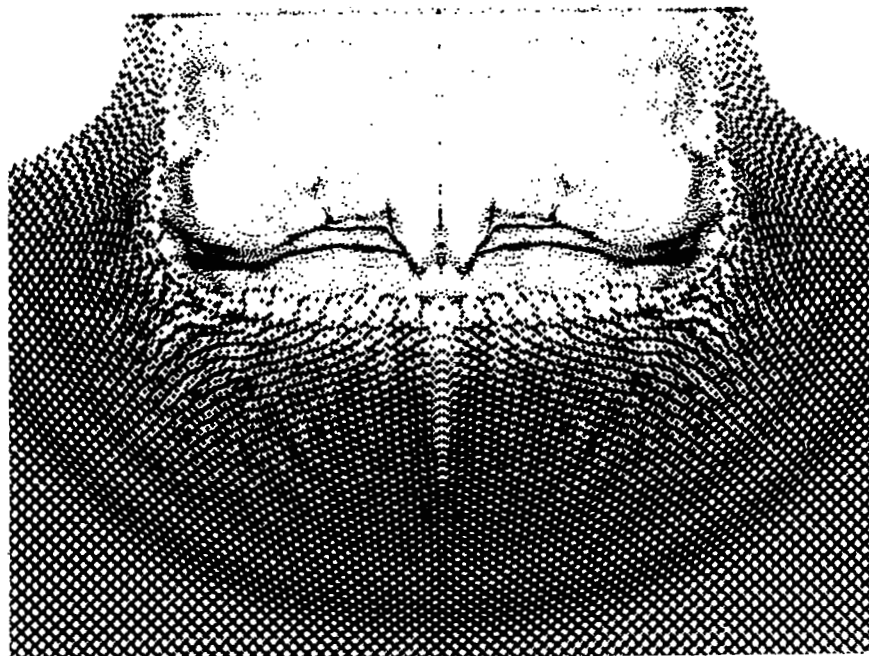
(h) Projectile-target configuration, t = 0.689 μsec (VISTA)

Figure 28 continued. Problem N5.

(i) Mass flux field, t = 1.246 μ sec (PICWICK III)

(j) Mass flux field, t = 1.836 μ sec (PICWICK III)

Figure 28 concluded. Problem N5.
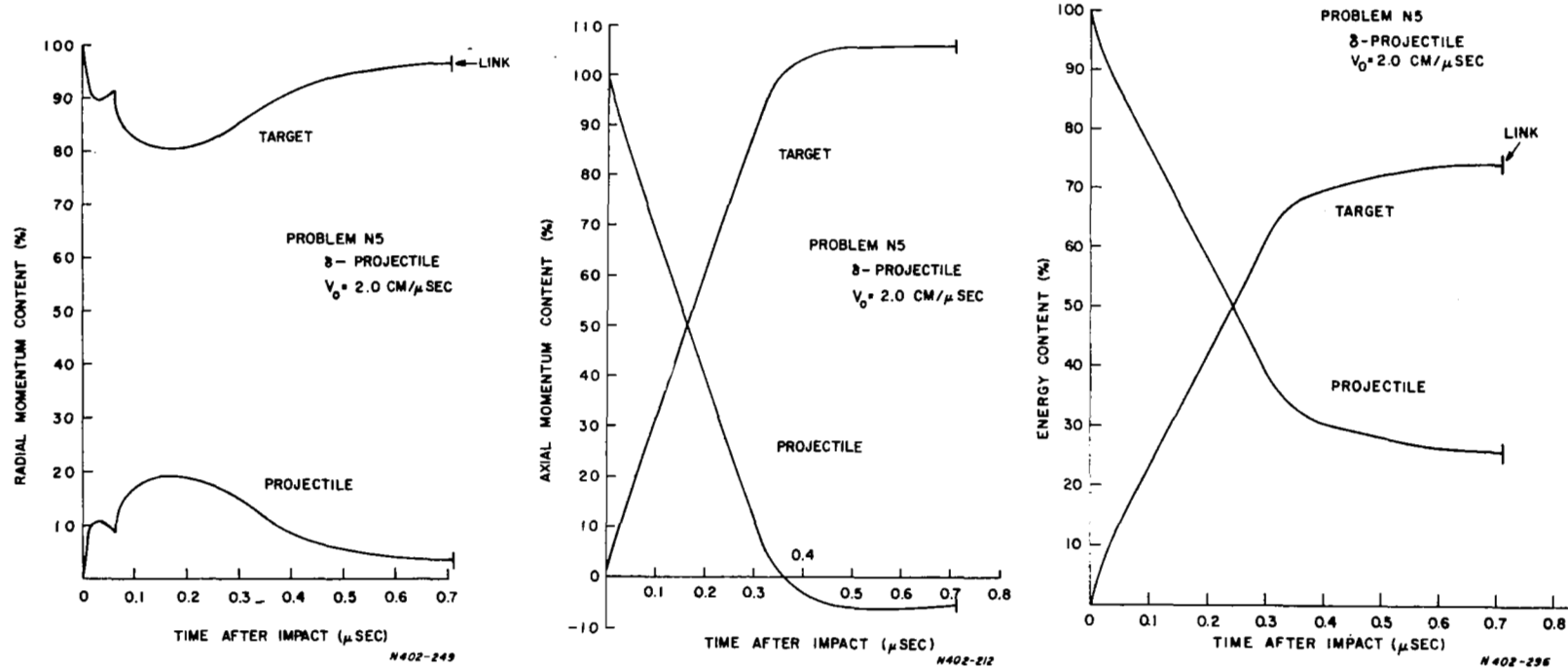
(a) Scale radical momentum   (b) Axial momentum   (c) Total energy

Figure 29. Homogeneous reduced-density particle, problem N5: δ-projectile impacting target at v_o = 2.0 cm/μsec. Time variation of partition of momentum and energy content between projectile and target materials.
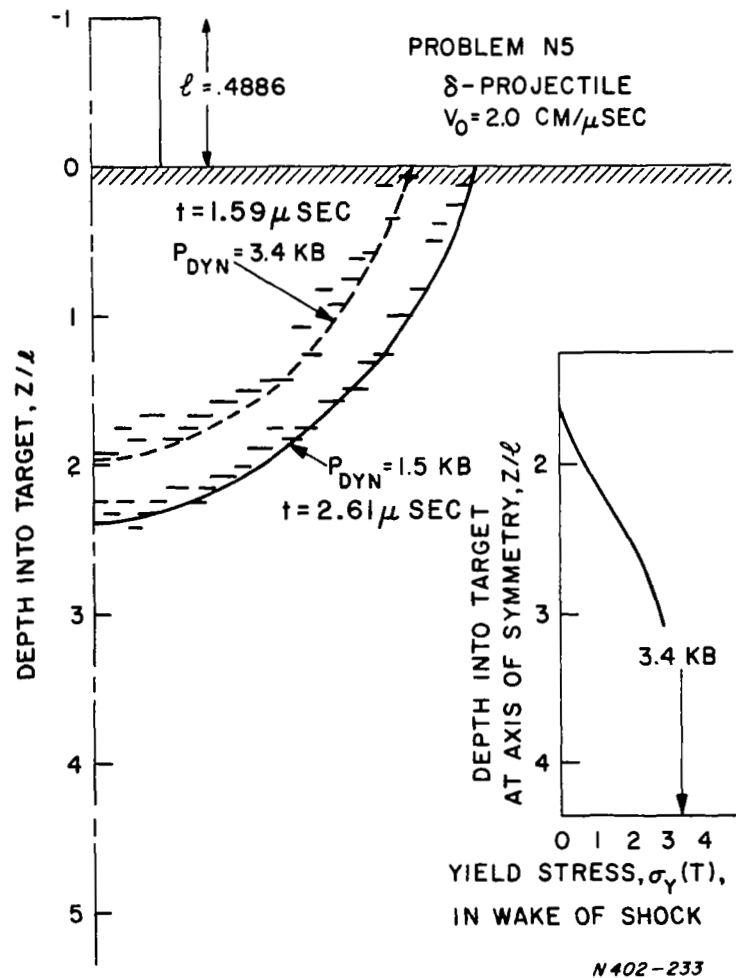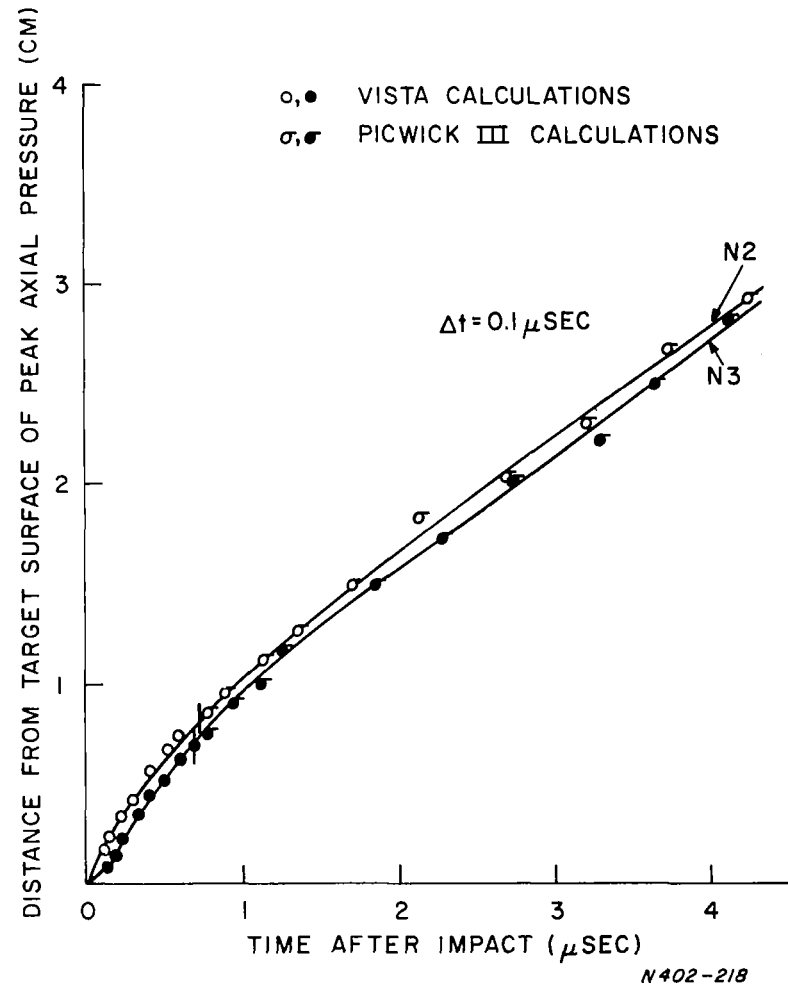
(a) Predicted crater
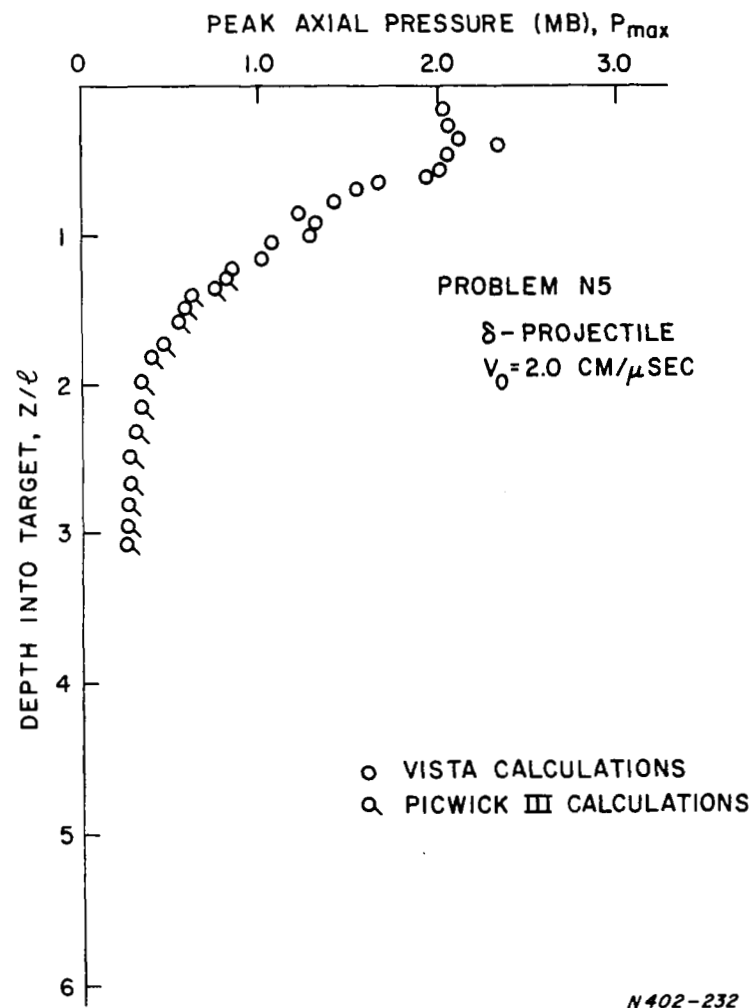
(b) Peak axial pressure along axis

Figure 30. Homogeneous reduced-density projectile, problem N5: δ - projectile impacting target at v_o = 2.0 cm/μ sec. Crater prediction based on dynamic pressure criterion.
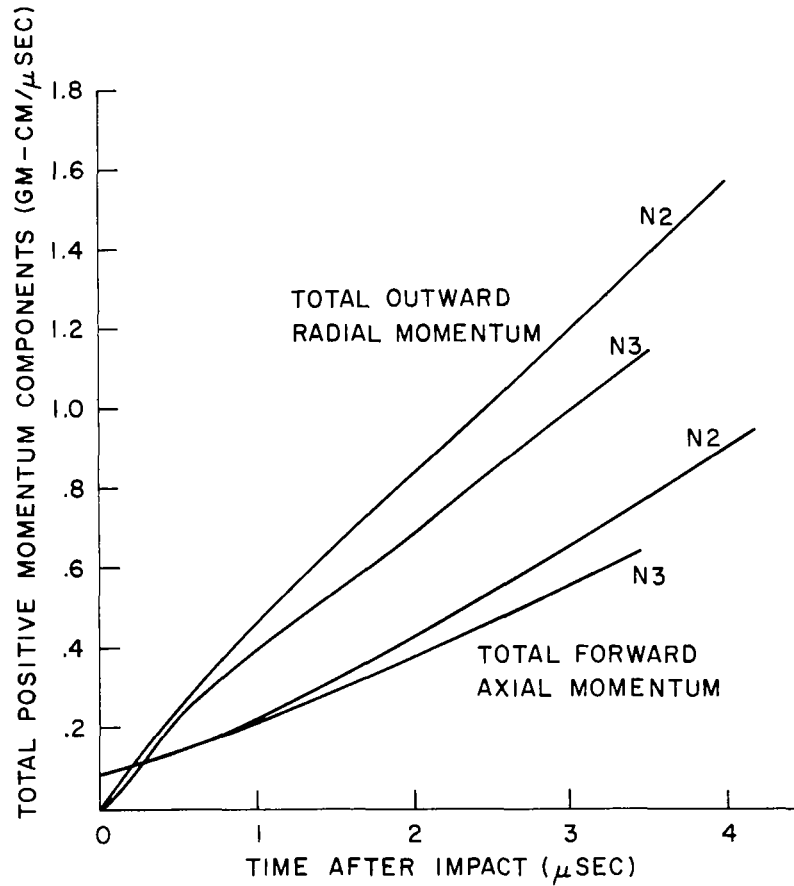
(a) Total positive momentum

(b) Time correction

Figure 31. Test of late-stage equivalence of problems N2 (normal-density projectile) and N3 (hetero-geneous reduced-density projectile).
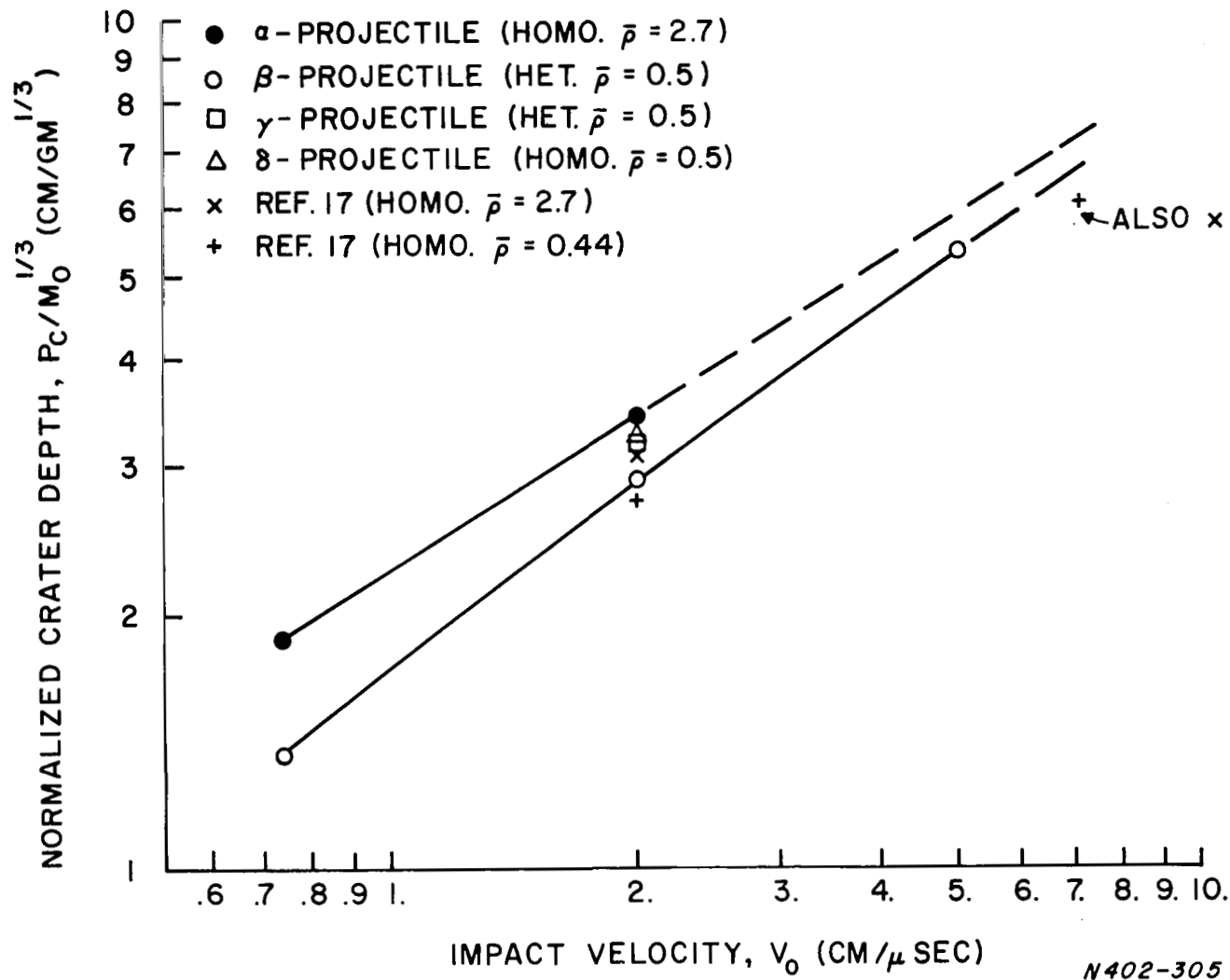
Figure 32. Predicted crater depth divided by cube root of projectile mass depicted as a function of impact velocity.
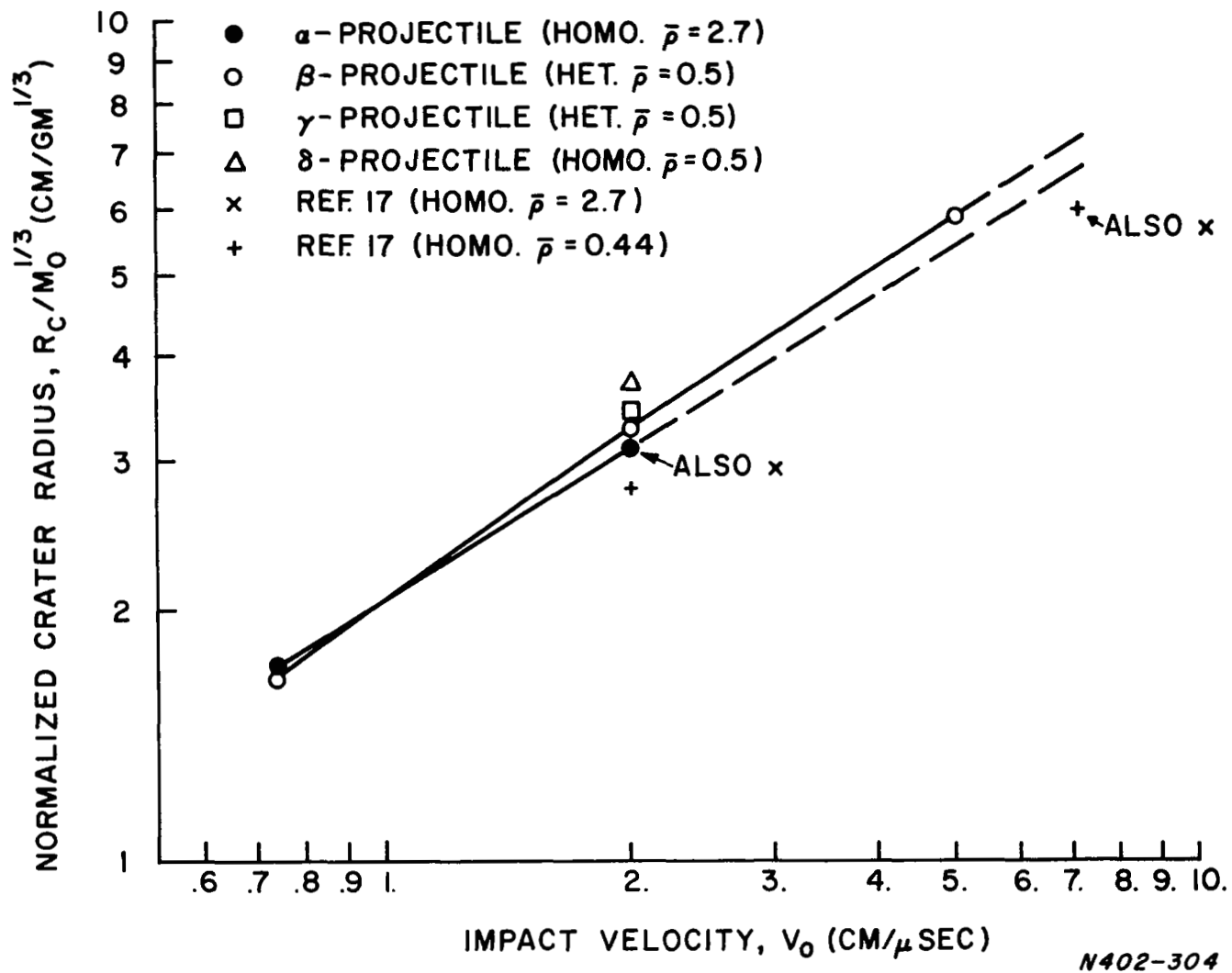
N402-305

Figure 33. Predicted crater radius divided by cube root of projectile mass depicted as a function of impact velocity.
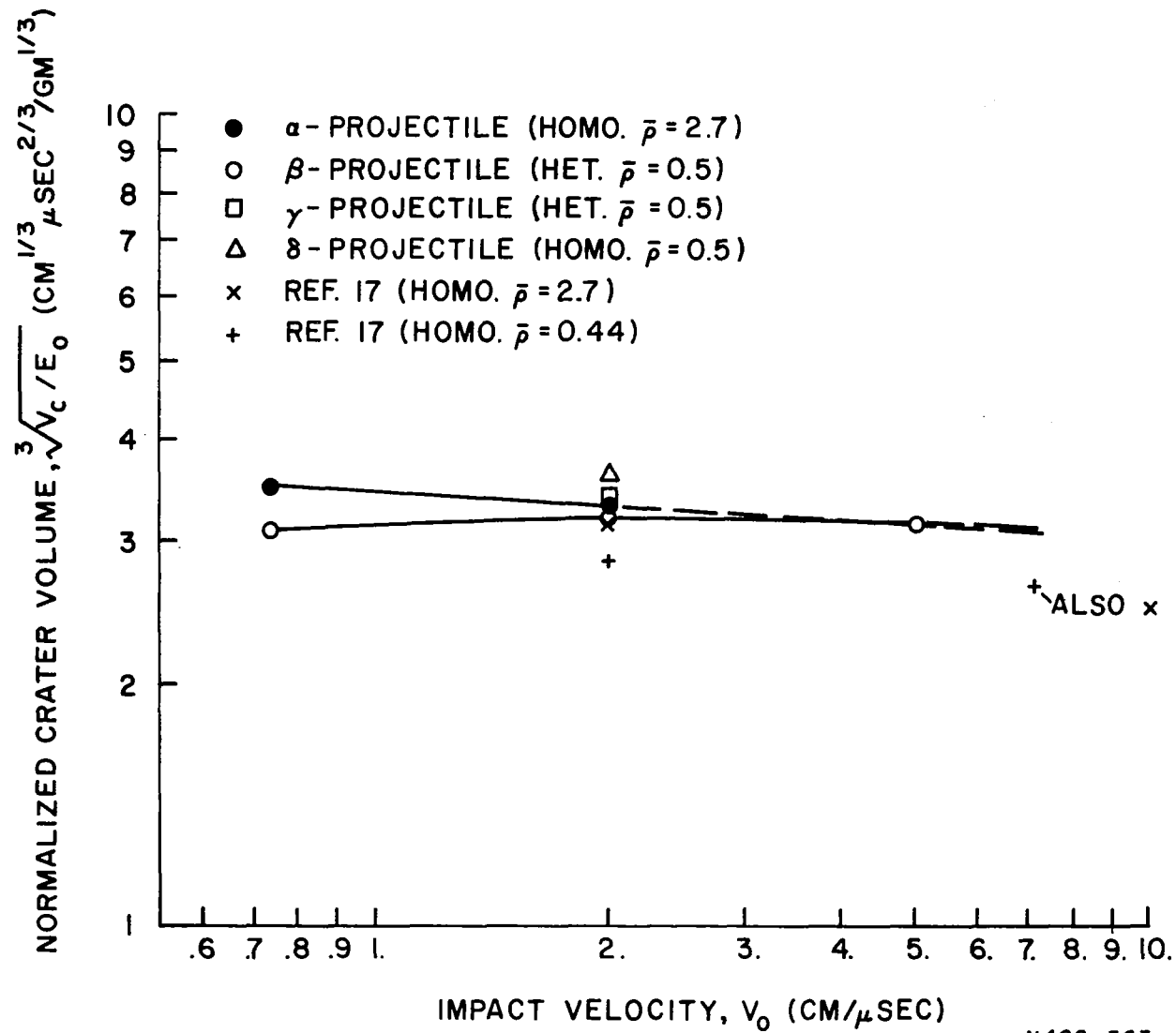
Figure 34. Cube root of the ratio of predicted crater volume divided by projectile kinetic energy depicted as a function of impact velocity.
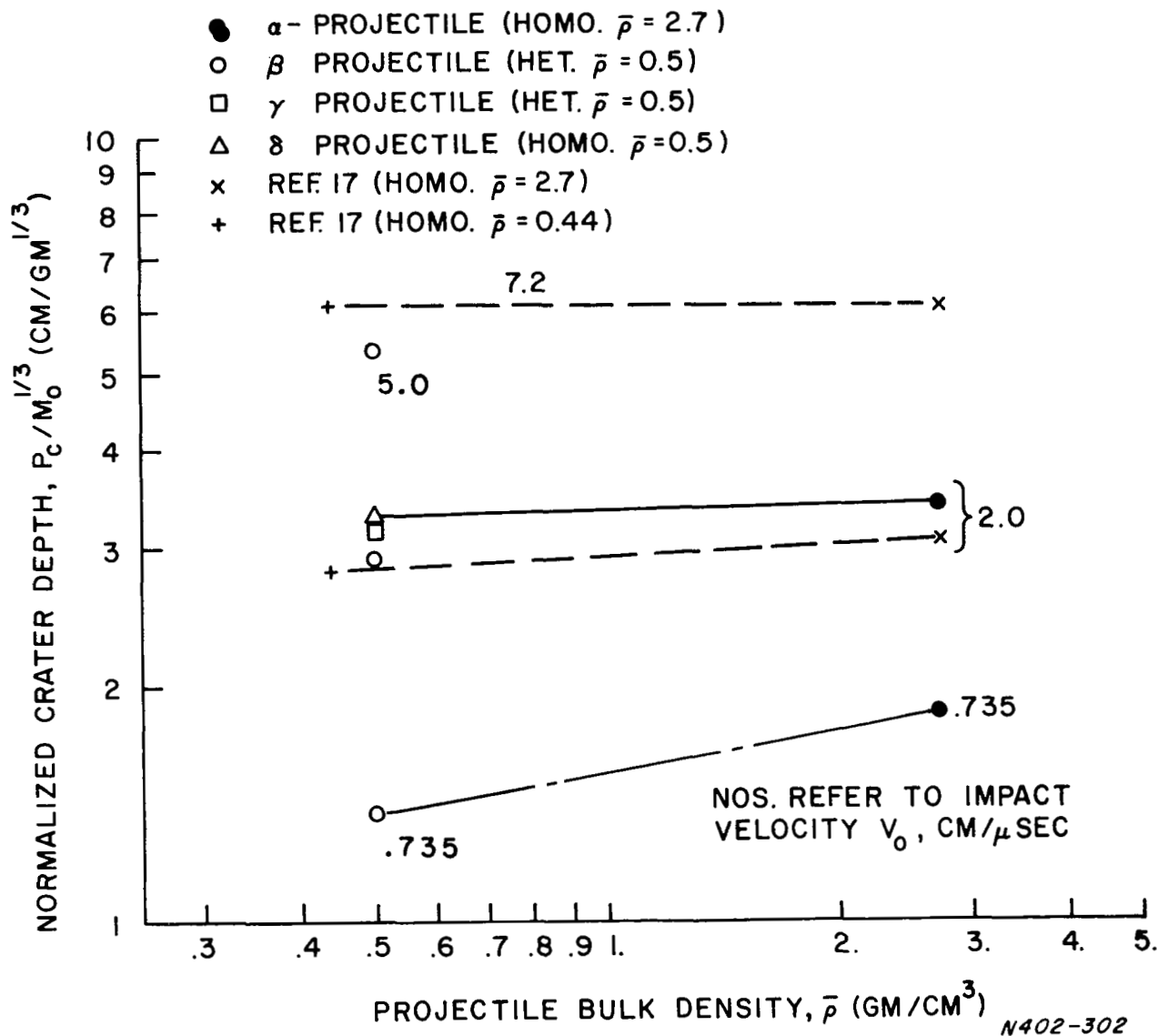
Figure 35. Predicted crater depth divided by cube root of projectile mass depicted as a function of the projectile bulk density.